Determination of Physical Parameters of LPV Stars and a Star Forming Region based on Annual Parallax Measurements

Tatsuya Kamezaki

Department of Physics & Astronomy,
Graduate School of Science & Engineering,
Kagoshima University

A Dissertation submitted to the
Graduate School of Science and Engineering,
Kagoshima University
for the degree of
Doctor of Philosophy (PhD),
March, 2015

Abstract

This thesis mainly focuses on obtaining accurate distances, and discussing the stellar properties of Long Period Variable (LPV) stars and star forming status based on the annual parallax measurements with Very Long Baseline Interferometry (VLBI). The celestial source's distance is the most fundamental and important parameter in astronomy. We cannot determine luminosities (or absolute magnitudes), masses, sizes and others of all celestial objects without knowledge of the distances to them. Therefore, we need to determine the distances precisely based on the most reliable method. I used the annual parallax to determine the distance because this is based on the most direct method and is reliable.

Chapter 1 gives the five distance measurements based on the different principles and why I used the annual parallax to determine the distance with VLBI compared with other three famous distance determination methods toward galactic sources, which are the kinetic distance, photometric distance and the distance based on the PL relations. The kinetic distance is estimated from radial velocity with the assumption of a galactic rotation model and it requires a precise galactic model. The photometric distance is estimated from the photometric observations with the assumptions of a model of the spectral type and the absolute magnitude, and it requires the precise extinction correction based on the reddening. The annual parallax is estimated from the annual motion of target (e.g. masers and stars) and it requires only the precise orbit of Earth around the Sun. It gives the precise target position in 3D space.

Chapter 2 gives the data reduction process of VLBI and the parameters to be corrected and the tasks of the standard data reduction software, Astronomical Image Processing System (AIPS). In following sections, I described what the data obtained with VLBI is, which is called as visibility. Then I explained the four fundamental parameters; the phase, group delay, delay change rate and intensity, which are obtained with VLBI and should be corrected. In addition, I described the procedure to obtain the phase-referenced images. In the last section, I noted the attentions and the special procedures in VERA data reduction.

We summarized all the observations in the Chapter 3. The VLBI observations were conducted with the VLBI Exploration of Radio Astrometry (VERA) to obtain the position of the water masers and to measure their parallaxes. The single-dish observations were conducted with VERA Iriki telescope and Kashima 34 m telescope. During VLBI observations, we monitored the target source with VERA Iriki telescope to know the intensity and to chase the variation. The observations with Kashima 34 m have the purpose to obtain the map of NH_3 emission and to understand the temperature distribution of the region.

From Chapter 4 to Chapter 6, I described the actual observational results and discussions of the three targets; LPV stars, RX Bootis and RW Leporis and a star forming region, NGC2264. We determined the distances toward these sources based on our annual parallax measurements with water masers. Therefore, the distance is more reliable than any previous estimation. The measured distances are consistent with the previous results and the accuracies of the distances were improved. Based on our derived distances, we determined the some physical parameters of

the targets; the luminosity, radius and mass. Moreover, we discussed the positions on the Period-Luminosity (PL) diagram and the stellar evolutionary stage for the observed LPV stars. For the star forming region, we discussed the driving source of the maser, and its evolutionary stage.

These studies mentioned above are summarized and the expected works from my studies are described in Chapter 7.

Contents

List of Figures

List of Tables

1 Introduction

The distance of a celestial object is a very important parameter in astronomy and it requires the discretion in estimating the distance. Then, we must understand the assumptions and the principle to estimate the distance and its uncertainty. In the former half of this chapter, we introduced the importance of the distance in astronomy and the various methods to measure the distance. We showed the influence of the determination of a source's distance to physical parameters, using three examples (luminosity, virial mass and LTE mass) in section 1.1, and we introduced the various methods to measure the distance in section 1.2. In the latter half of this chapter, we introduced observational methods to measure the distance. We introduce some methods to estimate the distance until section 1.2 and we chose the annual parallactic distance. To measure the annual parallactic distance, we chose to use masers and Very Long Baseline Interferometry (VLBI). Sections 1.3 to 1.5 give the explanation of the maser and VLBI.

1.1 Influence of the determination of a source's distance to its physical parameters

Although a distance is very important for astronomy, it is very difficult to measure distances toward many kinds of astronomical objects even in the Milky Way Galaxy (MWG). To indicate the importance, we exemplify some parameters: luminosity, viral mass, and local thermodynamic equilibrium (LTE) mass. When we consider a spherical star which has a radius R and a luminosity L_0, and is located at a distance D from the star, we can make the equation below since the energy is preserved at any distance in the case of no additional radiations and absorptions,

$$4\pi D^2 L = 4\pi R^2 L_0 \tag{1.1}$$

From the equation, luminosity can be estimated as follows;

$$L_0 = L(\frac{D}{R})^2. \tag{1.2}$$

Therefore, luminosity is proportional to the square of the distance D^2. When the D becomes twice, L_0 becomes four times.

The virial mass is the mass under the virial equilibrium, which is the equilibrium between twice kinetic energy and gravitational force for a spherical symmetric source (cloud). Assuming that the kinetic energy is indicated in the linewidth of the spectrum and that the line is not broadened, the virial mass, M_{vir} is

$$M_{\rm vir} = 250 \frac{R}{[\rm pc]} \frac{\Delta v_{1/2}}{[\rm kms^{-1}]}, \tag{1.3}$$

where R is the radius of the cloud and $v_{1/2}$ is the Full Width Half Maximum (FWHM) velocity of the line. Since R is estimated from the apparent radius

$R_{\rm app}$ of the source, which is measured as an angle, through $R = R_{\rm app}D$, where D is the distance to the source. Therefore, $M_{\rm vir} \propto D$ and $M_{\rm vir}$ becomes twice when the distance becomes twice.

LTE mass is estimated from the column density, which is obtained with the assumption of the local thermodynamic equilibrium (LTE). The LTE mass, $M_{\rm LTE}$, is given as an integration of the column density, N over the source extinction on the sky. Therefore, $M_{\rm LTE} \propto D^2 N$. It means that $M_{\rm LTE}$ becomes four times when the distance becomes twice.

Like these examples, some parameters are sensitive to the distance and these luminosity or masses vary with the fourth or second power of the distance. This indicates the importance of the distance. From the next section, we show the methods to measure the distance.

1.2 How to measure the Distance

In this section, we introduce five methods according to the different principles to measure the distance to the celestial objects. Each schematic image is shown in Figure 1.1.

1) *The method to measure the time of signal arrival*

When we know the velocity of the signal and we can measure the time lag between sending and receiving, we can measure the distance. For example, we send the signal to the target and we receive the signal reflected by the target. If we measure the time between sending and receiving, we can know the distance by multiplying the velocity of the signal by the time lag.

2) *The method estimated from the apparent motion of the target position*

We know that there are the difference in vision when we see it from the different direction. For example, our views are a little different when we see only with the right eye and when we see only with the left eye. This effect is called as parallax. In the case of the source outside of the solar system, the distance does not vary in the scale of a year. The positions of these sources vary with the observed days because of the Earth's revolution. This is called as annual parallax since it varies with the period of a year.

3) *The method estimated from the comparison of apparent and intrinsic intensities in visible light and near infrared*

It is the relation between the apparent and absolute magnitudes. A supernova in type Ia is one of the simplest example. Because of its constant absolute magnitude, we can estimate its distance only from its apparent magnitude. We can estimate the distance when we expect the absolute magnitude and measure the apparent magnitude.

4) *The method estimated from the comparison of apparent and true sizes*

The modified version of this is often used in astronomy. For a expanding shell, we can measure the proper motion and the radial velocity. The proper motion is an apparent motion on the celestial plane and it is in the unit of angle per time. The radial velocity is measured in the unit of length per time using the Doppler effect. If we assume that the shell is spherically expanding with constant velocity, the proper motion and the radial velocity should be same. Therefore, we

can know the distance from the comparison of the proper motion and the radial velocity.
5) *The method estimated from the systematic motion*
When the target is a part of a large scale system, we sometimes find a relation between radial velocity and the distance. Using this relation, we can measure the distance from the velocity measured using the Doppler effect. One of examples of this method is Hubble's law, which is relation between a radial velocity and the distance of a distant galaxy based on the assumption of the cosmic expansion.

From next subsection, we introduce the famous four methods to measure the distance toward sources in the MWG.

1.2.1 Kinetic Distance

This method is an the example of type 5) shown above. This method is most often used to estimate the distances of many sources and/or to know the galaxy-sized motion because it is very easy to estimate a distance. This kinetic distance can be estimated from the radial velocity of the source V_r, the position (galactic longitude) of the source l, galactic rotation velocity Θ, galactic constant R_0 and Θ_0 via the following equation;

$$V_r = \Big(\frac{\Theta}{R} - \frac{\Theta_0}{R_0}\Big) R_0 \sin l \tag{1.4}$$

From, this equation, the iso-velocity contours of V_r on the galactic plane are is shown in Figure 1.2, The value of Θ of the target can be obtained from the galactic rotation curve. If we know the galactic constant, we should measure only the radial velocity V_r. When we obtained V_r, we can easily estimate the distance R from the galactic center through equation 1.4. We can estimate the distance from the Sun, r, using the distance from the galactic center R. After combination of these procedures, we can get the equation,

$$r = R_0 \cos l \pm \sqrt{R^2 - R_0^2 \sin^2 l}. \tag{1.5}$$

Although this is simple process, it is based on many assumptions and its precision is low. First, it is powerless for a target located on some positions. We cannot estimate the distance of the sources in the direction of $l = 0^\circ$ and $l = 180^\circ$, because the radial velocity is always zero, as you can see the equation 1.4. Second, it is dependent on the model of the galactic rotation. Although the kinetic distance depends on the values of the galactic constants, they have not been fixed with enough accuracy. The peculiar motion of the target also gives the systematic error. Third, we obtain two solutions for r when the target is inside of the solar circle as you see the 1.5. Often, we assume the flat rotation model based on the observed results of the extra-galaxies, although it may not be true.

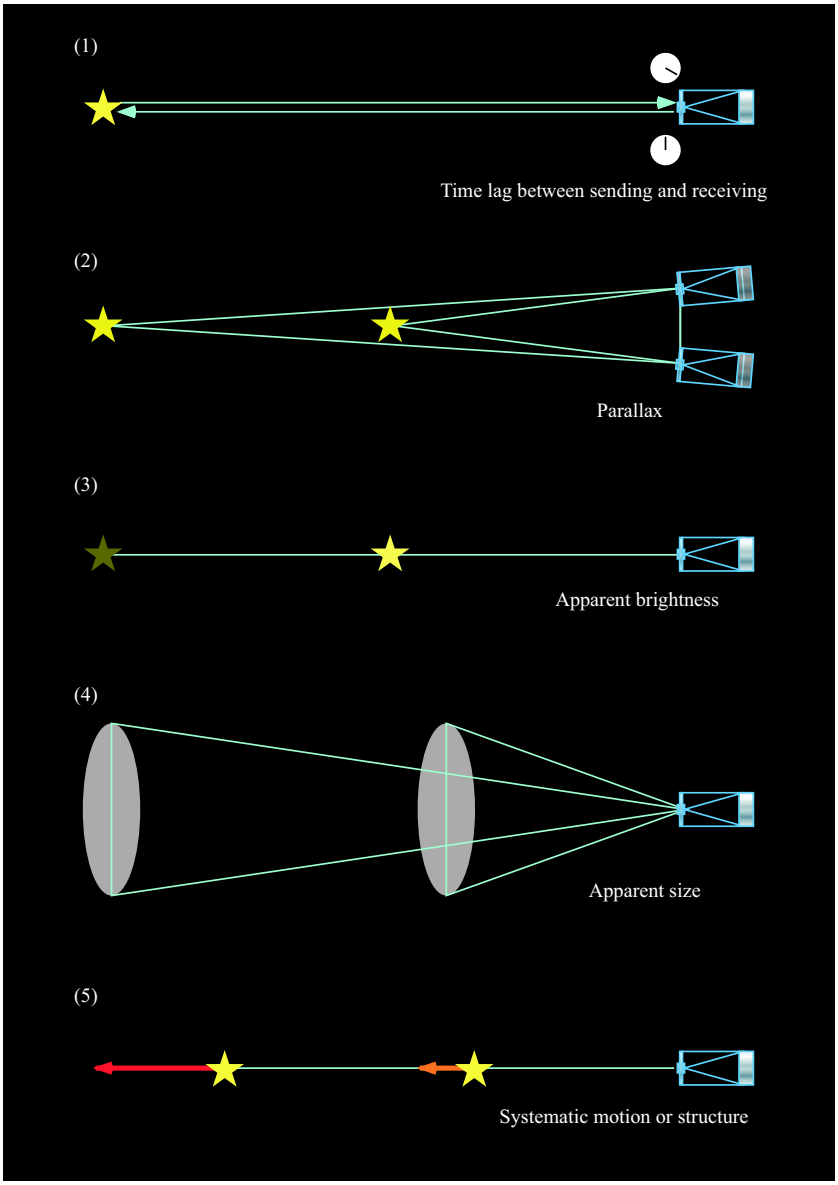

Figure 1.1: The schematic images of general methods to measure distances to celestial objects

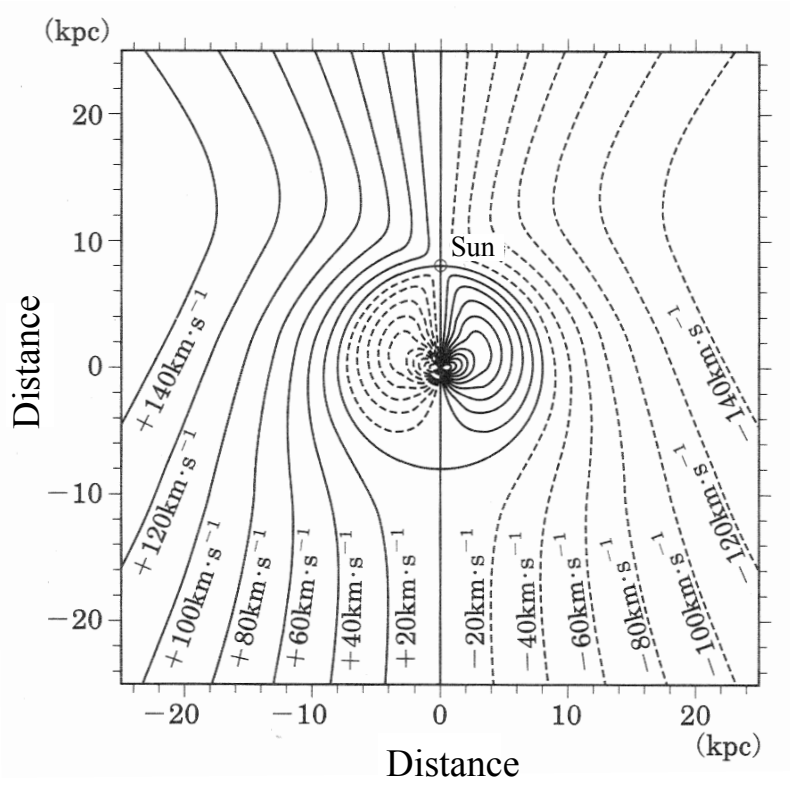

Figure 1.2: The iso-velocity contours of $V_r$on the face-on view of the galactic plane

1.2.2 Photometric Distance

This method is an the example of type 3) shown above. Photometric distance is determined with the optical photometry, which gives the colors and apparent magnitudes of a star. For a main sequence star we can easily expect the absolute magnitude, if it is extinction free. However, there is interstellar and circus setllar extinction actually. If we can estimate the extinction free color of the star from its spectral type, we can estimate the reddening. With the reddening, the extinction correction is performed and it gives the extinction free apparent magnitude. For an early-type star, we can obtain the distance by comparing the absolute magnitude expected using the template with the extinction corrected apparent magnitude. In this method, the potential systematic errors are reliability of the template of absolute magnitude, the corrections of reddening and the spectral type of the target.

1.2.3 Period – Luminosity (PL) relation

This method is an the example of type 3) shown above. Variable stars have the relations between their periods and luminosities, as called PL relation. The Cepheid variable stars have PL relation, which was found by Leavitt (1908). After the finding of Cepheid's PL relation, Glass & Evans (1981) found that Mira variable stars also have PL relation based on the observations of Large Magellanic Cloud (LMC). There are many observations to determine the PL relation for reliable stars not only in extra galaxies but also in MWG (Feast et al., 1989; Wood & Sebo, 1996; Wood, 2000; Whitelock & Feast, 2000; Ita et al., 2004; Yeşilyaprak & Aslan, 2004; Glass & van Leeuwen, 2007; Whitelock et al., 2008). Although the PL relations were previously studied in optical bands, it is often observed in infrared bands in these days since infrared band is not affected by interstellar or circum-stellar extinction so much compared to optical band. In many infrared bands, K-band is often used.

PL relations are described as

$$M = \rho \log P + \delta, \tag{1.6}$$

where M is the absolute magnitude. P is the period, and both ρ and δ are constants, depending on the type of the variable star. If you measure period of a star and assign the type of the variable star, you can obtain the absolute magnitude (M) using PL relation. When you measure the apparent magnitude, m, you can obtain the distance, D, through the equation;

$$m - M = 5(\log D - 1), \tag{1.7}$$

where m is the apparent magnitude. However, unfortunately, this procedure has some uncertainties, because PL relations for the MWG variable stars has not yet established until now. To establish the relation we need independent estimations of distances for many variable stars in MWG.

1.2.4 Annual Parallactic Distance

This method is an the example of type 2) shown above. This is the classical method, because it does not use any astrophysical characteristic of the target. Historically, Bessel (1838) became succeeded to measure the parallax toward 61 Cygni. It uses the Earth's revolution around the Sun and the schematic image is shown in Figure 1.3. The ϖ is the annual parallax and is the apparent radius of the annual motion of the target source if the source moves with the same velocity in space as the Sun. From the geometry, the object with the distance D [pc] from Earth shows the annual parallax, ϖ [rad], with

$$\sin \varpi = \frac{1}{D}. \tag{1.8}$$

The target out of the solar system is far enough, $\sin \varpi \sim \varpi$. Therefore, using the definition of pc, distance D in the unit of oc can be estimated from $D = 1/\varpi$, when the unit of ϖ is arcsec.

In the method, we have some problems. We must determine the positions of the target in many time (at least three or four times) in a year with the accurate positions. To measure the accurate positions, the reference source must be used and is considered to be fixed on the sky. In the optical wavelength, we can use stars themselves as the reference sources. When we take an image (or a photographic picture) of the target star, there are many stars in the same image. Using images covering the whole sky at many epochs, we can estimate the rest frame and obtain the many relative positions of the target star using simultaneous multi parameter fitting. From the variation of relative positions, we can estimate the parallax. HIgh Precision PARallax COllecting Satellite (Hipparcos) measured many (more than one hundred thousands of) parallaxes of stars using this method. However, it is limited to the point-like and bright source which is brighter than 9 mag in B band. For example, there are much interstellar dust and strong extinction although there are many sources near galactic center. It is difficult to measure the parallaxes of the star draping circumstellar dust like evolved star or young star since their lights are affected from their envelopes. And certainly, the dark star located far cannot be observed. In the case of radio astrometry, the continuum sources, which are limited to the source located far away and fixed on the sky such as quasars, are often used as the reference source since they are considered to be sufficiently distant and fixed on the sky. And as a target, we can use maser source or sometimes continuum source. Until now, the annual parallaxes of many sources are determined. Now, there are several instruments to be able to measure the annual parallax, such as Very Long Baseline Array (VLBA), VLBI Exploration of Radio Astrometry (VERA), European VLBI Network (EVN), Japanese VLBI Network (JVN) and GAIA satellite.

1.3 Astronomical Masers

Microwave Amplification Stimulated of Emission of Radiation, maser, is the strong radiation from the space. This is very strong emission and non-thermal

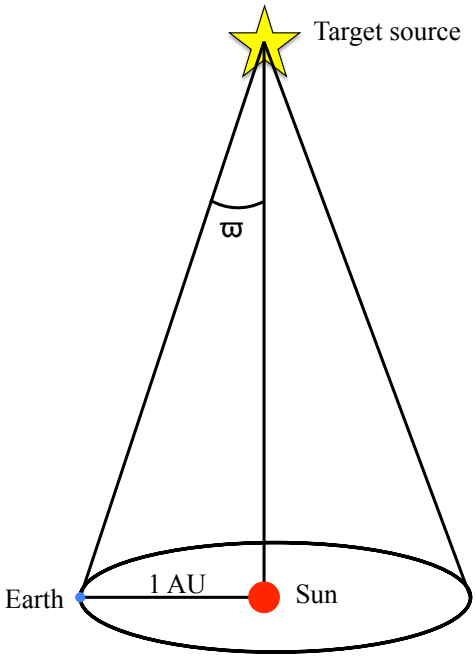

Figure 1.3: The schematic image of the parallax

emission. At the time of discovery, it is called as "mysterium" in 1960s because the emission mechanism is unclear. Afterwards, this is now very important for astronomy to know the physical properties of the sources.

1.3.1 Einstein Coefficient and inverse population

We use three energy levels to explain the maser emissions shown in Figure 1.4. The energy levels are E_3, E_2 and E_1 in descending order according to the energy and the instability. At first, we explain the made emission mechanism in the case of ground level, $E_1 = 0$, using lower level E_1 and E_2. Certainly, the particles prefer E_1 to E_2. The particles transit between E_1 and E_2 because of the following three reasons; 1) particles in E_2 naturally transit from E_2 to E_1, 2) particles in E_1 absorb the photon and they transit from E_1 to E_2, and particles in E_1 are induced by the photon and they transit from E_1 to E_2. The probability of these transitions 1) – 3), R_1 – R_3 are shown as the following;

$$R_1 = A_{21} n_2, \tag{1.9}$$

$$R_2 = B_{12} I_\nu n_1, \tag{1.10}$$

$$R_3 = B_{21} I_\nu n_2, \tag{1.11}$$

where I_ν is the intensity of the incident photon, n_1 and n_2 is the number density of the particles in E_1 and E_2, and A_{21}, B_{12} and B_{21} are called as "Einstein Coefficient" and indicate the probability of each transition for one particle.

Using these probabilities, the radiative transfer is shown as

$$\frac{dI_\nu}{ds} = \frac{h\nu}{4\pi}[R_1 + R_3 - R_2]\phi(\nu), \tag{1.12}$$

where the $\phi(\nu)$ is the profile function and it is normalized. The equation can be expressed using Einstein coefficient as

$$\frac{dI_\nu}{ds} = \frac{h\nu}{4\pi}[-(B_{12} n_1 - B_{21} n_2) I_\nu + A_{21} n_2]\phi(\nu) \tag{1.13}$$

On the other hand, the radiative transfer equation using radiative coefficient j_ν and absorption coefficient κ_ν is

$$\frac{dI_\nu}{ds} = -\kappa_\nu I_\nu + j_\nu \tag{1.14}$$

From the comparison equation 1.13 and 1.14, we can express the radiative coefficient and absorption coefficient as

$$j_\nu = \frac{h\nu}{4\pi} A_{21} n_2 \phi(\nu) \tag{1.15}$$

$$\kappa_\nu = \frac{h\nu}{4\pi}(B_{12} n_1 - B_{21} n_2)\phi(\nu) \tag{1.16}$$

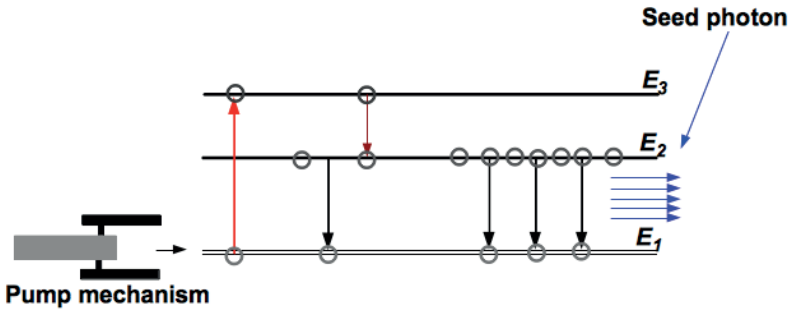

Figure 1.4: Maser emission excitation mechanism

In general, absorption coefficient is > 1 and electromagnetic wave is absorbed. However, electromagnetic wave is amplified when absorption coefficient is < 1 and the particles transiting from E_1 to E_2 is more than those ofE_2 to E_1. That is, particles in E_2 are more than those in E_1 and the population is inverse for general case. Therefore, the population is called as "inverse population". The microwave amplification based on the principle was suggested by Charles Townes in 1954 and his pupil, James P. Gordon published their successful experiment of maser oscillation (Gordon et al., 1955).

The particles in E_2 is dropped in E_1 and temporarily occupy E_1, but they pumped to E_3, release some energy and drop to E_2. Again, the particles in E_2 drop to E_1 with the stimulated emissions. These processes are iterated. The pumping from E_1 to E_3 is the natural process in inter stellar medium which can excite molecules in E_1, giving them enough excitation energy to move from E_1 to E_3. The strong maser emissions are observed in water, OH and SiO line around the star forming regions and the evolved stars.

1.3.2 History of Maser Discoveries in astronomy

The first maser emission with 18 cm radio radiation from ground state of hydroxyl radical OH was discovered in Weaver et al. (1965). They observed OH absorption toward the Westerlund catalog, but they detected some strong emissions at the frequency near 1665 MHz, which is OH main line. These emissions cannot explained by thermal equilibrium and can explained by maser amplification invoked in Litvak et al. (1966) and Perkins et al. (1966). This was the entrance of the maser science. Cheung et al. (1969) found the water maser emissions from the star forming regions at 22 GHz line. Water masers were detected in the star forming regions, the evolved stars and the external galaxies.

After the discovery of the OH and water masers, some species of masers such as methanol, SiO, ammonia maser and so on (Barrett et al., 1971; Snyder & Buhl, 1974; Thaddeus et al., 1974; Wilson et al., 1982).

1.4 Applications of Masers

To emit masers, there are three conditions; (1) keeping up the inversion population, (2) that the cloud of the inversion population have enough long path length to amplify and (3) that masing directs for our line-of-sight. These masers are found around several kinds of astronomical objects such as star forming regions, evolved stars, the circum-stellar environments of planetary nebulae, halos of comets, extragalactic sources, and supernova remnants. Masers have the strong emissions (high brightness temperatures) and compact sizes. Masers are observed as a group of spots, and the size of a spot is constrained to be typically 1 AU (e.g. Reid & Moran 1981) in the case of water maser, because the scatter of radial velocity of the amplified spot is < 1 km s^{-1} and the range of the scatter becomes the spot size. This is very useful to measure the motion or the parallax of the masers. Masers indicate the motions around the sources from maser properties. For instance, we can know the outflows or the circum-stellar shells with high resolution VLBI (see section 1.5), which is possible thanks for masers to be compact and be strong. With VLBI, we can measure the accurate positions of the masers since masers are compact. The accurate positions give us the trajectory of masers around the sources and it includes the parallax, the proper motions and the internal motion. Hence, we can measure the distance to the source based on the compact nature of maser with VLBI. The Japanese VERA project is mainly aimed at observing masers source in MWG and measuring the annual parallaxes and their corresponding distances. Their final purpose is to make a 3-dimensional map of the distribution of evolved stars and star forming regions in the MWG.

1.5 Very Long Baseline Interferometry

Very Long Baseline Interferometry (VLBI) is a powerful tool to investigate the compact sources with maser emissions. It is utilizing long baseline to virtually synthesize large telescope which is impossible to technologically construct. VLBI is different from the combined interferometers (all of whose antennas are directly connected to the correlator) in some points because of the long baseline. Of course, all interferometers require us to correct the signal delay and to measure the accurate time although there are difference of the baseline length. To achieve requirements, we use the recorder and the frequency standard installed in each station in VLBI, and the recorded signals are delivered to the location of correlator and correlated. Thanks to the long baseline, we can get the high angular resolutions in the milli-arc seconds (mas) scale and know the physics of the sources in the scale. Although VLBI has high resolution, the sensitivity is low. Therefore, we can observed the non-thermal emissions from synchrotron radiation sources (Active Galactic Nuclei: AGN) or maser sources

(their brightness temperature is higher than 10^6 K). Due to the low sensitivity, VLBI cannot generally observed the thermal sources.

To study the radio astrometry, we meet the problem of the atmospheric fluctuations. Japanese VLBI array, VLBI Exploration of Radio Astrometry (VERA) has overcome it with the unique "dual-beam system" (Honma et al., 2008a). The system consists of two receivers and makes it possible to cancel out the effect of atmospheric fluctuations between two sources. With the dual-beam system of VERA, we can observe target and reference sources simultaneously, and measure annual parallaxes and proper motions of many astronomical objects at 6.7 GHz (C-band), 22 GHz (K-band) and 43 GHz (Q-band), whose configuration is shown in Figure 1.5. Other than VERA, many VLBI instruments to investigate the environments around astronomical sources. The famous astronomical VLBI instrument is Very Long Baseline Array (VLBA), which is composed of ten 25m-antennas establish in USA and is invested by National Radio Astronomy Observatory (NRAO). European VLBI Network (EVN) is an interferometric array of radio telescopes spread throughout Europe, Asia and South Africa that conducts unique, high resolution, radio astronomical observations of cosmic radio sources. Japanese VLBI Network (JVN) is Japanese VLBI array, which is consists of VERA, Tomakomai 10m, Usuda 64m, Hitachi 32m, Takahagi 32m, Tsukuba 32m, Kashima 34m, Gifu 10m, Yamaguchi 32m. JVN can observe 6.7 GHz (C-band), 8 GHz (X-band), 22 GHz (K-band), 43 GHz (Q-band).

1.6 In this thesis

We chose the parallactic distance method to measure the distance since the method is the smaller number of assumptions than the other methods. All our used data to measure the distances were obtained only with VERA. We introduced the data reductions with Astronomical Image Processing System (AIPS) and the explanation of phase referencing method in section 2. The three targets (RX Boo, RW Lep and NGC2264) were observed to measure the distances and these observations are summarized in section 3. We introduced the results of three parallax measurements were compared with the previous distances measured with the other methods, shown in each section (section 4 to 6). The parallaxes of RX Boo and RW Lep were obtained to be $\varpi = 7.31 \pm 0.50$ mas and $\varpi = 1.62 \pm 0.16$ mas, respectively. These corresponds to 136^{+10}_{-9} pc and 617^{+68}_{-55} pc, respectively. The distance of RX Boo was consistent with that obtained with *Hipparcos* and the distance of RW Lep was the first successful distance measurements. We discussed the physical parameters (luminosity, radius and mass) of these LPV stars in their section and these values were consistent with typical values of LPV stars. We observed star forming region NGC2264 to investigate the star formation with the accurate distance measurements based on annual parallax measurements. The obtained parallax was consistent with the previously obtained photometric distance. Since the NGC2264 star forming region is small interstellar extinction ($A_V \sim 1$ mag), the photometric distance is thought to be accurate. The X-ray-emitting driving source of the water maser

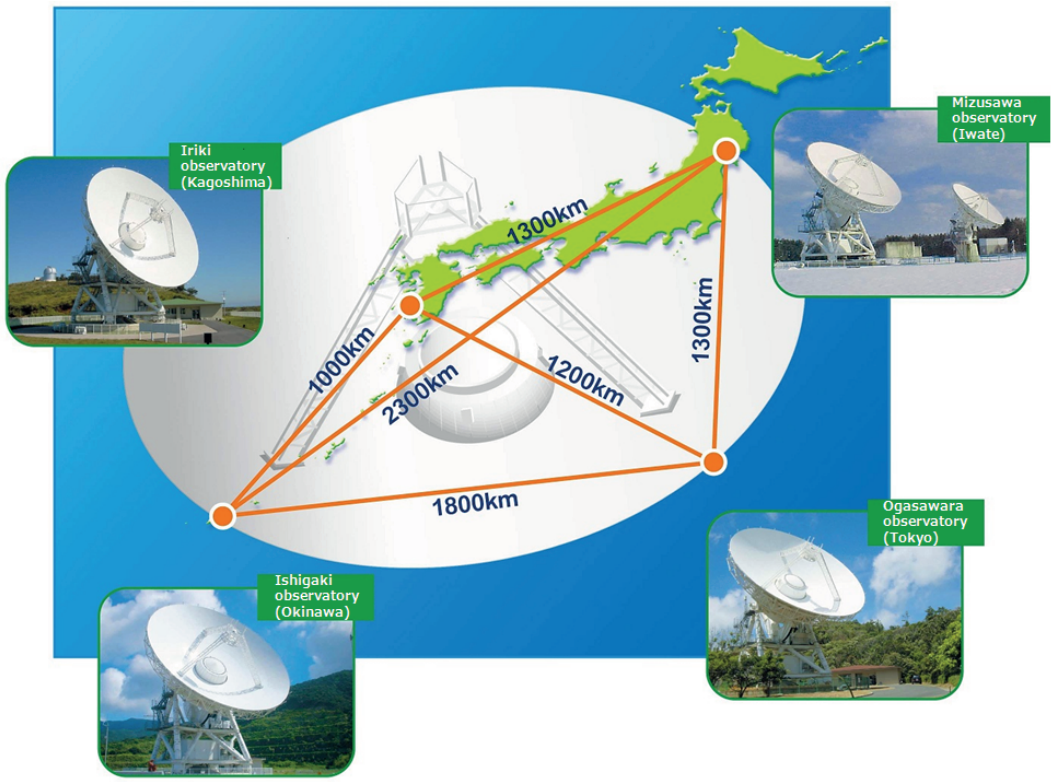

Figure 1.5: VERA four antennas and its positions

used to measure the parallax measurements was thought to be very young star, which is called as Class 0 source, based on some observational evidence (No sources in mid- and near infrared images, the higher density, the association of water maser and the higher column density than Class I source). And also the driving source may evolve to a low mass star, whose mass of ~ 1 $R_\odot$ from the $L_{\rm bol}$ – $M_{\rm env}$ diagram. Finally, we summarized these in section 7.

2 Data reductions with AIPS

The VLBI data is key to obtain the image and it is the base of valuable scientific discussion. Therefore, the VLBI data reduction is important and it must be done carefully. We must correct the fundamental observables (phase, group delay, delay change rate and amplitude) in the VLBI data, which is called as visibility. We adopted the phase-referencing method to correct these parameters which reflect the brightness distribution of the source. This chapter gives the procedures of the phase-referencing data reduction. The VLBI data reductions were held with Astronomical Image Processing System (AIPS) developed by National Radio Astronomical Observatory (NRAO). Since AIPS was made for the data taken with radio telescope and it also supports to reduce the interferometer's data, it has many tasks to be useful for VLBI. The fundamental observables (phase, group delay, delay change rate and amplitude) are mentioned in section 2.1 and we mentioned our data and phase-referencing in section 2.2. After these sections, we mentioned how to reduce the data with AIPS and we will note important parameters of tasks. Finally, we get the phase-referencing image.

2.1 Our Data and How to Reduce the Data

VERA has dual-beam system mounted to cancel out the atmospheric fluctuations. The dual-beam system is composed of A and B beam receiver. The A-beam is a receiver to observe a target source, mainly maser source, and the B beam is for the position reference source, such as the quasar. Since we can observe the two sources with the two beams, simultaneously, we can cancel out the atmospheric fluctuations and the phases are corrected. We used the phase-referencing method to cancel the atmospheric fluctuations (Kawaguchi et al., 2000). Since our data reductions include the method, it is called as phase-referencing data reductions.

2.2 Basic Observables

The observed signals are correlated with the correlator. The connected array, which is the interferometer in which all antennas are connected with cables, are correlated in real time. On the other hand, the VLBI data are cross-correlated with the correlator. The data obtained with interferometer including VLBI is called as visibility which is described as

$$V_\nu(u,v,w) = \int_l \int_m \frac{I_\nu(l,m)}{\sqrt{1-l^2-m^2}} \exp\{2\pi i(ul+vm+wn)\} dldm, \tag{2.1}$$

where (l, m, n) is the cartesian coordinate on the plane which the celestial plane and the vector toward the page tracking center ($\boldsymbol{s}_0$) are contacted, I_ν is the intensity of the observing source, and u and v is called as "spatial frequency" and u, v and w is described as

$$(u,v,w) = \Big(\frac{\boldsymbol{D}\cdot\boldsymbol{e_l}}{\lambda_0}, \frac{\boldsymbol{D}\cdot\boldsymbol{e_m}}{\lambda_0}, \frac{\boldsymbol{D}\cdot\boldsymbol{e_n}}{\lambda_0}\Big), \tag{2.2}$$

where $\boldsymbol{D}$ is the baseline vector, λ_0 is the wavelength and $(\boldsymbol{e_l}, \boldsymbol{e_m}, \boldsymbol{e_n})$ is the unit vector for (l, m, n). In the case of $l^2 + m^2 \ll$, the equation 2.1 becomes

$$V_\nu(u, v) = \int_l \int_m I_\nu(l, m) \exp\{2\pi i(ul + vm)\} dl dm, \tag{2.3}$$

This shows that the relation between visibility and the intensity of the source is fourier transformation.

The fringe phase is defined as

$$\phi = 2\pi\nu_0(\tau - \tau_i) = 2\pi \frac{\boldsymbol{D} \cdot (\boldsymbol{s} - \boldsymbol{s}_0)}{\lambda_0} = 2\pi(ul + vm + w(n-1)), \tag{2.4}$$

where $\tau_i = \boldsymbol{D} \cdot \boldsymbol{s}_0/c$ is the delay expected for the radio wave from the source at the phase tracking center, $\boldsymbol{s}$ is the vector for the source and τ is geometrical time delay. As you see the equation 2.4, phase include the informations of positions described as l and m.

The VLBI data are cross-correlated after observations. Then, we need to correct delays accurately to make them cross-correlated. We obtain the different delay for each antennas although the antennas receive the electromagnetic wave at the same time. The difference of the delays between antennas is due to the different antenna locations. Therefore, we need to the accurate time. Group delay, which is the phase gradient of the cross correlation spectrum with respect to the observing frequency band, can be expressed as

$$\tau_g = \frac{1}{2\pi} \frac{d\phi}{d\nu} \tag{2.5}$$

It is also important to know the delay (i.e. phase) change rate to track the phase. It is described as

$$\dot{\phi} = \frac{2\pi\nu \boldsymbol{D} \cdot \dot{\boldsymbol{s}}}{c} \tag{2.6}$$

These three main parameters (phase, group delay and delay change rate) and the Intensity (amplitude) which is included in the visibility are very important observables in VLBI. From the next section, we explain how to reduce the data with AIPS, focusing these four parameters.

2.3 Loading and Editing Data

VLBI data observed with VERA have the format of flexible image transport system (FITS). At first, we start AIPS already installed (The installation procedure of AIPS is beyond the scope of this thesis). When starting AIPS, there are four windows; a black window named TV server, main terminal, message server and task server. Mainly, we type the following command into the main terminal which you started AIPS. We must load the data in AIPS. We use task FITLD, which is the task of loading fits data and can be flexibly used for a number of purposes. We must set the adverb, which is the command to adjust the parameter of AIPS task. Before we use FITLD or set the adverb of it, we

confirm the number of the data. If there are troubles in the correlation, the fits data are often divided into some files (8 files at maximum in the case of me) in the case of VERA. If you have only one file, the adverb DOCONCAT is 0, and in the other case (there are more than 2 files), we set it as 1. The adverb DOCONCAT is to combine the fits data, and 0 is NOT combining data and 1 is combining the data. The CAT in DOCONCAT indicates the catalog and AIPS calls the data loading in AIPS as catalog. The catalog certainly includes some information (e.g. source position, scans, observing time and so on) and these informations are included in tables. The tables are divided in detail and each of these is named. For example, the table of source information is SU table, the tsys is TY table, gain curves is GC table and etc. The setting of DOCONCAT is most important here, you can set the catalog name or loading disk which the data region called in AIPS, etc. If you finished the setting, you type "go". Then, task FITLD should be starting. If FITLD was finished without critical troubles, "Appears to have ended successfully" are displayed on the message server.

Usually, VERA data are split two or more catalogs in the case of DOCONCAT = 1 according to the number of files. Then, the first catalog has primary data and the other data have only GC table(s). Since the GC table include the same informations at all, you must move one GC table to the primary data. You use task TACOP, which is to copy table(s) to another catalog and you copy the GC table to the primary data.

After the data are packed to one catalog, you sort the data configuration. The VLBI data have the time, baselines, scans and etc and we sort these in the adequate order. The task to do it is MSORT and it is a little slow. Since we need to obtain the CL (calibration) table to calibrate the data, we make the CL table with task INDXR, which make NX table in addition to CL table.

2.4 Checking the Data

Now, we loaded data as catalog of .MSORT or .UVDATA. Then, we check the data with some tasks. The observing informations are included in the data and we output it as the text files. We use task LISTR to output the scan informations, task PRTAB to output the source coordinates written in SU table and task PRTAN to output the antenna positions. If these are OK, you can check the data itself to use task VPLOT. VPLOT is the visibility plot and we can check the phase and amplitude of the data. Now, you check the existence of the data during the whole observation time, usually 8 or 9 hours.

2.5 Amplitude Calibration

From this section, we start to reduce the data. First, you take it into account that "Data are very valuable". In AIPS, we never delete tables including the estimates or informations obtained from some tasks. However, we use the CL table to reflect the solutions obtained from some tasks, which are stored in SN

(solution) tables. Therefore, we calibrate the data by renewing CL table and the final CL table are applied to the original data.

At the first calibration, we correct the amplitude with task ACCOR and APCAL. ACCOR is the task to normalize the visibility. Correlation coefficients has been already normalized in the correlation output. However in the case of the Mitaka FX correlator, the correlation coefficient is 3 – 4 times larger than the normalized coefficient. Thus, the need to run ACCOR with solution integration time (SOLINT adverb) of 10 to 30 minutes.

APCAL is the task to calculate the System Equivalent Flux Density(SEFD). The SEFD is to covert system noise temperature in kelvin (K) to jansky (Jy) and described as

$$SEFD = \frac{2k_{\mathrm{B}}T_{\mathrm{sys}}}{A_{\mathrm{e}}}, \tag{2.7}$$

where k_B is boltzmann coefficient, T_{sys} is system noise temperature and A_{e} is effective aperture of the antenna. When we calculate SEFD, we can compare the flux density of the source and we can estimate the signal-to-noise ratio (SNR).

After finishing these task, you must check the resultant SN tables with task SNPLT. If it has bad data, you can flag the data with task SNEDT. When using SNEDT, you must be careful. When the data seems to be good, you can apply the SN table to CL table with task CLCAL. After them, we finished the amplitude calibrations.

2.6 Bandpass Calibration

The bandpass calibration can be held with task BPASS. Since bandpass include the terms of phase and the amplitude, we must calibrate the two values. In first step, we calculate the amplitude correction from autocorrelation data with the phase of zero because the autocorrelation data is not affected from the coherence loss and has high SNR. In last step, we calculate the phase correction from cross-power function by decomposing the cross-power functions of the baseline into antenna-based complex bandpass response. We usually use the calibrator, strong continuum source, for this calibration because it has flat spectrum and is strong. In task BPASS, we set the adverb CALSOUR to the calibrator and the solution integration time (SOLINT) to -1 to obtain one solution for the whole observation. After finishing this process, BP table is made in the catalog.

2.7 Doppler Velocity Calibration

Rotation and revolution of the Earth makes Doppler shifts for the desired velocity and we must correct it to obtain the accurate radial velocity. In VLBI, the real time velocity tracking is not available. Therefore, the individual stations move along the line of sight of the target source making the spectra to meander with time within the bandpass. In the case of VERA, there is also the contribution for the motion of the continental plate, sometimes cause by the effect of earthquakes. Thus the accurate positions of the antenna need to be calibrated first using a model created by the VERA group in NAOJ. We use task CVEL

to calibrate it and the some settings are performed with task SETJY before CVEL. In the case of VERA data, although we are required by CVEL to input the velocity for the calibration, we do not know the velocity. Therefore we do CVEL at least twice in VERA data. Since usually the estimated velocity is different only smeller than 1 ch from the velocity in the data, we check whether the channel shift is smaller than 1 ch, which is displayed in the message server.

2.8 Phase and Delay Calibration

The purposes of the phase calibration are to obtain the accurate phase which has the informations of the source positions and the source structure and to integrate the visibility without coherent loss. Phase are related to the delay as shown in equation 2.4 or 2.5. The delay and delay change rate are roughly corrected in the correlation process. However, there are residuals for the delay and the delay change rate after the process. We use task FRING to calibrate the residuals in AIPS. FRING searches the residuals of the delay and the delay change rate to make SNR maximum, which called as fringe search. And the range to search the maximum is called as bring search window. In FRING, we set the adverb to determine the window with APARM and often set the SNR cutoff for weak source. You do this process once in the case of the strong reference source. When the reference source is weak, you divide this process into twice; first for the calibrator to solve delay only and guess delay of the reference source, and second for reference source to solve the delay and the delay change rate. If you finish this process, you check and flag it and apply to CL table. It takes longest time in the data reduction of VERA data. If you cannot wait, you can use task AVSPC, which averages the spectra and decrease the data volume, therefore the process becomes fast.

2.9 Self Calibration

This process is conducted for the reference source to make phases accurate or for target maser to obtain the relative position map. In the case of the former one, we use task SPLIT to isolate the source from the data and to integrate the channels. After SPLIT we obtain the new catalog with .SPLIT. In the case of VERA, we integrated from 4 to 60 channel since the reference source observed with B beam has 64 channel and the edge of bandpass is not flat. After this, we use task IMAGR to draw the image of the source, which is called as dirty map and is not experienced the CLEAN. We want to know the real distribution of the intensity, but the obtained image is convolved the real distribution of intensity and beam. To guess the real distribution of the intensity, we need to deconvolve. Since the solution of the deconvolution is not only one, one of the method to guess the real distribution of the intensity is CLEAN. In the dirty map, we can see clearly side-lobes. We can subtract the intensity peak of the target, which is considered to be real, from side-lobes, with the scaling adequately. This is the basic thought of the CLEAN. In AIPS, we can do a part of this process with IMAGR. You select PSEUDO, TVFLAME or something else to be easy to see

and you select the TVBOX to select the real image. After you select it, please select the CONTINUE CLEAN, then the image must change. You continue CLEAN until the intensity of the range you selected is under the outside of the range. When you get the condition, you select the STOP CLEANING. After finishing this process, you got the new catalog .IBM and ICL. The catalog of .IBM is the image of the synthesized beam and the ICL is the image of the CLEAN convolved image. You make SN table from the CLEANed image with task CALIB. The process of IMAGR and CALIB is iterated until the dynamic range, which is the ratio of the peak intensity and the image rms noise, reaches its peak. Therefore, SN table is generated at the number of iterations. The SN tables are copied to the SPLIT data catalog and you applies the SN tables to CL table with CLCAL. Maybe, all calibration is finished at this and you just make the final image.

In the case of maser source, we select the peak of the spectrum of the maser in the process of SPLIT. So, we must choose one channel in SPLIT and do NOT choose multi-channels. The reason we choose the peak is to obtain the good SNR. Except the point, the processes are same as the case of the reference continuum.

You do NOT do self-calibration of the target maser if you want to do the phase-referencing imaging. The position of the source is fixed at the positions of phase tracking center in the process of self-calibration and phase calibration shown in previous sub-section, since we solved the phase or delay in the position of the phase tracking center. Therefore, we lose the coordinate of the source unless the coordinate of the phase tracking center is accurate. If we know the accurate coordinate of the source, we correct the coordinate of the phase tracking center to it, but it is meaningless to know the coordinate based on the reduction in the case of it. Especially, we cannot know the absolute proper motion toward the moving source when we go through the processes. It is useful to know the maser distribution relative to the reference maser spot and its variation, although we lose the absolute coordinate. In the case, we can know the maser motions relative to the reference maser spot, which is often called as internal motion, and the mean motion is regarded as the motion of the reference maser spot. In VERA, the process including self-calibration and phase calibration for only the target maser source is called as 1 beam imaging since we used A-beam data only in the case.

2.10 Imaging

As you can see the equation 2.3, we can get the intensity distribution with the fourier transformation of the visibility. As you know task to do it in the previous section, we use task IMAGR to make image. Although we find the reference source at only the center of the image in the case of reference source, we must search the masers at the other positions. We add the offset into the imaging region with the adverb RASHIFT and DECSHIFT in unit of arcsec, and we can image the other region. When you find the maser spots, please CLEAN the spots. Then we do not lose the coordinate since the reference spot has the

reference coordinate. After CLEAN, you display the CLEANed image .ICL with the adverb TVALL and you can see the image. Since we want to obtain the position of the spots relative to the reference spot, we use task IMSTAT. We can get the positions and intensity using task IMSTAT and you make the map (distribution) of the masers if you collect the all positions of the maser spots.

2.11 Phase-Referencing

The phase-referencing has two main advantage; one is obtaining the absolute positions of the target and the other is availing the long integration time of the weak target. As former one is explained in the sub-section 2.10, we can obtain the absolute position of the target relative to the reference continuum. For the latter one, we can detect the fringe and can integrate the target source in the shorter time than the coherence time which is longest time to obtain the data the phases are roughly arranged and which determined by the atmospheric fluctuations. In the case of VLBI for the wavelength of 1 cm, the coherence time is about several tens of seconds, which is very short. When we use the phase referencing, we can calibrate the phase and delay with strong source and can apply it to target source. Thus, we can integrate it in longer time than the coherent time. As the procedure in AIPS, we copy the solutions of phase calibration and self-calibration with the reference source to the target source, and apply it to the target data. And we just do imaging of the target source. At last, we show the flow chart of the typical data reduction procedure for VERA data in Figure 2.1 .

2.12 Special procedures in VERA

VERA has some special process which is caused by the speciality of the VERA. One is the correction due to having the dual-beam. Since the two receivers have the different lengths of the cable, the recorded phases are certainly different. Therefore, we calibrate it to loading text data with the TBIN. The other one is called as uvw re-calculation, which is caused by no good uvw calculation model. We read the text data which the deference between better uvw calculation model and no good uvw calculation model is written in. These two processes are required and you cannot obtain the images without these processes. These processes must be applied before the imaging.

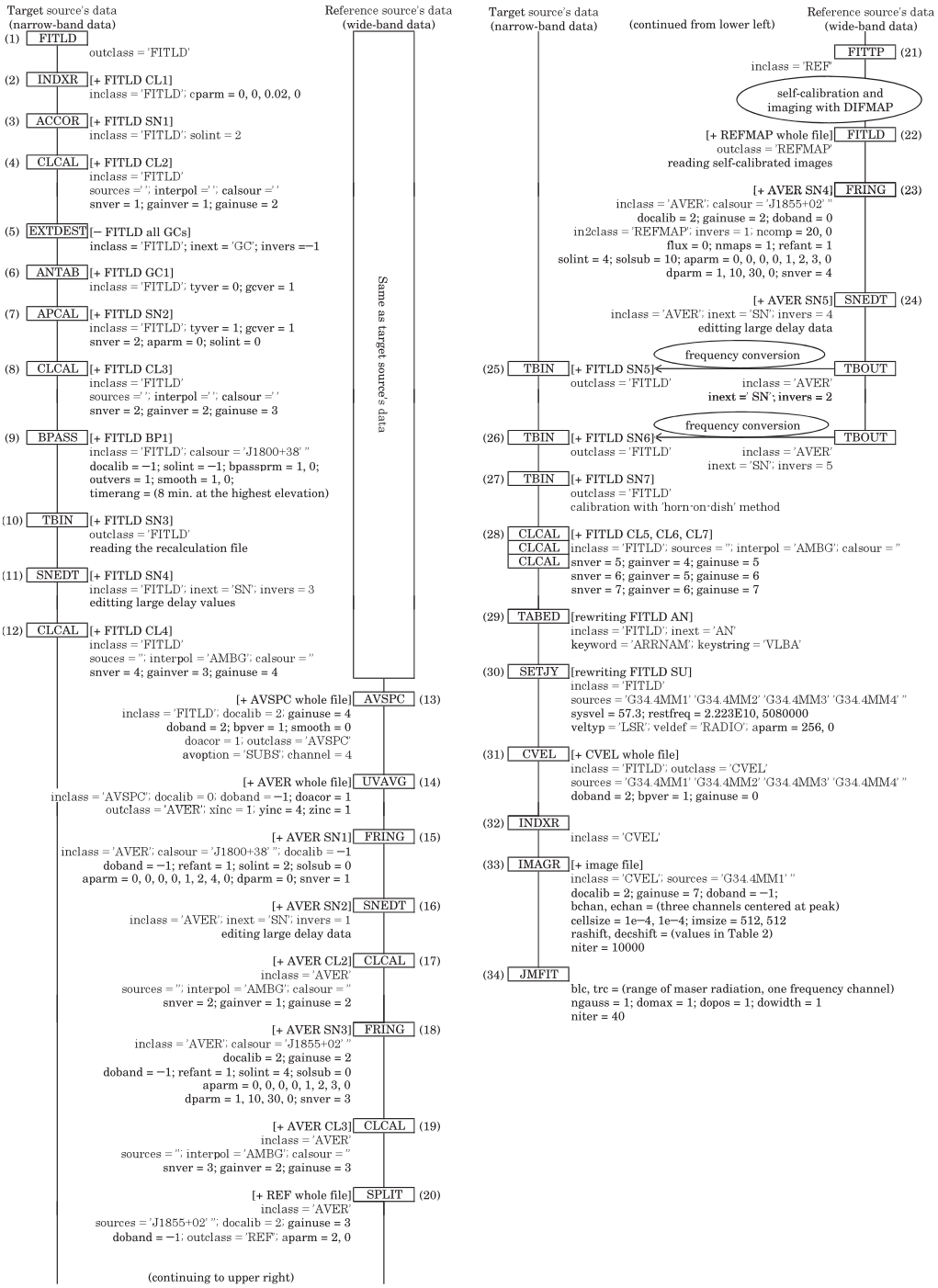

Figure 2.1: the flow chart of the typical data reduction procedure for VERA data

This is the flow chart of the typical data reduction procedure for VERA data shown in Kurayama et al. (2011).

3 Observations and Single-dish Data reduction

In this section, we summarized the observations of the three sources (RX Boo, RW Lep and NGC2264) mentioned in section 4 – 6. After we introduced the typical VLBI observations with VERA at first, we explain each sources and their single-dish observations with VERA Iriki station and Kahisma 34m telescope.

3.1 Typical VLBI Observations with VERA

VERA have the dual beam system to observe two different sources simultaneously and to cancel out the atmospheric fluctuations. One receiver to observe the target maser is called as A-beam and the other receiver to observe the position reference source is called as B-beam. The typical observations are 7 – 8 hours in total and the one observation is called as 1 epoch. In the observations, we observe the calibrator to calibrate the phase or delay time and to correlate in Mitaka FX correlator in first 5 minutes for each one tape. The the reference source must be located near the target maser ($< 2.2\ ^\circ$), which is constrained by the range of receiver's motion. Typically, we can observed two different maser or reference sources in 7 – 8 hours. To determine the parallax of the target source, we can choose the observation interval (one month or two months) or the observing month. Empirically, we observe for 1.5 months or more to measure the parallax, and there are twelve epochs more in the case of one month interval and excluding maintenance period. The data recording rate of 1024 Mbps was adopted with the VERA DIR2000 recording system, which yields a total bandwidth of 256 MHz with 2-bit digitization. The 256 MHz data of left-hand circular polarization were divided into 16 IFs, each of which had a bandwidth of 16 MHz. One IF was used to receive the maser emission and the others were used to receive the continuum emission. The correlation was carried out with Mitaka FX correlator (Chikada et al., 1991) at National Astronomical Observatory of Japan (NAOJ). The IF assigned to the water maser was divided into 512 spectral channels, yielding a frequency resolution of 31.25 kHz, corresponding to a velocity resolution of 0.42 $\mathrm{km\,s^{-1}}$. We can choose a frequency resolution of maser of 15.625 kHz or a velocity resolution of 0.21 km $\mathrm{s^{-1}}$ if we choose the bandwidth of 8 GHz to correlate. For the data of the reference source, each IF channel was divided into 64 spectral channels at all epochs.

3.2 VLBI Observations of RX Boo, RW Lep and NGC2264 with VERA

These three sources (RX Boo, RW Lep and NGC2264) were observed with VERA, and the observations are typical observations with one month interval. These observations are simply summarized in Table 3.1.

Table 3.1: Observations notes of RX Boo, RW Lep and NGC2264

Source	Starting date	Final date	total epoch	typical beam size
RX Boo	2008 February 19	2009 October 3	12	1.2 mas × 0.6 mas
RW Lep	2009 December 7	2011 December 24	18	1.5 mas × 0.7 mas
NGC2264	2009 September 20	2010 December 12	13	1.2 mas × 0.7 mas

3.2.1 RX Boo

We conducted monthly VLBI observations of water masers from February 2008 to October 2009 with VERA. We show the observation dates in Table 3.2. The duration of each observation was typically 8 hours, yielding an on-source integration time of 5 to 6 hours. Synthesized beam size (FWHM) was typically 1.2 mas×0.6 mas. To obtain positions of maser spots around RX Boo, we observed a continuum source J1419+2706 simultaneously as a position reference. The phase tracking center of RX Boo and J1419+2706 are $(\alpha_{J2000.0}, \delta_{J2000.0}) = (14^{\rm h}24^{\rm m}11^{\rm s}.6206, +25^\circ42'12''.909)$ and $(\alpha_{J2000.0}, \delta_{J2000.0}) = (14^{\rm h}19^{\rm m}59^{\rm s}.2971, +27^\circ06'25''.5530)$, respectively. The separation angle between two sources is $1^\circ.69$. In three observations, we did not detect any maser spot due to the bad weather conditions or the time variation of maser emission. Among twelve epochs, we used nine epochs that we detected a maser spot for the estimation of the annual parallax. In the seventh observation in 2009 January, Iriki station did not participate. In the ninth observation in 2009 March, Ogasawara station did not participate. The shape of the synthesized beam of ninth observation is different from those of the other observations. Data recording rate of 1024 Mbps was adopted with the VERA DIR2000 recording system, which yields a total bandwidth of 256 MHz with 2-bit digitization. The 256 MHz data of left-hand circular polarization were divided into 16 IFs which had bandwidth of 16 MHz. One IF is used to receive the maser emission and the others are used to receive the continuum emission from J1419+2706. The correlation was carried out with Mitaka FX correlator (Shibata et al., 1998) at National Astronomical Observatory of Japan (NAOJ). The rest frequency of 22.235080 GHz is adopted for water maser emission. The velocity resolution (ΔV) of the maser IF for each observation is also shown in table 3.2. In six observations, the IF assigned to the water maser was divided into 512 spectral channels, yielding a frequency resolution of 31.25 kHz, corresponding to a velocity resolution of 0.42 km s^{-1}. In the other observations, the maser IFs have bandwidths of 8MHz. They were divided into 512 spectral channels, yielding a frequency resolution of 15.625 kHz and a velocity resolution of 0.21 km s^{-1}. For the data of J1419+2706, each IF channel was divided into 64 spectral channels in all observations.

3.2.2 RW Lep

We performed VLBI observations of RW Lep, from December 2009 to December 2011, at 18 epochs spaced typically one month apart. The observations dates are summarized in Table 3.3. The duration of each observation was typically 8

Table 3.2: Observation dates of RX Boo

epoch	Date	Year/DOY	antennas†	ΔV ($\mathrm{km\,s^{-1}}$)‡
1	2008 February 19	2008/037	4	0.42
2*	2008 May 1	2008/121	4	0.21
3*	2008 June 11	2008/162	4	0.21
4*	2008 July 16	2008/197	4	0.21
5*	2008 November 11	2008/315	4	0.21
6*	2008 December 8	2008/342	4	0.21
7*	2009 January 10	2009/010	3	0.42
8*	2009 February 4	2009/035	4	0.21
9*	2009 March 12	2009/071	3	0.42
10*	2009 May 5	2009/125	4	0.42
11	2009 September 5	2009/248	4	0.42
12	2009 October 3	2009/276	4	0.42

* Observations used in the estimation of annual parallax.
† Total number of antennas joined the VLBI observation.
‡ Velocity resolution of the maser IF for each observation.

hours, yielding an on-source integration time of 5 to 6 hours. The synthesized beam size (full width at the half maximum) was typically 1.5 mas × 0.7 mas. To obtain the positions of the masers around RW Lep, we simultaneously observed a continuum source J0539−1550 as a position reference. The typical flux density of J0539 − 1550 was 240 mJy. The phase tracking centers of RW Lep and J0539 − 1550 were $(\alpha_{J2000.0}, \delta_{J2000.0})$=($05^{\mathrm{h}}38^{\mathrm{m}}52^{\mathrm{s}}.726$,$-14^{\circ}02'27''.18$) and $(\alpha_{J2000.0}, \delta_{J2000.0})$=($05^{\mathrm{h}}39^{\mathrm{m}}32^{\mathrm{s}}.010131$,$-15^{\circ}50'30''.32096$), respectively. The separation of the two sources is $1^{\circ}.81$. A data recording rate of 1024 Mbps was adopted using the VERA DIR2000 recording system, yielding a total bandwidth of 256 MHz with 2-bit digitization. The 256 MHz of left-hand circular polarization data were divided into 16 IFs, each with 16 MHz bandwidths. One IF was used to observe the maser emission from RW Lep and the other 15 IFs were used to receive the continuum emission from J0539−1550. The correlation was carried out with the Mitaka FX correlator (Chikada et al., 1991) at the National Astronomical Observatory of Japan (NAOJ). The rest frequency of water maser we observed was 22.235080 GHz. In all observations, the IF assigned to the water maser was divided into 512 spectral channels, yielding a frequency resolution of 15.625 kHz, corresponding to a velocity resolution of 0.21 $\mathrm{km\,s^{-1}}$. For J0539 − 1550 data, each IF channel was divided into 64 spectral channels in all observations.

3.2.3 NGC2264

We performed VLBI observations of the water masers around the region, NGC 2264, from 2009 September to 2010 December with VERA. With a time interval of 1 month between adjacent epochs, a total of 13 epochs of observations were carried out. The observation dates are shown in Table 3.4. The duration of

Table 3.3: Observation dates of RW Lep

epoch	Date	MJD[a]	Note[b]
1	2009 December 7	55172	U
2	2010 January 26	55222	U
3	2010 March 2	55257	U
4	2010 May 3	55380	N
5	2010 May 14	55391	N
6	2010 July 24	55432	N
7	2010 September 26	55465	N
8	2010 November 3	55503	U
9	2010 November 28	55528	U
10	2010 December 22	55552	U
11	2011 January 24	55585	U
12	2011 February 12	55604	U
13	2011 April 22	55673	U
14	2011 August 16	55791	N
15	2011 September 12	55816	N
16	2011 October 16	55851	N
17	2011 November 28	55893	N
18	2011 December 24	55919	N

[a] Modified Julian Day
[b] This shows whether we used the epoch to estimate the annual parallax, where "U" indicates 'used' and "N" indicates 'not used' in the estimation of annual parallax.

each of observation epochs was typically 8 hours, yielding an on-source integration time of 5 – 6 hours. The average full width at the half maximum of the synthesized beam size ($\theta_{\rm beam}$) was 1.19 mas × 0.66 mas (see Table 3.4 of the synthesized beam of each observation epoch). J0643+0857 (a position reference continuum source) was simultaneously observed with the maser source, and its average flux density over all the epochs of is 508 mJy. During our observations, the size and shape of the image of J0643+0857 did not change significantly. The phase tracking center of NGC 2264 and J0643+0857 were $(\alpha_{\rm J2000.0}, \delta_{\rm J2000.0}) = (6^{\rm h}41^{\rm m}9^{\rm s}86, +9^\circ29'14''.7)$ and $(\alpha_{\rm J2000.0}, \delta_{\rm J2000.0}) = (6^{\rm h}43^{\rm m}26^{\rm s}.445000, +8^\circ57'38''.01338)$, respectively. The separation angle between these two sources is $0^\circ.53$. In four epochs, we did not detect any maser spot due to either bad weather conditions or time variability of the maser emission. Among thirteen epochs, we used nine epochs to estimate the annual parallax and proper motions. The data recording rate of 1024 Mbps was adopted with the VERA DIR2000 recording system, which yields a total bandwidth of 256 MHz with 2-bit digitization. The 256 MHz data of left-hand circular polarization were divided into 16 IFs, each of which had a bandwidth of 16 MHz. One IF was used to receive the maser emission and the others were used to receive the continuum emission from J0643+0857. The correlation was carried

out with Mitaka FX correlator (Chikada et al., 1991) at National Astronomical Observatory of Japan (NAOJ). The rest frequency of 22.235080 GHz is adopted for water maser emission. The velocity resolution of the maser IF for each observation is also shown in Table 3.4. In 11 of 13 epochs, the IF assigned to the water maser was divided into 512 spectral channels, yielding a frequency resolution of 31.25 kHz, corresponding to a velocity resolution of 0.42 km s^{-1}. In the other 2 epochs, the maser IF had a bandwidth of 8 MHz, which was divided into 512 spectral channels, yielding a frequency resolution of 15.625 kHz or a velocity resolution of 0.21 km s^{-1}. For the data of J0643+0857, each IF channel was divided into 64 spectral channels at all epochs.

Table 3.4: Observation dates of NGC2264

epoch	Date	MJD[b]	Synthesized beam[c] [mas] ×[mas]	P.A.[d] [deg]	ΔV[e] [km s^{-1}]
1[a]	2009 September 20	55094	1.27 × 0.67	135	0.21
2[a]	2009 October 19	55123	1.25 × 0.65	140	0.42
3[a]	2009 November 19	55154	1.16 × 0.70	134	0.42
4[a]	2010 January 8	55204	1.19 × 0.68	132	0.42
5[a]	2010 February 1	55228	1.19 × 0.65	135	0.42
6[a]	2010 March 8	55263	1.21 × 0.60	133	0.42
7[a]	2010 April 30	55289	1.23 × 0.67	131	0.42
8[a]	2010 May 25	55341	1.20 × 0.65	136	0.42
9[a]	2010 August 16	55424	1.14 × 0.65	138	0.42
10	2010 September 15	55454	1.09 × 0.78	127	0.42
11	2010 October 16	55485	1.17 × 0.66	136	0.42
12	2010 November 13	55513	1.22 × 0.65	124	0.21
13	2010 December 12	55542	1.16 × 0.62	130	0.42

[a] Observations used in the estimation of annual parallax and the proper motions.
[b] Modified Julian day.
[c] The major and minor axial lengthes of the synthesized beam.
[d] The position angle (P.A.) of the synthesized beam.
[e] The velocity resolution of the maser IF for each observation.

3.3 VERA Iriki Single-dish observations and Data Reduction

We monitored RX Boo from October 2005 to July 2014 with VERA Iriki telescope and RW Lep from September 2005 to February 2013. The 64 single-dish observations are conducted with the velocity resolution of 0.21 km s^{-1} or 0.42 km s^{-1}. Basically, we integrated the files if the data files were separated and did baseline fitting. The data were reduced with Newstar package or Spectruman software. Newstar package was developed by Nobeyama radio observatory and Spectruman software was developed by Kagoshima university. Spectruman software is automated and specialized to do these procedures of water maser

observed by VERA Iriki single-dish.

3.4 NH_3 observations and Data Reduction with the Kahima 34m Telescope

To figure out the distribution of the dense molecular gas and to derive its physical property, we made mapping observations in the NH_3 emission lines. We performed NH_3 observations for NGC2264 region with Kashima 34 m telescope of National institute of Information and Communications Technology (NICT). The observations were conducted from 2007 May to 2008 January. We made simultaneous observations in three inversion transitions of the NH_3 (J, K) = (1,1), (2,2) and (3,3) lines at 23.694495, 23.722633 and 23.870129 GHz, respectively. At 23 GHz, the telescope beam-width is $1'.6$ and the main beam efficiency ($\eta_{\rm MB}$) is 0.50. We used a 22GHz-band HEMT amplifier whose system noise temperature is 150–250 K. All spectra were obtained with a 8192-channel FX-type spectrometer developed by the Kagoshima University and NiCT. This spectrometer has a bandwidth of 256 MHz and frequency resolution of 31.25 kHz. At the NH_3 frequencies, these correspond to 3200 km s^{-1} velocity coverage and 0.39 km s^{-1} velocity resolution. The surveyed area is about $16' \times 19'$, around $\alpha_{J2000} = 06^{\rm h}41^{\rm m}10^{\rm s}.2$, $\delta_{J2000} = 09°29'34''$. We set a grid spacing to $1'$ along the equatorial coordinates. The total number of observation points is 186. All data were obtained in the position switching mode between the target and reference positions. The reference position were located at $\alpha_{J2000} = 06^{\rm h}41^{\rm m}46^{\rm s}.7$, $\delta_{J2000} = 09°32'34''$, where NH_3 emission is free. We integrated at least 10 minutes at each point. The relative pointing error was better than $0'.2$, which was checked by the observations of several H_2O maser sources at 22.235080 GHz.

Data reduction was performed using the UltraSTAR package developed by the radio astronomy group at the University of Tokyo (Nakajima et al., 2007). The rms noise level is typically 0.095 K in the unit of the main beam temperature defined by $T_{\rm MB} \equiv T_{\rm A}^*/\eta_{\rm MB}$, where $T_{\rm A}^*$ is the antenna temperature calibrated by the chopper wheel method (Kutner & Ulich , 1981). In this paper the intensities are presented in the main beam temperature.

4 Distance toward the Multi Period Pulsating Semi-Regular Variable (SRV) Star, RX Bootis

4.1 Introduction

Some of evolved stars have water, SiO and OH maser emissions in their envelopes. We can obtain parallaxes toward the stars when we observed these masers. Therefore, we observed the evolved stars, and we show the results of the parallax measurements and the discussions based on the parallax measurements. We only observed water maser emissions around the stars, but it is convenient to understand the stellar properties with the other lines. In this section, we introduced Asymptotic Giant Branch (AGB) stars, the evolved stars, Period Luminosity (PL) relation and the target star, RX Bootis.

4.1.1 AGB stars

We explain of Asymptotic Giant Branch (AGB) stars, which is the closing stage of the stellar evolution. The low-mass stars leave the main sequence and their luminosities increas with their hydrogen burnings. The mass of central core composed of Helium increase with their hydrogen burnings. When the helium cores begin to burn, the temperatures increase and the luminosities decrease and they evolve to red clump stars or horizontal branch stars. Red Giant Branch (RGB) stars are located before and after beginning of helium core burnings. The horizontal branch stars go through the Cepheid instability strip and we call the horizontal branch stars in the cepheid instability strip as "RR Lyr" variable stars. After finishing the burning of helium core, their luminosities are increasing again and then they are located near positions of RGB stars. The routes of these stars are asymptotic to the route from RGB to horizontal branch stars on Hertzsprung-Russell (HR) diagram, we call these stars as Asymptotic Giant Branch (AGB) stars. These route is shown in Figure 4.1.

AGB stars include supergiant and giant in HR diagram. Supergiant stars evolve from massive main sequence star without going through the horizontal branch and RGB phase. These stars are included AGB stars because we cannot distinguish them from low-mass evolved stars on the HR diagram, and most of them are included in SRc variable stars as mentioned in next sub-subsection.

4.1.2 Long Period Variable Stars

Long Period Variable (LPV) stars are composed of Mira, Semi-Regular varriable (SRV), irregular variable stars. All these stars are evolved stars and they have long periods. In LPVs, Mira is a famous variable star, which has regular light curve caused from regular pulsating of the stars. The definitions are shown in General Catalog of Variable Stars (GCVS) and is shown as "These are long-period variable giants with characteristic late-type emission spectra (Me, Ce, Se) and light amplitudes from 2.5 to 11 mag in V. Their periodicity is well

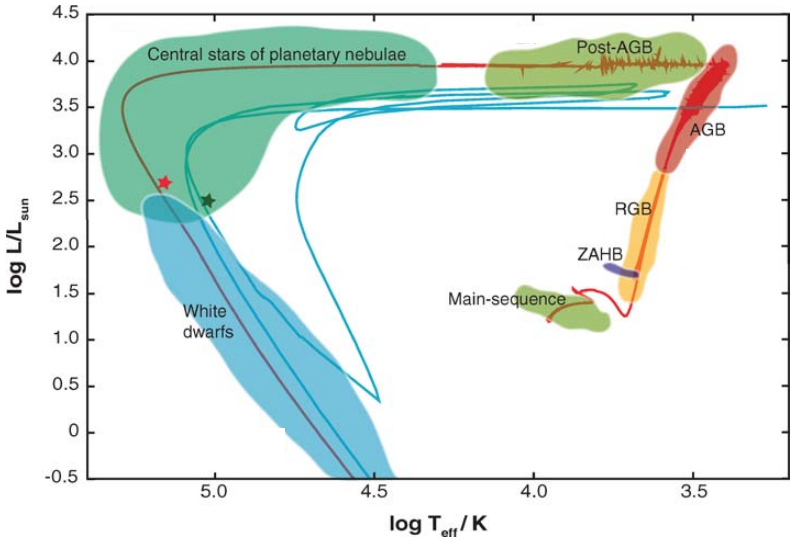

Figure 4.1: The evolutionary track of low-mass stars
The evolutionary track of low-mass stars shown on the HR diagram (Herwig, 2005).

pronounced, and the periods lie in the range between 80 and 1000 days.". Their variation is considered as being caused from the pulsation of the central star.

SRVs are divided into four sub-classes (a, b, c and d). Type-a SRV (SRa) has regular light curve, same spectral type, same luminosity class similar period to Mira. However, they have small amplitude lower than 2.5 mag in V band. The threshold 2.5 mag in V band is mentioned in Section 4.1.1. Type-b SRV (SRb) has irregular light curve and they often have multi-period. Mattei et al. (1997) suggested that new classification of Mira and SRVs and they suggested that SRb should be called as semi-regular variable star. Type-c SRV (SRc) is supergiant and has long period. Since massive star comes onto the AGB position in HR diagram on the way of their evolution, they classified in SRV. For example, VX Sagittarii or Betelgeuse is famous. Type-d SRV (SRd) has warmer spectral type (F, G, K). SRd stars have not well studied.

Irregular variable star has clearly irregular light curve and they are divided into two types: Lb and Lc. They are distinguished by their spectral classes and Lb is giant and Lc is supergiant. Lebzelter & Obbrugger (2009) suggested that the Lb variable stars are extension of SRb towards shorter periods and smaller amplitudes based on their period analysis.

Most of LPVs are considered as pulsating variable star (e.g. Miras are pulsating with period of 300 days), excepting Lc and SRd since their varying reason is unclear. They eject their materials by their stellar wind or pulsation and the ejected material are observed with mid-, far-infrared or ultra violet band (Mayer et al., 2011; Cox et al., 2012). The morphology of the ejected materials is various (arc, ring, eye, irregular and so on). These morphologies is very complex and how the shapes were made is under discussion (contribution of binary? or outflow?, etc).

4.1.3 Period – Luminosity (PL) Relations

Many periodic variable stars, which is composed of many pulsating variable stars, have Period – Luminosity (PL) relations. PL relation of Mira was found from the observations toward Large Magellanic Cloud (LMC) by Glass & Evans (1981). From this finding, we obtained the way to estimate the distance to the mass-loss stars. In PL relation, Wood & Sebo (1996); Wood (2000) showed that there are several sequences. These sequences are different by their variable type or pulsating mode (Ita et al., 2004). Wood (2000) labelled the sequences from A to E. We showed the figure of Wood (2000) and the PL relations revised by Ita et al. (2004) in Figure 4.2. The sequence C has been well-studied by Feast et al. (1989) and is the sequence of fundamental mode pulsating Miras. The sequence B was relabeled as the sequence C$'$ by Ita et al. (2004) and is the sequence of first overtone mode pulsating Mira and SRVs. They discussed the sequences, especially longest sequence D. The sequence D is much longer than that of sequence C. Since the fundamental mode pulsators distribute on sequence C, the sequence D may be the sequence of non-pulsating variable and the periods are not caused by pulsation. The periods located on the sequence D were the periods called as "Long Secondary period (LSP)", which are much

longer than their primary periods. What causes LSP ? Although they implied two scenarios (binary and strange pulsating mode), the causes are still unknown in 2013 (Soszyński & Wood, 2013).

The studies of PL relation have been done not only for LMC but also the MilkyWay Galaxy (MWG). When we determined the PL relations of LMC, we assumed that all stars have same distance. It is a reasonable assumption, since the geometrical thickness of LMC along the line of sight is much smaller than the distance to LMC. However, we cannot use this assumption for stars in MWG, because the distance to each variable star in MWG is significantly different. Therefore, we need the precise distance to each star. The way to measure the distance each stars is very difficult and needs many times. HIgh Precision PARallax COllecting Satellite (Hipparcos) made a breakthrough of the problem by measuring the parallaxes of many stars including variable stars. Although many papers discussed the PL relations of LPVs (e.g. Whitelock & Feast (2000); Yeşilyaprak & Aslan (2004); Glass & van Leeuwen (2007); Whitelock et al. (2008)), it is not determined well because the number of sources with accurate distances is limited. So, more studies on the distance of the pulsating variable stars are required to establish the precise relation. To investigate the PL relations in MWG with sufficient precision, we need more variable stars with accurate distances. Now, the accurate distance can be obtained with Very Long Baseline Interferometry (VLBI) although it limits the LPVs with maser emissions and existing reference sources. Once we get the PL relation, we easily use it and we can obtain the distance to LPVs regardless of its maser emissions. Hence, the determinations of PL relations is very important.

4.1.4 RX Bootis

RX Bootis (RX Boo) is a type-b Semiregular (SRb) variable star, which has an irregular visual light curve. SRb stars are typical SRVs and they often have muti-periods. RX Boo is the very SRb variable star because RX Boo has irregular light-curve and multi-periods. RX Boo has multi-periods of shorter ($\sim$ 170 days) and longer ($\sim$ 300 days) although we discuss the periods below (section 3.4). In addistion to these periods, Mattei et al. (1997) have also suggested the existence of the third period of 2691.837 day without confirmation. The optical light curve of RX Boo is shown in Figure 4.3.

Winnberg et al. (2008) monitored the water maser emissions of RX Boo over twenty years with single-dish observations using Effelsberg 100-m and Medicina 32-m telescopes. They also observed water masers in RX Boo using the Very Large Array (VLA) on four occasions in the period from 1990 to 1992 and later in 1995. Then they revealed the distribution of water masers around RX Boo shown in Figure 4.4. They detected the emission of incomplete shell around RX Boo (see Figure 4.4). The inner radius of the shell is estimated to be 15 AU. They conclude that the variability of water masers around RX Boo is due to the appearance and disappearance of maser clouds with a lifetime of $\sim$1 year. With infrared interferometers, the angular diameter of RX Boo is estimated as 18.4 $\pm$ 0.5 mas and 21.0 $\pm$ 0.3 mas in K band (2.2 μm) and L'

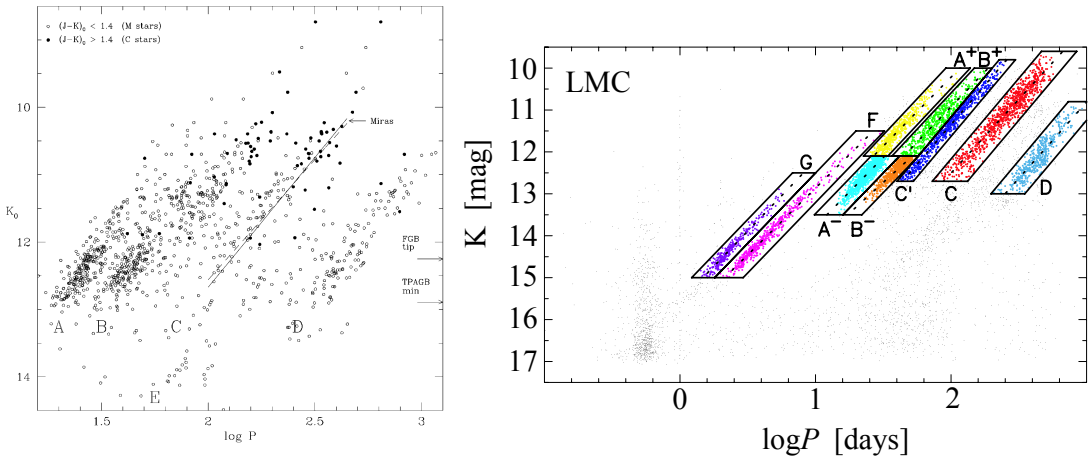

Figure 4.2: Period – Luminosity (PL) relations
Period – Luminosity (PL) relations. The left panel is Wood (2000)'s fist shown multiplicity of PL relations and the right panel is revised PL relations shown in Ita et al. (2004). Both were label their identified sequences and their labeling alphabets are different. Their vertical axis is K_0 magnitude which is K band apparent magnitude corrected for the reddening since they assumed that all stars have the same distance.

band (3.8 μm), respectively, with the model of uniform disks (Dyck et al., 1996; Chagnon et al., 2002). We can convert these apparent sizes to actual sizes by using distance. RX Boo emits SiO and OH masers as well as water masers (Boboltz & Claussen, 2004; Szymczak et al., 1995). The annual parallax of RX Boo was measured to be 6.42 ± 1.00 mas by Hipparcos (Perryman et al., 1997). From CO observations, Olofsson et al. (2002) estimated its mass-loss rate and expansion velocity of $6 \times 10^{-7} M_{\odot}\,\mathrm{yr}^{-1}$ and $9.3\,\mathrm{km\,s}^{-1}$, respectively. Teyssier et al. (2006) also obtained the values of $2 \times 10^{-7}\,M_{\odot}\,\mathrm{yr}^{-1}$and $7.5\,\mathrm{km\,s}^{-1}$ from CO observations.

4.2 Single-dish Results

The all single-dish spectra are shown in Figure 4.11 to Figure 4.11. VLBI observations were conducted from February 2008 to Ocotber 2009, the flux of water maser emission increases twenty-times more than that of previous emissions. The water maser emissions were seen from $\Delta V = -5$ km s^{-1} to $+10$ km s^{-1}. In the single-dish monitoring, the water masers sometimes increased, but the increasing components were differnet at any given times. In the case of our maser spot which is used to measure the annual parallax, it did not become stronger

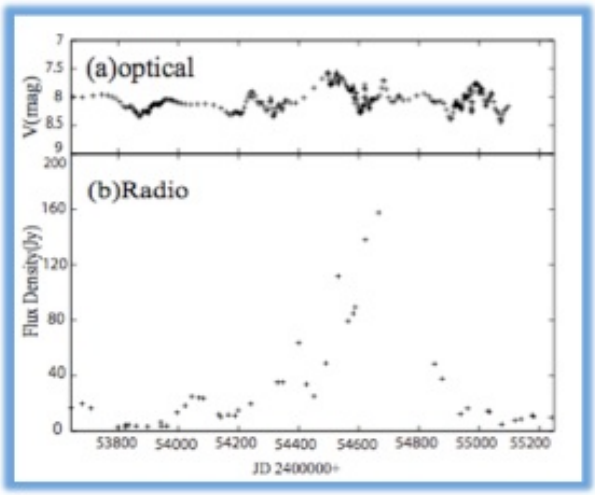

Figure 4.3: The light curves of RX Boo
The light curves of optical band (a:top) and water maser (b:bottom). The optical light curve is obtained with moving average of the data from Association Française des Observateurs d'Etoiles Variables (AFOEV) and the peak-intensity water maser light curve is obtained from the single-dish observations with VERA Iriki telescope.

with the increase of the flux in spectrum (see Table 4.1). This impies that water masers were resolved out because of the near distance, which is shown as below.

4.3 VLBI Results

4.3.1 Cross-power Spectra and Maser Images

We obtained the time variation of cross-power spectra of RX Boo as shown in Figure 4.12. From this figure, we found the LSR velocity of the peak did not change among our VLBI observations. This component was $V_{\rm LSR} = 3.2\,{\rm km\,s^{-1}}$ and had been strong before our observations, as seen in Winnberg et al. (2008). Several frequency channels at which we detected masers were imaged. Obtained images of water masers at a LSR velosity of $3.2\,{\rm km\,s^{-1}}$ are shown in Figure 4.13. Although the maser has a small change of the structure, it did not affect the parallax measurements.

4.3.2 Position Uncertainty in each epoch

It is very important to determine the position error of each epoch because it affects the fitting for the annual parallax of RX Boo. So, we explain the position error of each epoch before least square analysis for the annual parallax. The

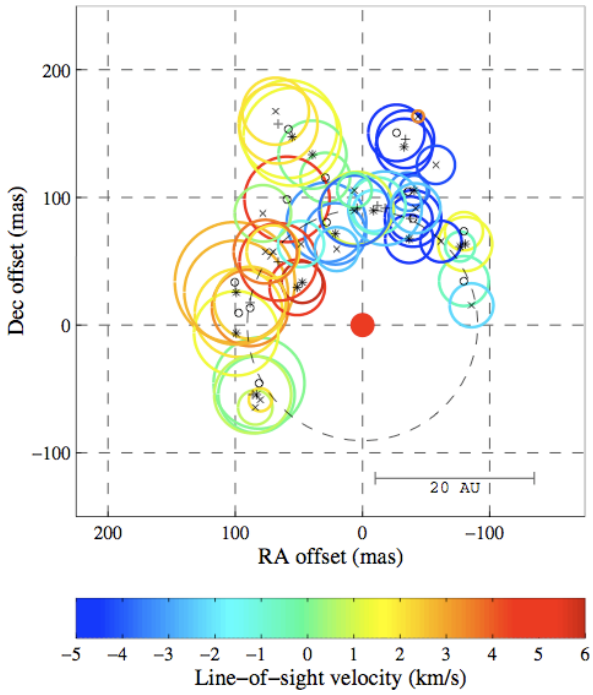

Figure 4.4: Water maser distributions around RX Boo
Water maser distributions around RX Boo shown in Winnberg et al. (2008). Using VLA, they detected more than 50 spots in four epoch. Each component is represented by a symbol and a circle whose diameter is logarithmically proportional to the flux density of the component. The epochs are represented by different symbols: 1990 February by small circles; 1990 June by asterisks; 1991 October by plus signs; 1992 December by crosses.

position error of each measurement was estimated from the root sum square of the following three error factors: (1) the airmass effect σ_A, (2) the errors in station positions σ_S, and (3) the quality of images σ_I. After the calibration of airmass effect in the delay tracking model, there still remains an uncertainty of about 3 cm in the zenith direction (Nakagawa et al., 2008; Honma et al., 2007). Therefore, the error from factor (1) is estimated to be σ_A =80–110 μas (Nakagawa et al., 2008; Honma et al., 2007). Station positions are determined to be an accuracy of $\sim$3 mm based on geodetic observation (Nakagawa et al., 2008; Honma et al., 2007), the error from factor (2) was estimated to be $\sigma_S = 8\,\mu$as. We estimate the error from factor (3) from $\sigma_I = \theta_b/\mathrm{SNR}$, where θ_b is a root sum square of major and minor axes of the synthesized beams and SNR is a signal-to-noise ratio in the phase referenced image of the maser. Because SNR was affected by observational condition and intensity variation of the maser, the error was estimated to be σ_I = 50–250 μas. Thus, the error of each observation

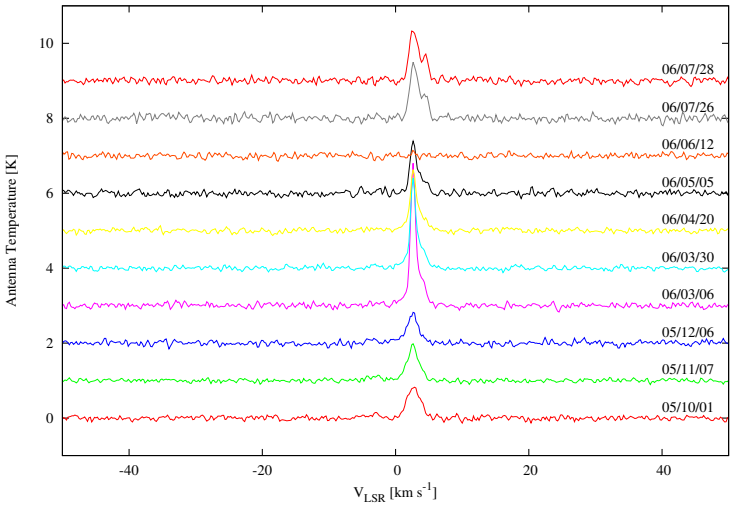

Figure 4.5: Water maser spetra of RX Boo obtained with VERA Iriki Single dish observations 1

The single-dish spectra of RX Boo observed from October 2005 to July 2006 with VERA Iriki telescope. We showed the observed date in right of the spectra.

was estimated to be 110–300 μas by taking root sum squares of these factors. The errors are shown in Table 4.1 and figure 4.14 and 4.15 as the error bars. In addition to these three error factors, we can consider error raised by maser structure. This error factor is smaller than 110–300 μ as of $\sigma_{\Delta\alpha\cos\delta}$ or $\sigma_{\Delta\delta}$. In Table 4.1, there are positions, errors in the positions, peak Intensity S and SNRs of detected maser spot in each epoch, where positions are relative offsets from the position of the maser in the 2nd epoch.

4.3.3 Annual Parallax

In order to obtain the annual parallax, we adopted the assumptions that the maser spot has no acceleration and the reference source is fixed on the sky.

We conducted the weighted least square fitting analysis. Its weights are based on the position errors. The error in each epoch is shown in table 4.1. To calculate the parallax, we used maser spots which have sufficient signal-to-noise ratios on the phase-referenced images (SNR > 5). Only one maser spot with $V_{\rm LSR} = 3.2\,{\rm km\,s^{-1}}$ is selected with this criterion. We performed the least square fitting by using the following equations;

$$\Delta\alpha\cos\delta = \varpi(-\sin\alpha\cos\lambda_\odot + \cos\epsilon\cos\alpha\sin\lambda_\odot) + (\mu_\alpha\cos\delta)t + \alpha_0\cos\delta \quad (4.1)$$

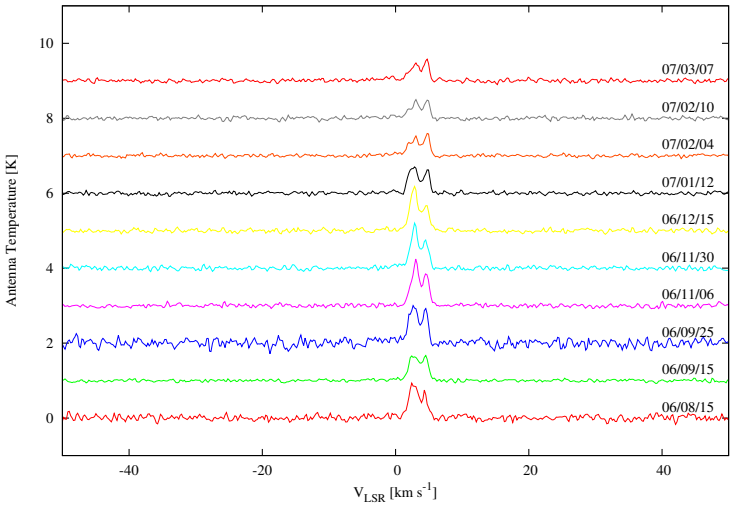

Figure 4.6: Water maser spetra of RX Boo obtained with VERA Iriki Single dish observations 2

Same as Figure , but from August 2006 to March 2007.

$$\Delta\delta = \varpi(\sin\epsilon\cos\delta\sin\lambda_\odot - \cos\alpha\sin\delta\cos\lambda_\odot - \cos\epsilon\sin\alpha\sin\delta\sin\lambda_\odot) + \mu_\delta t + \delta_0, \tag{4.2}$$

where $(\Delta\alpha\cos\delta, \Delta\delta)$ are the displacements of the observed maser spot, $(\mu_\alpha\cos\delta, \mu_\delta)$ are the linear motions of the maser around RX Boo, t is time, ϖ is the annual parallax, (α, δ) are the right ascension and declination of the source, $\lambda_\odot$ is ecliptic longitude of the Sun, ϵ is the obliquity of the ecliptic and (α_0, δ_0) is the right ascension and the declination when $t = 0$. In this fitting, we derived five parameters; $\varpi, \mu_\alpha\cos\delta$, μ_δ, α_0 and δ_0. The total number of data is eighteen (right ascension and declination of nine epochs).

In Figure 4.14 and 4.15, we showed observed positions and results of the fitting. In Figure 4.14, we present the motion of one maser spot with $V_{\rm LSR} = 3.2$ km s^{-1} with respect to the phase tracking center. In Figure 4.15, parallactic motion in right ascension and declination are presented. The apparent motion clearly shows an effect of parallactic motion. Based on the least square fitting analysis, the annual parallax was determined to be 7.31 ± 0.50 mas, corresponding to the distance of 136^{+10}_{-9} pc. This is the nearest distance measured with VERA as of 2014. The proper motion of the spot was $(\mu_\alpha\cos\delta, \mu_\delta) = (24.55 \pm 1.06\,{\rm mas\,yr^{-1}}, -49.67 \pm 2.38\,{\rm mas\,yr^{-1}})$.

4.3.4 Comparison with the Previous Results

Here, we compare our results with previous results. In table 4.2, our results and Hipparcos' results are summarized. In comparison with Hipparcos' parallax,

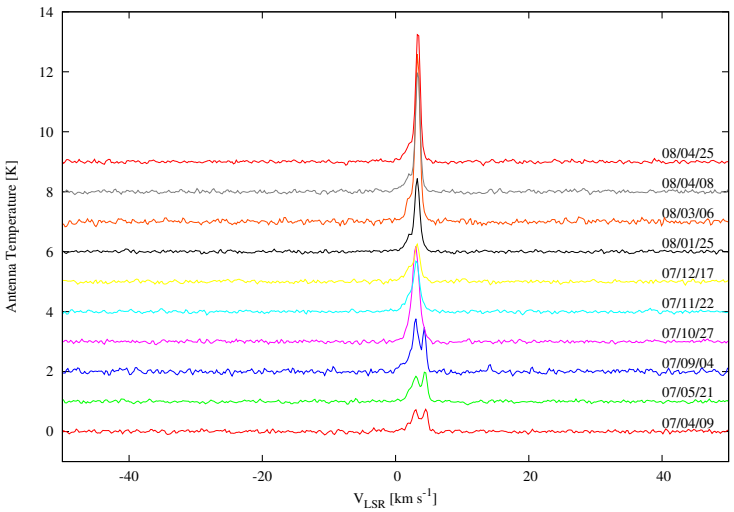

Figure 4.7: Water maser spetra of RX Boo obtained with VERA Iriki Single dish observations 3

Same as Figure , but from April 2007 to April 2008.

$\varpi_{\rm HIP} = 6.42 \pm 1.00$ mas, our parallax is consistent with the Hipparcos' parallax. According to Hipparcos' result, the proper motion of RX Boo is $(\mu_\alpha \cos\delta,\ \mu_\delta) = (21.74 \pm 0.90\,{\rm mas\,yr^{-1}}, -49.70 \pm 0.49\,{\rm mas\,yr^{-1}})$. In the declination component, the proper motion from our analysis is consistent with the result from Hipparcos, but in the right ascension component, the motion is $2.81\,{\rm mas\,yr^{-1}}$ larger than Hipparcos' result. This difference of the proper motions between Hipparcos' and ours corresponds to $1.8\,{\rm km\,s^{-1}}$ at the distance of RX Boo. We think that this is the velocity of the maser motion with respect to the star itself. From CO observations, the LSR velocity of the star is 1.0 $\rm km\,s^{-1}$ (Teyssier et al., 2006). The difference of the LSR velocities between the star and the water maser is 2.2 $\rm km\,s^{-1}$. The difference of the proper motions between Hipparcos' and ours is almost as large as that of the LSR velocities between the star and the water maser. The difference of the proper motions between Hipparcos' and ours may be caused by the motion of the maser spot with respect to the star itself.

From the directions of the proper motion and the radial velocity, we can know the positional relationship between the maser and star. The proper motion of the maser with respect to the central star is $(\mu_\alpha \cos\delta, \mu_\delta) = (2.81\ {\rm mas\ yr^{-1}}, 0.03\ {\rm mas\ yr^{-1}})$ and directs the position angle of 89°.4. The position angle of the maser is 89°.4 with respect to the central star. We expect that this maser is located in east direction for the central star. This is consistent with the result of VLA (Winnberg et al., 2008) and their detected masers which had the similar radial velocity distributed in the same direction.

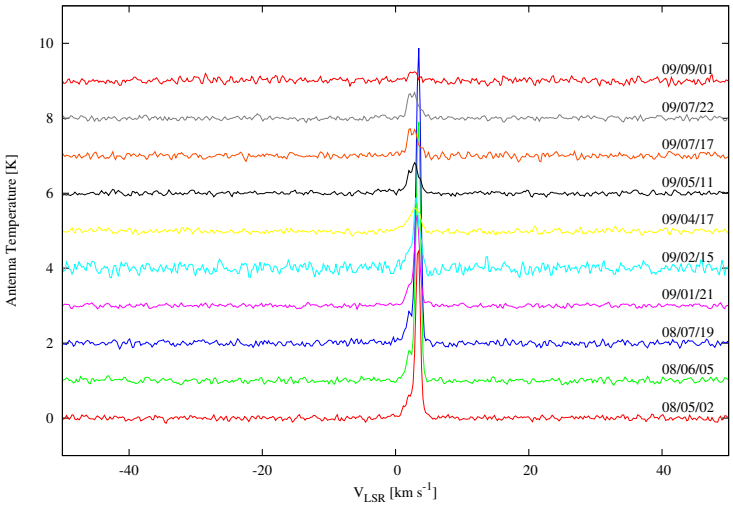

Figure 4.8: Water maser spetra of RX Boo obtained with VERA Iriki Single dish observations 4

Same as Figure , but from May 2008 to September 2009.

Winnberg et al. (2008) considered out-flow model of water maser using data observed with VLA. They assumed the model that water masers were accelerated exponentially and expanded spherically. Based on this assumption, they showed a relationship between expansion velocities and the three-dimensional distances from the central star to the masers;

$$r = r_0 - \frac{1}{k}\ln\left(1 - \frac{v}{v_f}\right), \tag{4.3}$$

where r is three-dimensional distance from the central star to the maser, $k = 0.065\,\mathrm{AU}^{-1}$, $r_0 = 1.5\,\mathrm{AU}$ is the radius at which expansion velocities are zero, $v_f = 8.4$ km s^{-1} is the largest expansion velocity, and v is the expansion velocity of masers. By using their model, we can estimate the three-dimensional distance from central star to the maser. On the celestial plane, the difference of proper motion between the maser and the central star is 2.8 mas yr^{-1}. This corresponds to 1.8km s^{-1}. The difference of the radial velocities is 2.2km s^{-1}. From these, the expansion velocity is $v = \sqrt{1.8^2 + 2.2^2} = 2.8$ km s^{-1}. From equation 4.3, we obtained the three-dimensional distance from central star to be 7.9 AU. This distance is smaller than the inner radius of the detected incomplete ring structure by Winnberg et al. (2008).

Table 4.1: parameters of a detected maser spot in each epoch

epoch	$\Delta\alpha\cos\delta$[mas]*	$\sigma_{\Delta\alpha\cos\delta}$[mas]†	$\Delta\delta$[mas]*	$\sigma_{\Delta\delta}$[mas]†	S[Jy beam^{-1}]‡	SNR
2	0.00	0.11	0.00	0.11	6.4	25.95
3	−0.52	0.12	−5.43	0.12	2.3	14.32
4	−2.03	0.15	−5.75	0.15	4.8	11.29
5	14.93	0.14	−34.18	0.14	3.6	16.92
6	20.02	0.12	−38.10	0.12	6.2	21.33
7	23.91	0.11	−41.48	0.11	2.1	14.92
8	26.03	0.13	−43.85	0.13	2.0	14.59
9	28.28	0.29	−49.64	0.29	0.8	8.41
10	24.56	0.26	−44.84	0.26	3.4	5.38

* Right Ascension and declination offsets from $(\alpha_{J2000.0},\ \delta_{J2000.0}) = (14^{\rm h}24^{\rm m}11^{\rm s}.6206,\ +25^\circ42'12''.906)$.
† Position errors in right ascension and declination.
‡ Peak fluxes of the maser spots.

Table 4.2: our results and Hirrarcos' results

	Our result	Hipparcos*
$\varpi^\dagger$	7.31±0.50 mas	6.42±1.00 mas
$\mu_\alpha\cos\delta^\ddagger$	$24.55 \pm 1.06\,{\rm mas\,yr^{-1}}$	$21.74 \pm 0.90\,{\rm mas\,yr^{-1}}$
$\mu_\delta^\ddagger$	$-49.67 \pm 2.38\,{\rm mas\,yr^{-1}}$	$-49.70 \pm 0.49\,{\rm mas\,yr^{-1}}$

* Data from Perryman et al. (1997)
† Annual parallax.
‡ proper motions.

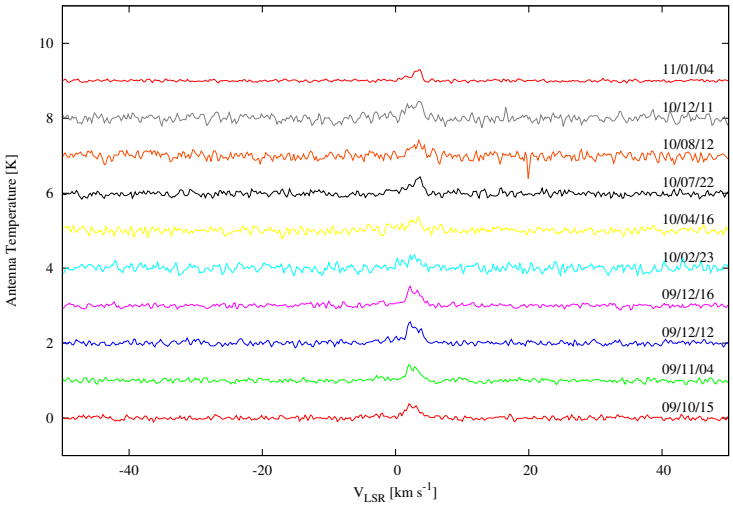

Figure 4.9: Water maser spetra of RX Boo obtained with VERA Iriki Single dish observations 5

Same as Figure , but from October 2009 to January 2011.

4.4 RX Bootis on the PL Plane

The parallax 7.31 ± 0.50 mas obtained as above gives the distance modules of -5.68 mag. We apply this to assume the absolute magnitude of RX Boo. For RX Boo Glass & van Leeuwen (2007) used the apparent K magnitude m_K of -1.85 mag based on the observation by Lloyd Evans and the parallax of 4.98 ± 0.64 mas derived from the revised Hipparcos Catalogue (van Leeuwen & Fantino, 2005; van Leeuwen, 2007). Their values gave the absolute magnitude M_K of $-8.36^{+0.26}_{-0.30}$ mag. Our new parallax gives M_K of $-7.53^{+0.14}_{-0.15}$. This magnitude may have also the probable error about 0.4 mag or less as indicated in Glass & van Leeuwen (2007).

The period of variable stars classified as semi-regular (SR) is difficult to determine precisely. In 1980s, Taylor (1987) reported the existence of two periods, 160.0 d and 302.0 d, for RX Boo. Andronov & Kudashkina (1988) obtained several periods based on their observational results. In the General Catalogue of variable Stars (GCVS) by Samus et al. (2009) the period of 162.3 d is tabulated for RX Boo, although Glass & van Leeuwen (2007) used 340 d indicated in the former version of GCVS. The period of 162.3 d is based on Mattei et al. (1997). Mattei et al. (1997) give the period of 304.7 d together with 162.3 d adopted in GCVS. They have also suggested the existence of the third period of 2691.837 d without confirmation. A recent paper by Speil (2006) gives also the double-periodicity of 278.0 and 169.6 d. Because of the uncertainty of the period determination for the semiregular variables, it is difficult to judge which

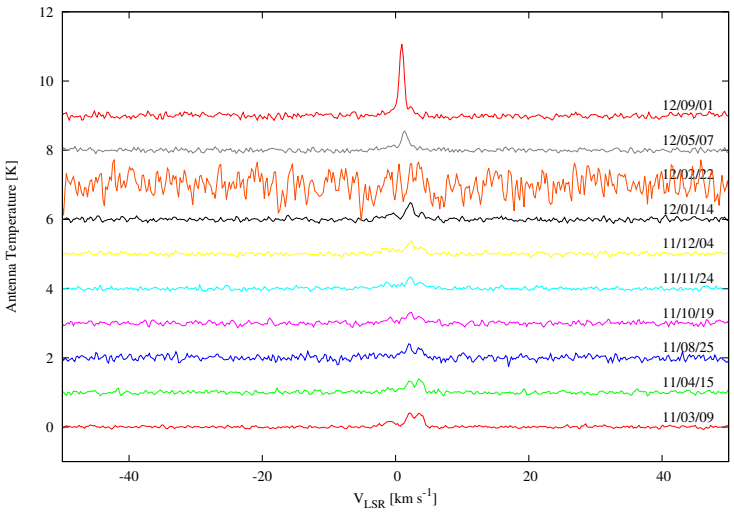

Figure 4.10: Water maser spetra of RX Boo obtained with VERA Iriki Single dish observations 6

Same as Figure , but from March 2011 to Septermber 2012.

periods are the most essential to present the nature of the variability of RX Boo. At least, we accept the fact that the stellar variability show the double-periodic nature with the shorter period of 160 - 170 d and the longer one of 280 - 350 d. These early studies of periods of RX Boo are tabulated in table 4.3.

The period-luminosity relation is useful not only to estimate the distance of astronomical objects but also to study the stellar structure and pulsation properties. The above obtained M_K and the periods should be compared with the PL-relation of the long-period variables in our Galaxy and the Magellanic Clouds. Glass & van Leeuwen (2007) compared the period and M_K with the Period-Luminosity sequences originally found in the Magellanic Cloud by Wood (2000) and corrected by Ita et al. (2004). The relation for Miras and SRa stars is labeled as sequence C, and that for some of SRb as sequence C$'$. For the long period, RX Boo is found on sequence C, and on sequence C$'$ for the short period. The fact indicates that both two periods of RX Boo look concerned with the basic properties of stellar structure not with any spontaneous occurrence. One of the periods corresponds to a definite mode of pulsation, and the other to another mode. The simultaneous enhancement of both modes may be evidence for the transient nature of RX Boo between the sequence C and C$'$ stars.

4.5 Stellar Properties of RX Bootis

The revision of the parallax will yield the derivation of the revised physical parameters of the star. A thorough survey of late-type giants including RX Boo

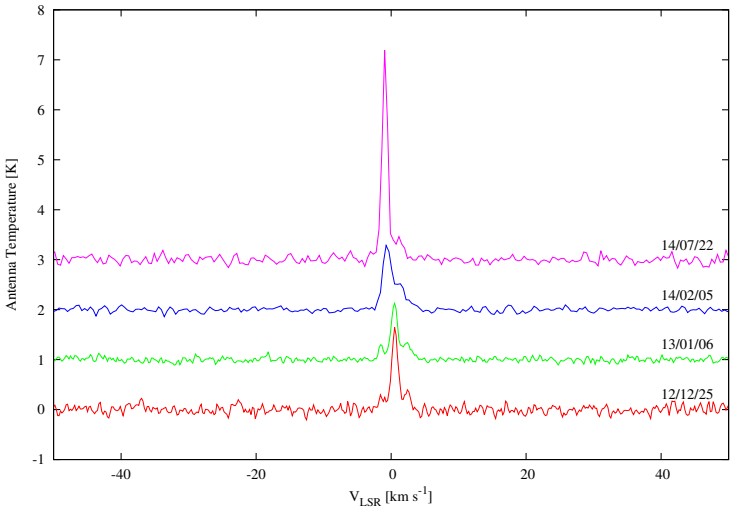

Figure 4.11: The single-dish spectra of RX Boo 7
Same as Figure , but from December 2012 to July 2014.

has been performed by Kučinskas et al. (2005). They discussed the Rosseland radius for a measure of the stellar radius. It is defined as the radius where the optical depth calculated by using the opacities with the Rosseland mean is equal to the unity. The radius is very similar to the radius where the total flux corresponds to that derived from the effective temperature of stellar atmospheres. For RX Boo, Kučinskas et al. (2005) used the angular diameter of the Rosseland radius, 18.87 ± 0.12 mas, based on the results in Perrin et al. (1998). The Rosseland radius of 278 solar radii is obtained by combining their radius and the present parallax. The estimated value of the radius should be increased from this when we adopt the uniform disk angular diameter of 21.0 ± 0.3 mas

Table 4.3: Period of RX Boo

Periods (days)		Reference
Short Group	Long Group	
160.0	302.0	Taylor (1987)
179.1, 164.0	352.0	Andronov & Kudashkina (1988)
162.3	304.7	Mattei et al. (1997)
	340.0	previous version of GCVS
159.6	278.0	Speil (2006)
162.3		GCVS (Samus et al. (2009))

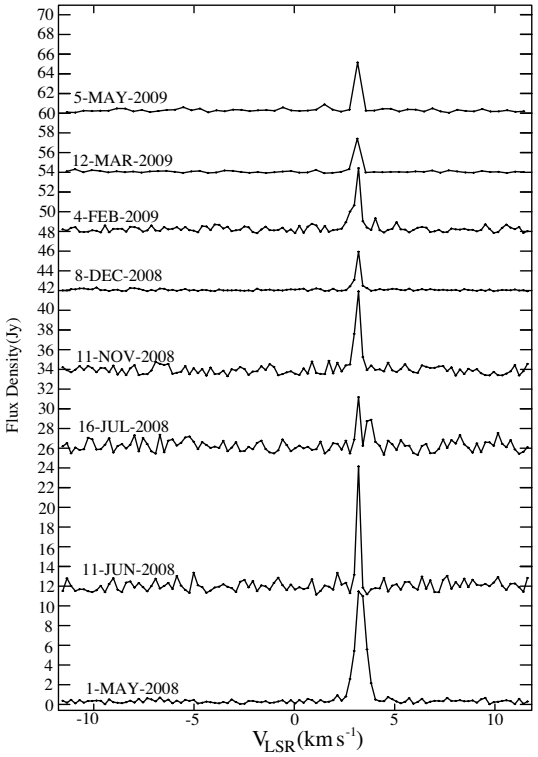

Figure 4.12: The time variation of the cross - power spectra of RX Boo
The time variation of the cross - power spectra of RX Boo obtained by VLBI observations at 22 GHz with VERA. This spectra were obtained from the baseline of Mizusawa – Iriki. We cannot show the spectrum in the 7th epoch on 2009 January 10, because Iriki station did not joined the VLBI observation.

derived by Chagnon et al. (2002).

The stellar radius can be derived with another procedure that is based on the apparent magnitude, the effective temperature of stellar atmosphere, and the parallax. In GCVS, the maximum and minimum V magntude are tabulated as 6.43 and 9.1. We may assume the mean V magnitude of 7.8 from these values. Kučinskas et al. (2005) adopted V of 7.98 in their study. We may assume the mean V magnitude of 8.0 from the AAVSO results between 1987 and 2007 demonstrated in Winnberg et al. (2008). The results presented by AFOEV also show the mean V magnitude of about 8.0. After V magnitude of 8.0 is chosen, the color $(V-K)$ of 9.85 is derived by using K magnitude tabulated in Glass & van Leeuwen (2007). We can obtain the bolometric correction of about -6.5 mag Worthey & Lee (2011), and then we have the apparent bolometric magnitude $m_{\rm BOL}$ of 1.5 mag. Finally, we have $M_{\rm BOL}$ of -4.2 which gives the

stellar luminosity of 3630 $L_\odot$ or $\log(L/L_\odot) = 3.56$. When we use the effective temperature of 2750 K based on Worthey & Lee (2011), the radius of 266 $R_\odot$ is obtained. The effective temperature of such a late M type stars is difficult to estimate from the study of stellar atmospheres. Aringer et al. (1999) have found that the effective temperature of semiregular variables is hotter than Mira stars. This result suggests that the effective temperature of RX Boo will be higher than the mean value for the late-type giants. Such a higher temperature yields smaller radius for this star. Further study on this problem will be interesting. At present, we may suppose the radius of RX Boo of about 270 $R_\odot$ based on the results obtained with two different procedure.

The radius of a pulsating star can be used to estimate the stellar mass when the characteristic period, the pulsation constant, Q is obtained from theoretical consideration. The detailed theoretical study on the radial pulsation of red ginats performed by Xiong & Deng (2007) gives the period ratio and the characteristic period Q for various models. The period ratio of RX Boo is 0.61 for the results of Speil (2006) and 0.53 for those of Mattei et al. (1997). The theoretical ratio of the first overtone period P_{1O} to the fundamental period P_F scatters for less massive and cool models. So it looks difficult to obtain precise results but the period ratio of 0.53 is preferable for the theoretical results. In their theoretical results, the characteristic period for the first overtone mode Q_{1O} does not scatter even for luminous models. We may use Q_{1O} of about 0.039 or $\log Q_{1O} \simeq -1.41$ when we use their algebraic expression, even though the luminosity of RX Boo $\log(L/L_\odot) = 3.56$ exceeds the range of their calculation unfortunately. From the period-density relation,

$$Q_{1O} = P_{1O}\sqrt{M/R^3},$$

we obtain the mass of RX Boo of 1.13 $M_\odot$. The mass estimated here will be increased when we adopt larger radius.

The luminosity and mass of RX Boo can be compared with the theoretical studies of AGB stars. A diagram titled as evolution in mass and luminosity for solar composition stars prepared by G. H. Bowen is presented in Wilson (2000). The diagram shows the rather schematic figure of the evolutionary path on the $\log L$ – $\log M$ diagram. It indicates that first a star of intermediate mass evolves with the increase in the luminosity and almost constant mass, and then the mass decreases with high mass loss rate when the star reaches a critical luminosity. Such a critical mass-luminosity line is called as the cliff in her paper. The luminosity and mass obtained here for RX Boo indicate the star on the locus of evolutionary track for the initial mass of 1 $M_\odot$ and before reaching the cliff. In Wilosn's diagram, the mass loss rate is also indicated, and the rate of 10^{-8} $\dot{M}$ is found for this position. The mass loss rate of 6 - 2 $\times 10^{-7}$ $M_\odot$ yr^{-1} derived by Olofsson et al. (2002) and by Teyssier et al. (2006) does not coincide with the properteis of RX Boo presented above.

Because the derived mass depends on the adequacy of our assumption that Q_{1O} will be constant for cool and bright AGB stars, further examination on the stellar mass should be required.

4.5.1 Water Maser Distribution

Although we used only one maser to obtain the parallax of RX Boo, we detected 74 water masers in total and it is the highest resolution map of RX Boo. These 74 water masers were plotted in Figure 4.16 and shown in table 4.4. The water masers distributed 2 AU × 2 AU, which was smaller than that of typical size (several tens of AU: e.g. Nakagawa et al. 2014, Kamezaki et al. 2014) because water masers was not emitted at the other LSR velocities. We checked the spectra of the observation and the other components did not exist (see Figure 4.12). Winnberg et al. (2008) showed the distribution of 14 AU × 14 AU and we only detected their blue-shifted components (see Figure 4.4), although we cannot detect the other masers. Our red-shifted masers were located in north side and the blue-shifted were located in south side. Since the stellar velocity was +1.0 km s^{-1} based on CO observations (Teyssier et al., 2006), all of our masers, whose LSR velocity ranges are from −3.83 to −2.36 km s^{-1}, are blue-shifted with respect to the star. The red-shifted masers with respect to the star are located east for our masers as shown in Winnberg et al. (2008) or Figure 4.4.

Table 4.4: Parameters of the detected maser spots

ID	$v_{\rm LSR}$	$\Delta\alpha$ [mas]	$\Delta\delta$ [mas]	S [Jy beam^{-1}]	SNR	epoch
1	+2.57	+3.15	+5.39	0.6	6.5	2
2	+2.57	−0.56	+2.30	0.7	8.1	2
3	+2.78	+2.91	+1.53	0.8	6.4	2
4	+2.78	−0.47	+2.26	1.2	9.5	2
5	+2.78	−5.02	+1.11	0.8	6.0	2
6	+2.78	+3.29	+5.07	1.3	10.7	2
7	+2.78	+0.28	+4.99	0.9	7.0	2
8	+2.78	+1.82	+3.03	1.0	8.1	2
9	+2.99	−0.02	+0.10	2.0	11.0	2
10	+2.99	+3.16	+1.22	1.1	6.2	2
11	+2.99	−2.02	+5.89	1.1	6.2	2
12	+2.99	+0.25	+5.00	1.3	6.9	2
13	+2.99	−3.55	+3.32	1.4	7.5	2
14	+2.99	+3.38	+4.80	1.5	8.6	2
15	+2.99	+1.64	+2.66	1.5	8.3	2
16	+3.20	+0.00	+0.00	5.5	23.2	2
17	+3.41	+0.01	−0.09	4.9	23.1	2
18	+3.62	+0.03	−0.20	2.1	17.2	2
19	+3.62	+1.17	+1.84	1.0	8.3	2
20	+3.83	+4.39	+5.61	0.6	6.9	2
21	+3.83	+0.05	−0.28	0.6	6.2	2
22	+2.78	+0.76	+1.59	1.0	7.4	3
23	+2.99	+0.48	+1.45	1.6	8.7	3
24	+2.99	−1.39	+2.02	1.4	7.6	3

Table 4.4: Parameters of the detected maser spots

ID	v_{LSR}	$\Delta\alpha$ [mas]	$\Delta\delta$ [mas]	S [Jy beam^{-1}]	SNR	epoch
25	+2.99	+0.02	−0.07	1.7	9.5	3
26	+2.57	−0.01	+1.57	1.0	6.5	4
27	+2.78	+0.29	+1.38	2.8	17.6	4
28	+3.20	+0.24	+0.48	6.7	13.9	4
29	+4.04	+0.04	−0.14	1.3	9.2	4
30	+2.57	−0.50	+3.48	0.8	7.7	5
31	+2.57	−1.84	+1.25	0.9	8.3	5
32	+2.78	−1.82	+1.16	2.0	13.1	5
33	+2.99	−1.89	+1.23	3.2	15.8	5
34	+2.99	−0.74	+3.42	3.1	15.2	5
35	+3.20	−1.85	+1.58	1.6	10.2	5
36	+3.20	−0.70	+3.48	2.2	13.7	5
37	+3.41	−0.45	−2.71	0.9	7.1	5
38	+3.41	+0.22	+0.37	1.3	9.7	5
39	+3.41	+5.28	+10.95	0.8	6.3	5
40	+3.41	−1.97	−1.18	1.6	12.2	5
41	+3.41	−1.65	+1.72	0.8	6.3	5
42	+3.41	−2.84	−4.04	1.0	7.8	5
43	+3.62	+0.08	+0.57	0.5	6.1	5
44	+3.62	−1.90	−1.09	0.8	9.2	5
45	+2.57	−0.03	−0.02	0.7	9.0	6
46	+2.57	+0.22	+3.78	0.5	6.2	6
47	+2.57	+1.19	+2.25	0.7	8.7	6
48	+2.78	−0.05	+0.09	2.4	18.6	6
49	+2.99	−0.08	+0.43	3.1	20.9	6
50	+2.99	−0.01	+0.03	3.8	25.7	6
51	+3.20	−0.31	−2.43	1.2	8.6	6
52	+3.20	+0.65	+2.21	1.4	9.7	6
53	+3.41	−0.29	−2.62	1.2	11.5	6
54	+3.62	−0.46	−2.82	0.5	7.2	6
55	+3.62	−0.31	−2.43	0.6	8.1	6
56	+2.36	−0.06	+4.03	0.3	6.3	7
57	+2.78	+0.03	−0.09	1.3	16.1	7
58	+3.62	+0.06	−1.87	0.3	6.9	7
59	+2.36	+0.44	+6.89	0.8	12.3	8
60	+2.57	+3.04	+1.57	0.7	7.5	8
61	+2.57	+6.51	−1.83	0.7	7.8	8
62	+2.57	+0.99	+10.07	0.6	6.4	8
63	+2.57	+0.39	+6.91	1.3	14.8	8
64	+2.78	+3.68	+6.43	0.7	7.3	8
65	+2.78	+6.51	−1.66	0.7	7.5	8
66	+2.78	−2.65	+14.21	0.7	7.0	8

Table 4.4: Parameters of the detected maser spots

ID	$v_{\rm LSR}$	$\Delta\alpha$ [mas]	$\Delta\delta$ [mas]	S [Jy beam^{-1}]	SNR	epoch
67	+2.78	+0.38	+6.81	1.4	13.9	8
68	+2.78	−0.05	+0.61	1.7	17.2	8
69	+3.41	−0.00	−0.43	0.9	14.1	8
70	+3.41	+0.67	+2.77	0.8	11.9	8
71	+3.62	+1.81	−3.54	0.5	9.0	8
72	+2.36	+0.79	+6.81	0.5	8.2	9
73	+3.62	+0.64	−1.19	0.3	6.4	9
74	+3.62	+0.18	−0.59	0.3	6.2	9

Column (1) — Spot ID. Column (2) — LSR velocity. Column (3) and (4) — offset positions in R.A. and Dec. relative to the phase tracking center. Column (5) — brightness of the spot. Column (6) — signal to noise ratio. Column (7) — The epoch number coded in Table 2 when Column (2) – (6) were obtained.

4.6 Summary

We have measured annual parallax of the Semiregular variable RX Bootis by tracking a maser spot at $V_{\rm LSR} = 3.2\,{\rm km\,s^{-1}}$ for one year. The annual parallax is 7.31 ± 0.50 mas, corresponding to the distance of 136^{+10}_{-9} pc. The luminosity by using the present parallax is 3630 $L_\odot$ or $\log(L/L_\odot) = 3.56$. With this luminosity and latest periods, RX Boo is found on Sequences C and C$'$ originally discovered on the period-luminosity diagram of the LMC. Based on the present results, we derived the stellar radius of about 270 $R_\odot$. The mass of about 1 $M_\odot$ is estimated from the radius and the theoretical pulsation properties. This mass and the luminosity indicate that RX Boo remains still at the slowly evolving phase based on the reults of stellar evolution consideration. Such an estimate matches the comparatively small mass loss rate of this star. RX Boo seems to be before the phase of strong mass loss.

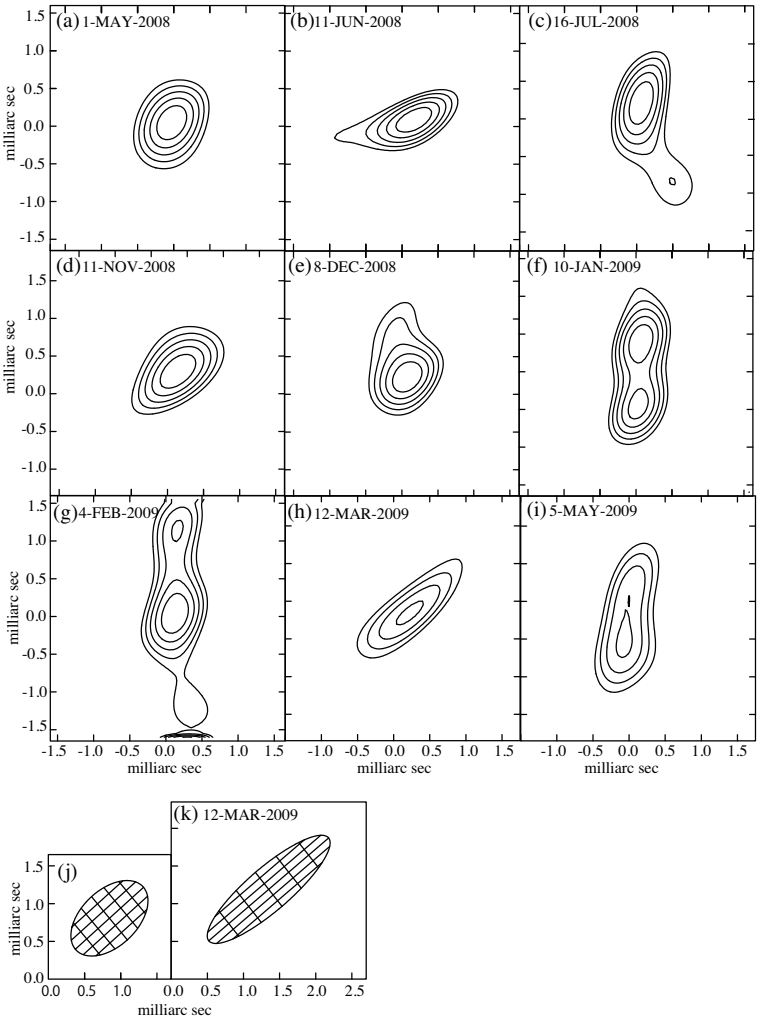

Figure 4.13: Images of the detecte maser spot
(a–i) Contours of masers in each epoch at a channel of $V_{\rm LSR} = 3.2$ km s^{-1}. The center of each map is shown in table 4.1. (j) Synthesized beam in the 8th epoch on 2009 February 4. The shapes of the other epochs except the 9th epoch on 2009 March 12 are almost same. (k) Synthesized beam in the 9th epoch on 2009 March 12.

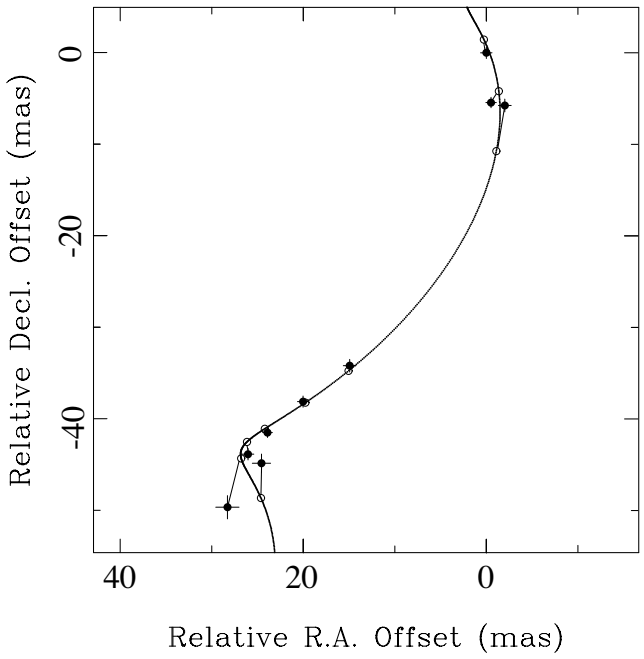

Figure 4.14: Relative position of the maser spot around RX Boo
Relative position of the maser spot around RX Boo with respect to the phase tracking center ((α, δ)=($14^{\rm h}24^{\rm m}11^{\rm s}.6206$, $+25^\circ42'12''.909$)). Filled circles with error bars indicate the observed positions. Open circles indicate the positions calculated from the least square fitting.

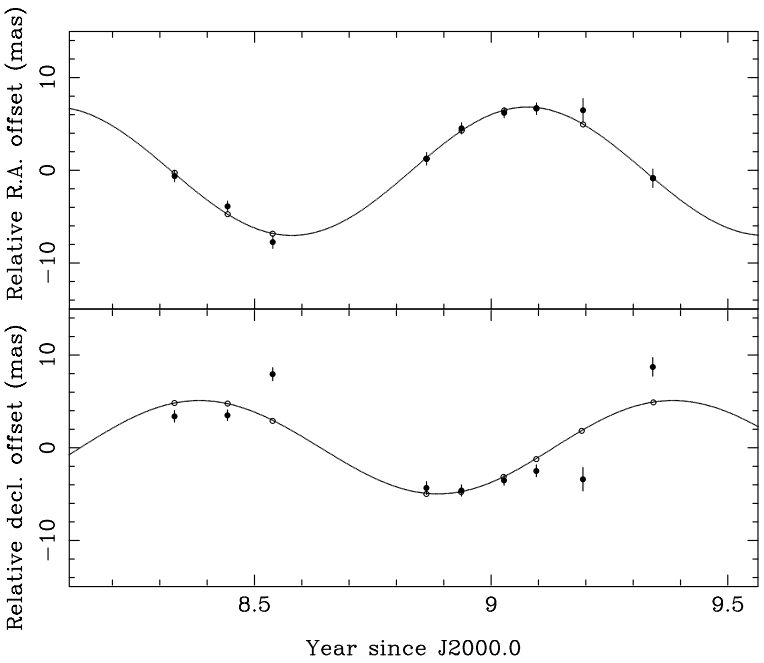

Figure 4.15: Time variation of the position of a maser spot around RX Boo
Time variation of the position of a maser spot around RX Boo in right ascension (top) and declination (bottom) after subtracting the linear proper motion. The solid line is the fitting result of the annual parallax. Filled circles with error bars indicate the observed positions. Open circles indicate the positions calculated from the least square fitting.

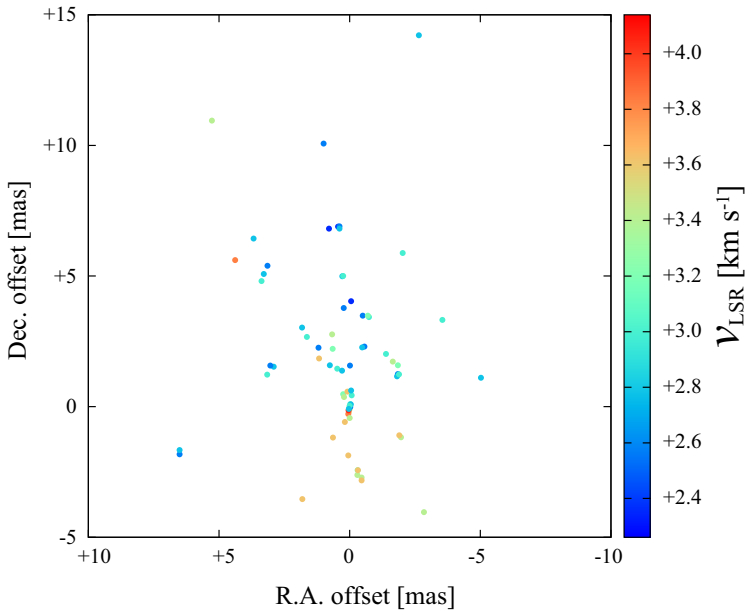

Figure 4.16: Water maser distribution around RX Boo
The distribution of all 74 detected water masers around RX Boo (Colored plots). The color of each spot represents its LSR velocity coded as shown in the color bar. The detected maser positions shown in Table 4.4. The origin is the spot used to measure the parallax ((α, δ)=($14^{\rm h}24^{\rm m}11^{\rm s}.6206$, $+25°42'12''.909$)). The plus symbol is the average position of all detected masers, ($\Delta\alpha$, $\Delta\delta$) = (0.35 mas, 1.87 mas).

5 Distance to a Semi-Regular Variable (SRV) Star, RW Leporis

5.1 Introduction

We showed the four types of Semi-Regular variable (SRV) stars in section 3.1.2 and mentioned the multi-periodic SRV, RX Bootis in section 3. In this section, we showed the parallax measurements to Type-a Semi-Regular (SRa) Variable star, RW Leporis, which has different variable type from RX Bootis and estimated the physical parameters (Luminosity, Radius and Mass).

5.1.1 Type-a Semi-Regular (SRa) Variables

Type-a semi-regular (SRa) variable stars are defined as "Semiregular late-type (M, C, S or Me, Ce, Se) giants displaying persistent periodicity and usually small (< 2.5 mag in V band) light amplitudes. Amplitudes and light-curve shapes generally vary and periods are in the range of 35-1200 days. Many of these stars differ from Miras only by showing smaller light amplitudes." in the General Catalog of Variable Stars (GCVS; Samus et al. 2012). As shown in the definition, the difference from Miras is only one point that they shows smaller light amplitudes. In Mattei et al. (1997), the reason why the threshold of magnitude in V band is 2.5 mag is shown. They made the diagram of the amplitude in V band versus its instability and it is shown in Figure 5.1. They said that this shows the "traditional" amplitude cutoff of Mira. Certainly, we can see the division of Mira and SRVs near the amplitude of 2.5 mag.

5.1.2 RW Leporis

RW Leporis (RW Lep) is a SRa variable star, which has persistent periodicities and small variation amplitudes (< 2.5 mag in V band). RW Lep is reported to have two different periods of variation. The shorter period of 149.9 days was reported by Goetz (1952) and the longer period of 272 days was reported by Price et al. (2010). Although the parallax of RW Lep was listed in Tycho catalog, it was -64.00 ± 39.00 mas (ESA, 1997). The proper motion listed in Tycho catalog was $(\mu_\alpha \cos\delta,\ \mu_\delta)$=$(15.4 \pm 1.8\ \mathrm{mas\,yr^{-1}},\ -29.6 \pm 1.7\ \mathrm{mas\,yr^{-1}})$. Roeser et al. (2010) reported it to be $(\mu_\alpha \cos\delta, \mu_\delta) = (15.8 \pm 2.1\ \mathrm{mas\,yr^{-1}},\ -31.2 \pm 2.1\ \mathrm{mas\,yr^{-1}})$ in their catalog, named Positions and Proper Motions eXtended-L (PPMXL), which is based on USNO-B1.0 and Two Micron All Sky Survey (2MASS) data. Maser emissions in RW Lep has been reported many times in the literature (Wilson & Barrett, 1972; Crocker & Hagen, 1983; Cesaroni et al., 1988; Haikala et al., 1994; Takaba et al., 1994; Lewis et al., 1995; González Delgado et al., 2003; Shintani et al., 2008; Kim et al., 2013). According to these papers, OH masers were not detected at all, but water masers were detected in every observation. The mass-loss rate and the expansion velocity of RW Lep were investigated using the circumstellar CO emission (Olofsson et al.,

2002). In their results, the mass-loss rate and the expansion velocity of RW Lep are $0.5 \times 10^{-7} M_{\odot}$ yr^{-1} and 4.4 km s^{-1}, respectively.

5.2 Single-dish results

We show the all spectra in Figure 5.2 to 5.5. Although the VLBI observations were conducted from December 2009 to December 2011, water maser emissions were weak in this period and water maser emission became too weak for us to detect after that time. However, we could detect the water maser emissions with VLBI as mentioned below. As we can see the spectra, there are mainly two components (see Fig. 5.6) and some water maser burst, which occurred every component. The water maser emissions were seen from -65 km s^{-1} to -56 km s^{-1}. We showed the light curves of the water maser components in Figure 5.7, with a constrain of signal-to-noise ratio more than 3 in their integrated intensities . Component 1 is bluer than component 2 as shown in Figure 5.6 and there are no correlations between their integrated intensities. However, the total integrated intensity seems to vary with the peak-to-peak period of 180 day and 268 day. These periods were obtained from a small dataset and have large uncertainty since we did not fit the data. These periods were almost consistent with previously obtained optical periods, which is 149.9 day and 272 day (Goetz , 1952; Price et al., 2010). The shorter period was obtained from the deference between the peak of component 1 and 2. We can also confirm that the total integrated intensity gradually reduced, as seen in Figure 5.7.

5.3 Annual Parallax

To measure the annual parallax, we used two maser spots which were detected in more than two continuous epochs, and which have signal-to-noise ratios larger than 5 in the phase-referenced images. These spots had different radial velocities of $v_{\rm LSR} = -60.1$ km s^{-1} and -63.0 km s^{-1}, respectively. We did not detected both of them in the same epoch.

In order to obtain the annual parallax, we adopted an assumption that each maser spot moves with a constant velocity and the reference source is fixed on the sky. We performed a least square fitting by using the following equations for each spot;

$$\Delta\alpha^{(i)} \cos\delta = \varpi(-\sin\alpha\cos\lambda_{\odot} + \cos\epsilon\cos\alpha\sin\lambda_{\odot}) + (\mu_{\alpha}^{(i)}\cos\delta)t + \alpha_0^{(i)}\cos\delta \tag{5.1}$$

$$\Delta\delta^{(i)} = \varpi(\sin\epsilon\cos\delta\sin\lambda_{\odot} - \cos\alpha\sin\delta\cos\lambda_{\odot} - \cos\epsilon\sin\alpha\sin\delta\sin\lambda_{\odot}) + \mu_{\delta}^{(i)}t + \delta_0^{(i)}, \tag{5.2}$$

where i denotes each observation epoch, $(\Delta\alpha^{(i)}\cos\delta, \Delta\delta^{(i)})$ are the displacements of the maser spot, $(\mu_{\alpha}^{(i)}\cos\delta, \mu_{\delta}^{(i)})$ is the linear motion of the maser spot, t is time, ϖ is the annual parallax, (α, δ) are the right ascension and declination of the source, $\lambda_{\odot}$ is the ecliptic longitude of the Sun, ϵ is the obliquity of the ecliptic, and $(\alpha_0^{(i)}, \delta_0^{(i)})$ are the coordinates of the maser spots at $t = 0$. In this fitting, we derived five parameters; $\varpi, \mu_{\alpha}\cos\delta$, μ_{δ}, α_0 and δ_0, while the

total number of data to fit is eighteen (right ascension and declination at nine epochs). Since in nine of eighteen epochs, we did not detect any maser spot due to bad weather or the time variation of maser emission, we used nine epochs for the fitting.

In this fitting, the positions of two maser spots relative to reference source, J0539−1550, were fitted simultaneously with one common parallax, but different proper motions and position offsets for individual spots. This reduces χ^2 per degree of freedom in the parallax fit. The errors were 0.10 mas and 0.23 mas in right ascension and declination, respectively as was required to produce a value of $\chi^2 = 1$. Weightings of the data in the fitting are based on the position errors.

In Figure 5.3, we show the changes of observed positions of masers on the celestial sphere with respect to the phase tracking center, and the results of the fitting of proper motions and parallax. In Figure 5.9, we present the parallactic motions of two maser spots at $v_{\rm LSR} = -60.1$ km s^{-1} (open circles) and -63.0 km s^{-1} (filled circles) in right ascension and declination. The apparent motion clearly exhibits an annual parallactic motion. From our fitting procedures, we obtained an annual parallax of 1.62 ± 0.16 mas, corresponding to a distance of 617^{+68}_{-55} pc. Although RW Lep was observed by the HIgh Precision PARallax COllecting Satellite (HIPPARCOS), it is only listed in the Tycho catalogue (ESA, 1997). The ESA online catalog gave -64.00 ± 39.00 mas for the parallax of RW Lep, but the negative value is, of course, unreal. Before the work shown in this paper, this result listed in Tycho catalog was the only reported value; ours is the first legitimate measurement of the parallax of RW Lep. We measured the proper motion of RW Lep to be $(\mu_\alpha \cos\delta,\ \mu_\delta)$=$(5.53 \pm 0.98$ mas yr^{-1}, -26.30 ± 1.43 mas yr$^{-1})$ for the spot at $v_{\rm LSR} = -60.1$ km s^{-1} and $(\mu_\alpha \cos\delta,\ \mu_\delta)$=$(12.55 \pm 0.59$ mas yr^{-1}, -26.92 ± 0.68 mas yr$^{-1})$ for the spot at $v_{\rm LSR} = -63.0$ km s^{-1}. We discuss the maser proper motions and distributions in further detail in section 4.7.

5.4 RW Leporis the PL plane

Since we derived the distance to RW Lep from its annual parallax, we can plot RW Lep on the PL plane. Before showing the plot we review the three required parameters to plot; the distance, the apparent magnitude in K band m_K and the pulsation period of the star.

We measured the distance of RW Lep to be 617^{+68}_{-55} pc as shown in the previous section. The apparent K magnitude is $m_{K_s} = +0.639 \pm 0.319$ mag according to the 2MASS point source catalog (Cutri et al., 2003). Price et al. (2010) published near infrared stellar light curves for 3.6 years observed as part of the Diffuse Infrared Background Experiment (DIRBE) program by the Cosmic Background Explorer (COBE). They showed that the flux of RW Lep in K band was 340 Jy and the amplitude was 30 Jy. We adopted the amplitude as the error because the star varies and moves on the PL plane within the range of the amplitude. The flux corresponds to an apparent K magnitude of $m_K = +0.687^{+0.100}_{-0.092}$ mag and to 2MASS K_s magnitude of $m_{K_s} = +0.588^{+0.102}_{-0.093}$

mag. Then, we used the conversion equation between K_{DIRBE} and K_{2MASS}, $K_{DIRBE} = 0.982K_{2MASS} + 0.109$ shown in Smith et al. (2004). These two apparent magnitudes coincide within their errors. In this paper, we used the apparent magnitude by Price et al. (2010), because their magnitude takes into account the variability. From these values, we obtained the absolute K magnitude of RW Lep to be M_K=$-8.27^{+0.30}_{-0.33}$ mag. We estimated the period of RW Lep from GCVS (Samus et al. 2012) and Price et al. (2010). According to GCVS, the period of RW Lep was posted as 149.9 days based on Goetz (1952) and Goetz (1952) did not show the light curve. On the other hand, Price et al. (2010) showed the period was 272 days from their data and the light curve. We use both for these periods of RW Lep because a SRV star may have multi-periods, but the period shown in Price et al. (2010) is more reliable since they showed the light curve. We cannot determine whether RW Lep pulsates with two periods at the same time or not, since these two measurements are separated by about 50 years. During these 50 years, RW Lep may have switched its pulsation mode as Bedding et al. (1998) reported for a SRV, R Dor. This change may be due to a physical or chemical change.

Using these values we plot RW Lep in the PL plane (Fig. 5.10). The plot of the PL plane is useful to study the properties of a pulsating star. We compared RW Lep with long-period variables in the LMC on the PL plane. If we take the longer period reported by Price et al. (2010), RW Lep was located between the sequences C and C′. The sequence C is composed of Mira type and part of the SRa type variable stars (Cioni et al., 2001). The sequence C′ is composed of many SRVs pulsating with overtone mode. Although RW Lep is classified as SRa (Samus et al., 2012), its location on the PL plane is plausible, since some of Mira and SRVs are located between the sequences C and C′. It is, therefore, difficult to say whether RW Lep pulsates with a fundamental mode or an overtone mode. If we use the shorter period based on the observations by Goetz (1952), RW Lep lies at the sequence B^+. Ita et al. (2004) says that the sequence B^+ is composed of "Less regularly pulsating AGB variables", but the pulsating mode is not clear. In any cases, we cannot determine the pulsation mode of RW Lep.

5.5 Stellar Properties of RW Leporis

Using the estimated distance, we can discuss the basic stellar properties of RW Lep. Here, we first obtain the radius of RW Lep. We calculated the K-band bolometric correction of +3.06 mag based on the equation shown in section 6.4 of Whitelock et al. (2000), 2MASS J-band magnitude of +2.001 mag and DIRBE K-band magnitude of +0.687 mag. We estimated the effective temperature of 3110 K from the equation (8) and (9) in Takeuti et al. (2013), 2MASS H-band magnitude of +1.086 mag and DIRBE K-band magnitude of +0.687 mag. The bolometric correction allowed calculation of the apparent bolometric magnitude of RW Lep, $m_{bol} = +3.75$ mag. This corresponds to $M_{bol} = -5.73$ mag or 15400 $L_\odot$. Using the effective temperature, we estimate the radius of RW Lep to be 428 $R_\odot$. The radius has the ranges of $\sim \pm 100 R_\odot$ or $\sim 20\%$ since evolved

Table 5.1: Evolved stars with precise VLBI parallaxes from the literature

Name	Variable type	Parallax [mas]	Apparent magnitude m_K[mag]	Period [days]	References
U Her	Mira	3.76±0.27	−0.30	406.4	V07, W08
S CrB	Mira	2.39±0.17	+0.32	359.7	V07, W08
S Crt	SRb	2.33±0.13	+0.79	155	N08, GCVS*, C03
SY Scl	Mira	0.75±0.03	+2.54	415	N11, W94
RX Boo	SRb	7.31±0.50	−1.85	159.6 & 278.0	K12, G07, S06
R Aqr	Mira	4.59±0.24	−1.02	387	M14, W08
T Lep	Mira	3.06±0.04	+0.09	368	N14, W08

*General Catalogue of Variable Stars
References:V07 – Vlemmings & van Langevelde (2007); W08 – Whitelock et al. (2008);
N08 – Nakagawa et al. (2008); C03 – Cutri et al. (2003); N11 – Nyu et al. (2011);
W94 – Whitelock et al. (1994); K12 – Kamezaki et al. (2012);
G07 – Glass & van Leeuwen (2007);S06 – Speil (2006);M14 – Min et al. (2014);
N14 – Nakagawa et al. (2014)

stars are pulsating with variation of about 100 solar radius in their pulsation phases (e.g. Thomson et al. 2002).

Using the derived radius we can estimate the mass of RW Lep using the pulsation constant. The pulsation constant (e.g., Binney & Merrifield 1998) is given as

$$Q_i = P_i \sqrt{M_i / R^3}, \tag{5.3}$$

where i indicates ith overtone mode, and 0 and 1 indicate fundamental mode and first overtone mode, respectively. P_i is the pulsation period in days, M is the mass in $M_\odot$, and R is the radius of the star in $R_\odot$. We adopted the pulsation constant $Q_0 = 0.062$ or $\log Q_0 = -1.21$ for fundamental mode, and $Q_1 = 0.039$ or $\log Q_1 = -1.41$ for first overtone mode, which are derived from the effective temperature and Figure 4a shown in Xiong & Deng (2007). We use $P_0 = 272$ day and $P_1 = 149.9$ day, although we cannot determine the pulsation mode for each observed period. With $R = 428\,R_\odot$, we obtain the mass of RW Lep to be $M_0 \simeq 4.1\,M_\odot$ or $M_1 \simeq 5.3\ M_\odot$. The two masses estimates are consistent because these value may change by a factor. We conclude that the mass of RW Lep is $M \simeq 4.7 M_\odot$ as the average of our two estimates. We need a more precise model of pulsating stars and a more reliable period to estimate the mass of RW Lep at any higher precision.

5.6 Water Maser distributions

In the previous section we used only two maser spots, at $v_{\rm LSR} = -60.1$ km s^{-1} and -63.0 km s^{-1}, to measure the annual parallax because only these spots were detected at three or more continuous epochs. We detected some maser

spots at $v_{\rm LSR} \simeq -58.0$ km s^{-1}, although these spots were not persistent enough to be used in the parallax fitting. We show the distribution of all detected water maser spots in Figure 5.11 and their parameters are shown in Table 5.2. Before this work, water masers had been detected at $v_{\rm LSR} = -59.2$ km s^{-1} and -57.8 km s^{-1} (Crocker & Hagen, 1983), -60.2 km s^{-1} (Takaba et al., 1994) and $-63.6 < v_{\rm LSR} < -64.5$ km s^{-1} and $-58.6 < v_{\rm LSR} < -59.1$ km s^{-1} (Shintani et al., 2008). The velocity range of our results are consistent with all these previous results. Kim et al. (2013) reported the LSR velocity of SiO masers in RW Lep at ~ -58.7 km s^{-1}. The LSR velocity of RW Lep should be close to that of SiO masers since the SiO maser is located near the central star both in space and in velocity. If we assume the stellar LSR velocity of RW Lep to be -58.7 km s^{-1}, water maser spots at -60.1 km s^{-1} and -63.0 km s^{-1} are blue-shifted and the spots at -58.0 km s^{-1} are red-shifted.

There exists some previous works on the stellar proper motion of RW Lep (Roeser et al., 2010; Zacharias et al., 2005; Høg et al., 2000). Their values are consistent with each other within the errors. We take the proper motion $(\mu_\alpha \cos\delta, \mu_\delta) = (+15.8 \pm 2.1\ {\rm mas\,yr^{-1}}, -31.2 \pm 2.1\ {\rm mas\,yr^{-1}})$ reported by Roeser et al. (2010). In this case, the maser spots at $v_{\rm LSR} = -60.1$ and -63.0 km s^{-1} show motions of $(\Delta\mu_\alpha \cos\delta,\ \Delta\mu_\delta) = (-10.27\ {\rm mas\,yr^{-1}},\ +4.9\ {\rm mas\,yr^{-1}})$ and $(-3.25\ {\rm mas\,yr^{-1}},\ +4.28\ {\rm mas\,yr^{-1}})$ relative to the star, respectively.

Using the relative motion vectors and the positions on the sky of these two maser spots, we can estimate the kinematical center as the crossing point of the maser trajectories. The derived kinematic center is $(\Delta\alpha, \Delta\delta) = (+29.6$ mas, -31.3 mas) relative to the phase tracking center, which is shown as a black plus symbol in Figure 5.11. We note that the position is located between the blue and red shifted components on the sky. The central star of RW Lep should be located at this kinematical center. If it is, the water maser spots are distributed at ~ 22 AU from the star, this is ~ 11 times larger than the stellar radius ($428\,R_\odot$ or 1.99 AU). This value is consistent with that of T Lep, where water maser spots are distributed about 14 times larger than the stellar radius (Nakagawa et al., 2014). If it were possible to detect more maser spots over a longer time range, we would be able to trace the detailed kinetics in the vicinity of the star, which may reveal an expanding shell and/or bipolar outflow.

5.7 Summary

We have measured the annual parallax of the water masers around the semi-regular variable star RW Lep using observations with VERA. We measured a parallax of 1.62 ± 0.16 mas, corresponding to a distance of 617^{+68}_{-55} pc. This is the first successful estimation of the parallax of RW Lep, since the parallax listed in Tycho catalog was a negative value. RW Lep is located between the sequences C and C$'$ in the PL plane, if its pulsating period is 272 days. It is located on the sequence B$^+$ in the PL plane, if its pulsating period is 149.9 days. We estimated the luminosity, radius and mass of RW Lep to be 15400 $L_\odot$, 428 $R_\odot$ and 4.7 $M_\odot$, respectively. Using the motions and positions of the maser spots, we estimated the position of the star on the sky. All detected maser spots are located at 22

Table 5.2: Parameters of the detected maser spots

ID	$v_{\rm LSR}$	$\Delta\alpha$ [mas]	$\Delta\delta$ [mas]	S [Jy beam^{-1}]	SNR	$\mu_\alpha \cos\delta$ [mas yr^{-1}]	μ_δ [mas yr^{-1}]	epoch
1	−63.6	+24.07	−13.97	0.9	14.7	...	...	11
2	−63.8	+24.13	−14.13	0.4	7.6	...	...	11
3	−58.0	−8.79	−36.30	0.4	6.3	...	...	11
4	−58.0	−5.03	−48.57	0.3	5.3	...	...	11
5	−58.0	−4.62	−69.32	0.4	6.5	...	...	11
6	−57.8	−7.59	−32.72	0.4	6.5	...	...	11
7	−58.2	−4.45	−69.40	0.4	6.6	...	...	11
8	−63.0	+4.68	+1.59	1.9	22.8	$+12.55 \pm 0.59$	-26.92 ± 0.68	11
9	−63.2	+4.73	+1.50	1.0	12.8	...	...	11
10	−63.4	+24.02	−13.80	1.1	16.7	...	...	11
11	−62.8	+4.70	+1.61	1.5	19.9	...	...	11
12	−62.6	+4.69	+1.75	0.6	10.5	...	...	11
13	−60.1	−2.80	−15.81	2.8	21.1	$+5.53 \pm 0.98$	-26.30 ± 1.43	1

Column (1) — Spot ID. Column (2) — LSR velocity. Column (3) and (4) — offset positions in R.A. and Dec. relative to the phase tracking center. Column (5) — brightness of the spot. Column (6) — signal to noise ratio. Column (7) and (8) — best fit linear motion in R.A. and Dec with the error. Column (9) — The epoch number coded in Table 5.1 for which Column (2) – (6) were obtained.

AU or 11 stellar radii from the star.

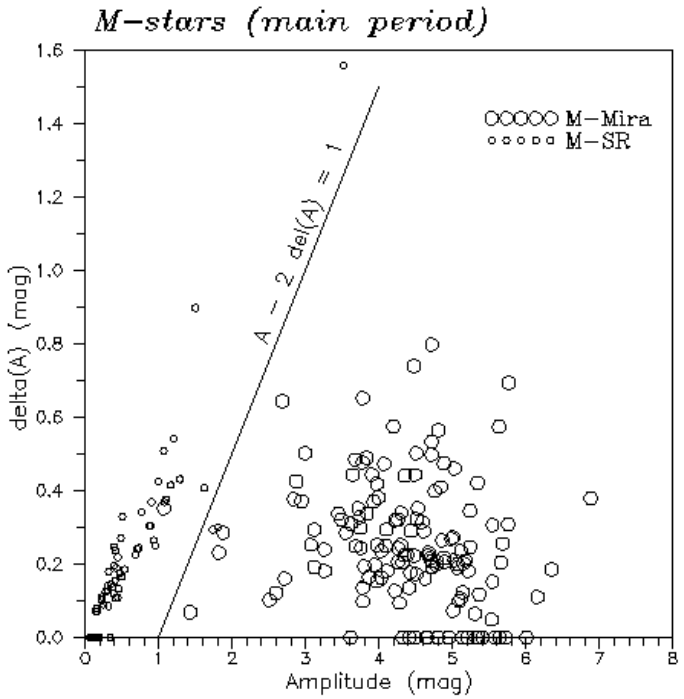

Figure 5.1: The diagram of the amplitude in V band versus its instability δA

The diagram of the amplitude in V band versus its instability δA shown in Mattei et al. (1997). We can see the "traditional" amplitude cutoff of Mira which is the amplitude of 2.5 mag in V band. In this figure, the "M" of "M" – Mira and "M" – SR indicates the Spectral type of the stars, separates from the Carbon rich stars (they are often called as C-Mira or C-SR) and shows that they are Oxygen rich stars. The "main period" in the figure title shows that secondary or more period of multi-periodic stars are not shown in the diagram, which both Mira and SRVs have.

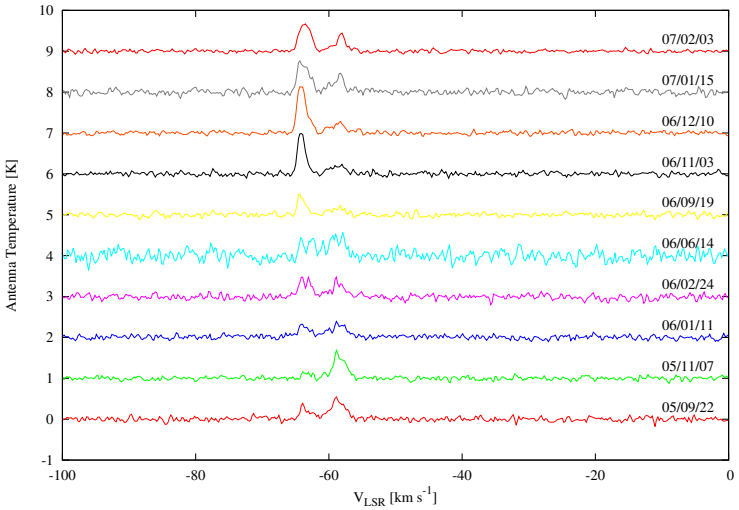

Figure 5.2: Water maser spetra of RW Lep obtained with VERA Iriki Single dish observations 1

The single-dish spectra of RW Lep observed from September 2005 to February 2007 with VERA Iriki telescope. We showed the observed date in right of the spectra.

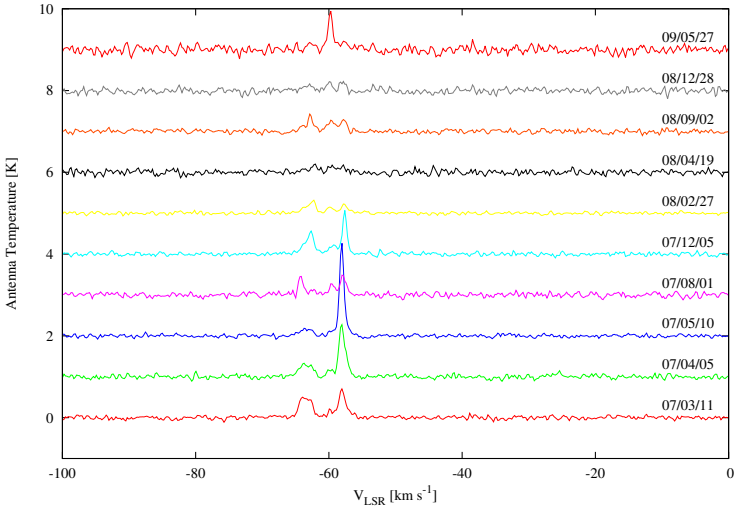

Figure 5.3: Water maser spetra of RW Lep obtained with VERA Iriki Single dish observations 2

Same as Figure 5.2, but from March 2007 to May 2009.

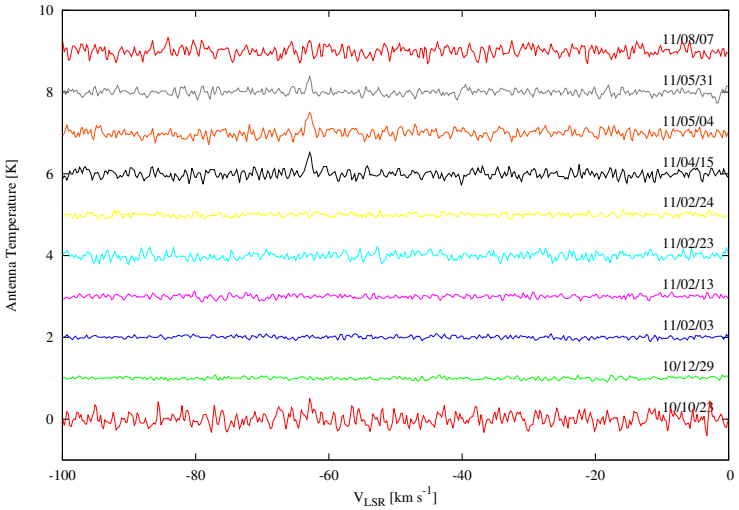

Figure 5.4: Water maser spetra of RW Lep obtained with VERA Iriki Single dish observations 3

Same as Figure 5.2, but from October 2010 to August 2011.

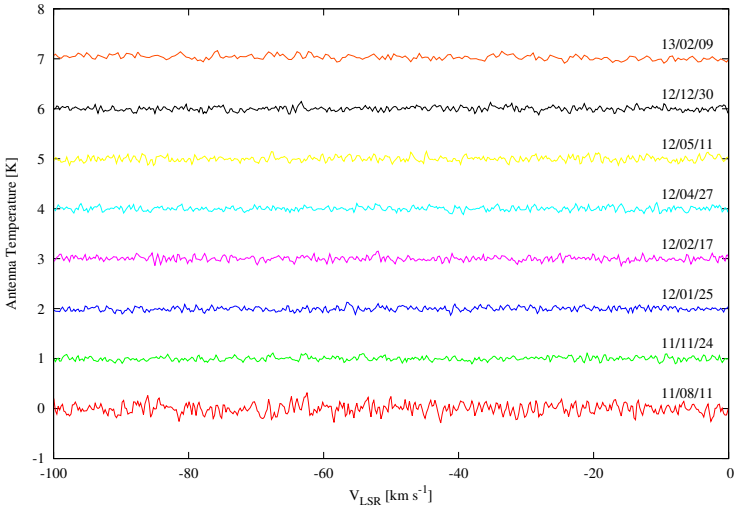

Figure 5.5: Water maser spetra of RW Lep obtained with VERA Iriki Single dish observations 4

Same as Figure 5.2, but from August 2011 to February 2013.

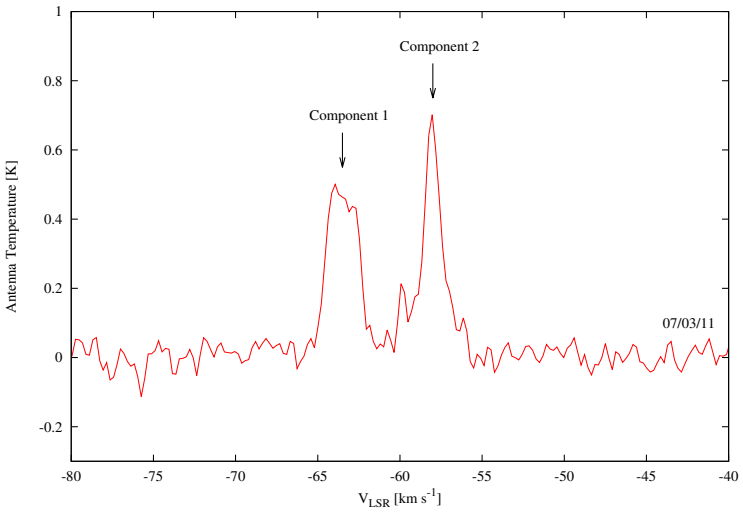

Figure 5.6: The single-dish spectrum of RW Lep at March 11 2007
The single-dish spectrum at March 11 2007, which was obtained with VERA Iriki telescope. The arrows show two distinct components.

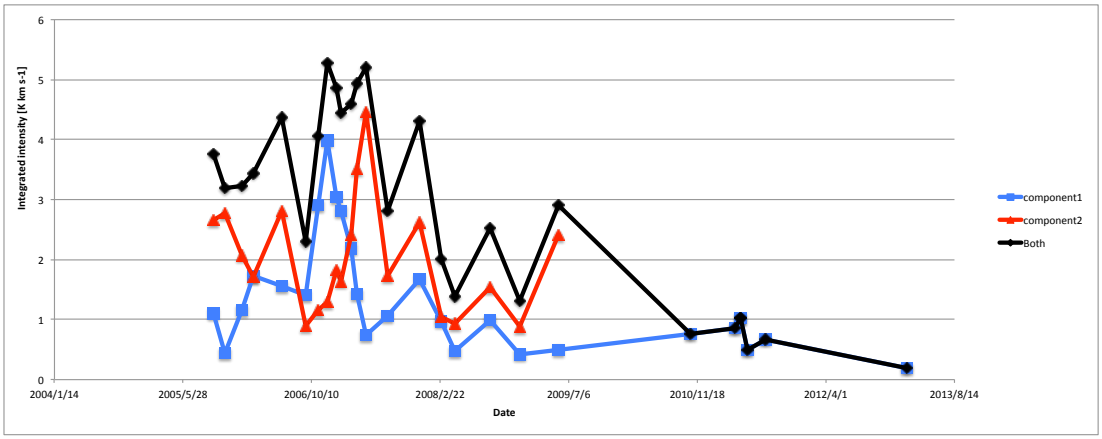

Figure 5.7: Light curves of the integrated intensity of RW Lep
The light curves of the integrated intensity of water masers around RW-Lep, which is produced from the Iriki Single-dish spectra. We produced the plots with the data points whose signal-to-noise ratios are higher than 3 in their integrated intensities. The blue squares with line, the red triangles with line and the black diamonds with line show the integrated intensity of component 1, component2 and both of them, respectively. Each range of them is from -65 km s^{-1} to -62 km s^{-1}, from -62 km s^{-1} to -56 km s^{-1} and from -65 km s^{-1} to -56 km s^{-1}, respectively.

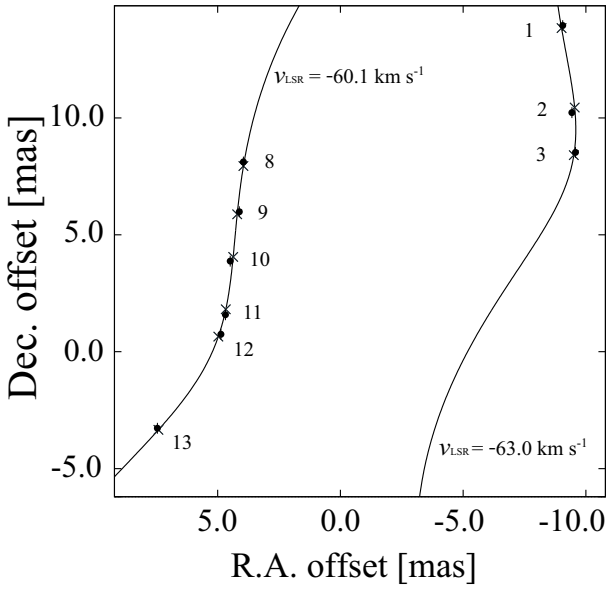

Figure 5.8: Relative positions of the maser spots around RW Lep to the phase tracking center

Relative positions of the maser spots around RW Lep with respect to the phase tracking center, (α, δ)=($05^{\rm h}38^{\rm m}52^{\rm s}.726$, $-14°02'27''.18$). Filled circles with error bars (0.10 mas for Right Ascension and 0.23 mas for declination) denote the observed positions. Gray crosses denote the positions calculated from the least square fitting. Solid curves denote the fitting results. The number near each spot indicates the epoch number label shown in Table 3.3. The LSR velocity of the spot is shown near the curve.

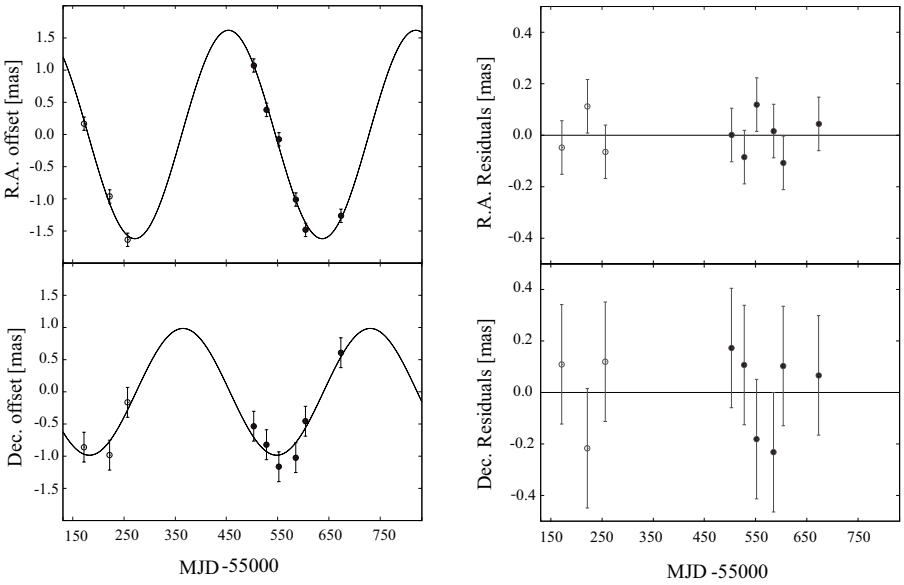

Figure 5.9: Time variations and the resuduals of the position of the maser spots of RW Lep
Left) Time variation of the position of the maser spots around RW Lep in right ascension (top) and declination (bottom) with the linear proper motion subtracted. The filled and open circles with error bars show the observed positions of maser spots at $v_{\rm LSR} = -60.1$ km s^{-1} and -63.0 km s^{-1}, respectively. The solid curves represent the fitting results. Right) Residuals from the fitting results of each epoch in right ascension (top) and declination (bottom). The circles and error bars indicate the same as the left plot.

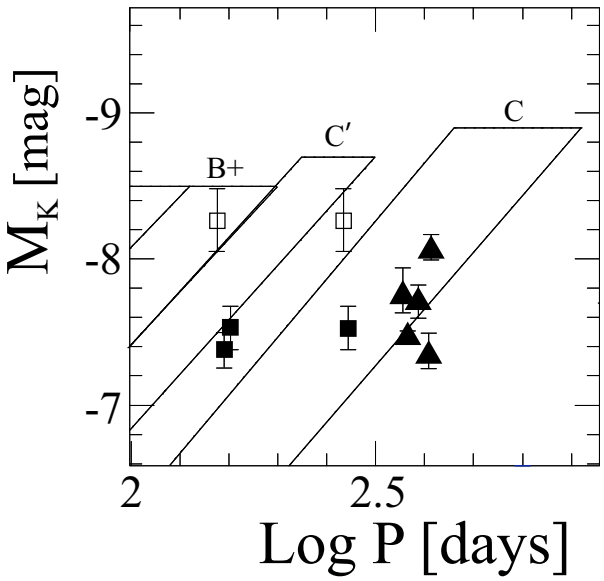

Figure 5.10: Period-luminosity diagram of RW Lep and 7 previously observed SRVs and Miras in the MWG
The period-luminosity diagram of RW Lep and 7 previously observed SRVs and Miras in the MWG overlaid on sequences reproduced from Ita et al. (2004). RW Lep are shown with open squares. Two symbols correspond to two different periods reported by GCVS and Price et al. (2010). The filled squares and triangles show SRVs and Miras, respectively. All have VLBI parallaxes with precisions better than 10% and their periods and K band apparent magnitudes are shown in Table 5.1.

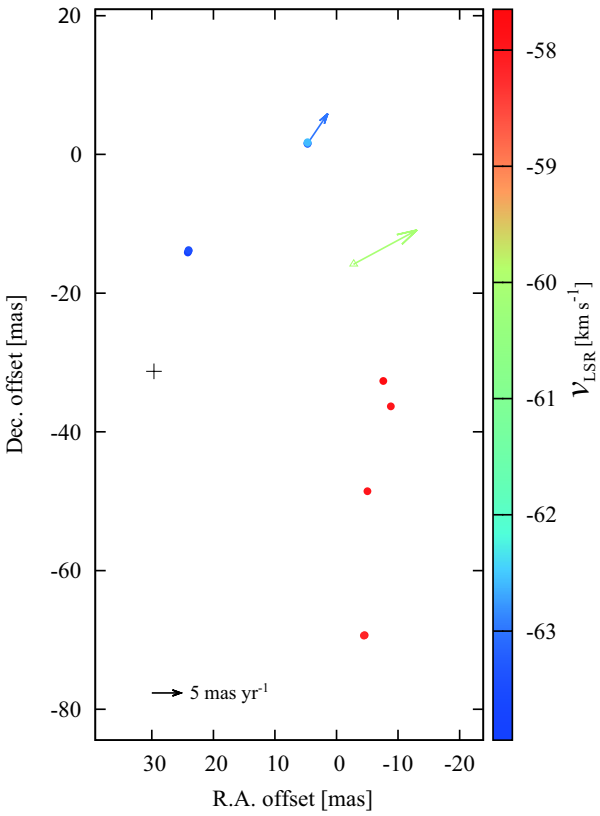

Figure 5.11: Distribution of all detected water maser spots in epoch 11
The distribution of all detected water maser spots in epoch 11 (Colored filled circles and open triangle). The color of each spot represents its radial velocity coded as shown in the color bar. The filled circles are the masers detected in this epoch. The open triangle is the predicted position of the maser spot at $v_{\rm LSR} = -60.1$ km s^{-1} using the proper motion and the elapsed days from the epoch 1. Note that this spot was not detected in epoch 11. The arrows show the maser motions relative to the star (Roeser et al., 2010). The black plus symbol shows the kinematic center estimated using the position and proper motion vectors of the maser spots. The map origin is the tracking center of RW Lep, (α, δ)=($05^{\rm h}38^{\rm m}52^{\rm s}.726$, $-14°02'27''.18$).

6 Discovery of a New X-ray-emitting Class 0 Candidate in the NGC2264 Star Forming Region

6.1 Introduction

For the star forming regions, it is very important to know their distances, since their masses, luminosities, densities, actual sizes are estimated from the distances. We selected NGC2264 star forming region as a target because this region has the distances estimated from various methods (photmetric, kinetic, and so on), it is best site to investigate the early star formation since many stars are being born now and it is active star forming site. Of them all, there are many results of the photometric distances since NGC2264 is known with small interstellar extinction ($\lesssim 1.0$ mag, Dahm (2008)). This is a good situation for us to compare our annual parallactic distance with other distances. Some other star forming regions have different distance between annual parallactic and the other (e.g. Hirota et al. (2008); Kurayama et al. (2011)). Certainly, these distances are sometimes consistent. Which pattern is for NGC2264 ?

To know the formed stellar properties (e.g. luminosity, mass and density), we need the accurate distance. After we obtained the accurate distance, we can discuss them. We used water masers to determine the distance to NGC2264, and water masers are considered to be associated with the class 0/I young star Furuya et al. (2001, 2003). Therefore, investigating the stellar properties of the driving source of water masers is very useful to discuss and to know the early star formation. Thus, we discussed the type of the driving source and its young stellar class based on our distance estimation.

6.1.1 What is Class 0 Source ?

Lada & Wilking (1984) classified infrared point sources based on the spectral energy distributions (SED) with their infrared observations. Lada (1987) divided them into three classes (I – III) (see Figure 6.1) and these classes are often used as a classification to characterize their evolutionary stages until now. As a method to classify these classes, the spectral index (α) is often used (e.g. Andre & Montmerle (1994); Greene et al. (1994); O'Linger et al. (2006)) and is defined as

$$\alpha = \frac{\mathrm{dlog}(\lambda \mathrm{F}_\lambda)}{\mathrm{dlog}\lambda} \tag{6.1}$$

where the slope is often between near-infrared (almost 2 μ m) and mid-infrared (from 10 to 25 μ m). O'Linger et al. (2006) is summarized the scheme of Greene et al. (1994) as the following: Class I sources have positive spectral indices ($\alpha > 0.3$) because of their infrared excess from their circum-stellar disks and envelopes. Class II and Class III sources have negative spectral indices, $-1.6 < \alpha < -0.3$ and $\alpha < -1.6$, respectively. The spectral index of $-0.3 < \alpha < 0.3$ is called as "flat spectrum" have near-infrared spectra that are strongly veiled by

continuum emission from hot circumstellar dust. They have infrared excesses compared to that expected from their black body of the central star and they are caused from their circum-stellar disks. Although this method is used now, Enoch et al. (2009) suggested the method using the bolometric temperature (T_{bol}) previously proposed by Myers & Ladd (1993) and Chen et al. (1995) based on their comparisons and observations toward perseus, serpens and ophiuchus region. According to Myers & Ladd (1993) and Chen et al. (1995), Class 0, I and II sources have $T_{\rm bol}$70 K, 70 K $< T_{\rm bol} <$ 650 K, 650 K $< T_{\rm bol} <$ 2800 K, respectively (but Class I sources need 1.1 mm detections). Class 0 sources were defined with far-infrared or (sub) milli-meter wavelength and non-detections in shorter wavelength than mid-infrared. The schematic images and SEDs of these classes are shown in Figure 6.1.

Although these classifications are based on their infrared spectra, Andre et al. (2000) is summarized the properties of Class 0 sources based on mainly radio wavelength observations as follows:

1. Indirect evidence for a central YSO, as indicated by, e.g., the detection of a compact centimeter radio continuum source, a collimated CO outflow, or an internal heating source.

2. Centrally peaked but extended submilli-meter continuum emission tracing the presence of a spheroidal circumstellar dust envelope (as opposed to just a disk).

3. High ratio of submilli-meter to bolometric luminosity suggesting the envelope mass exceeds the central stellar mass: $L_{smm}/L_{bol} > 0.5\%$, where Lsmm is measured longward of 350 μm. In practice, this often means a SED resembling a single temperature blackbody at T $\sim$ 15 – 30 K.

The property 1, 2 and 3 distinguishes to pre-stellar cores, more evolved cores (Class I, II and III) and the sources of $M_{env}/M_* < 1$, respectively. These properties mentioned above is assumed that Class 0 is the previous evolutionary stage compared to Class I. However, some papers (e.g. Tamura et al. (1996)) suspected it and they implied that the Class 0 sources may be the edge-on Class I sources since the disks of the sources absorb the central stellar emissions. Therefore, the precise definitions of Class 0 sources are under discussions.

6.1.2 The previously known X-ray-emitting Class 0 Source and its Location

6.1.3 NGC2264 Star Forming Region

NGC2264 is a star forming region located in the eastern side of the Mon OB1 giant molecular cloud, where the richest stellar cluster in Mon OB1 resides (see Figure 6.2). The optical and near-infrared images are shown in Figure 6.3. NGC2264 is exceptionally well-studied at all wavelengths: e.g.) (Allen, 1972; Kruegel et al., 1987; Margulis et al., 1988; Scarrott & Warren-Smith, 1989; Schreyer et al., 1997; Ward-Thompson et al., 2000; Nakano et al., 2003; Schreyer

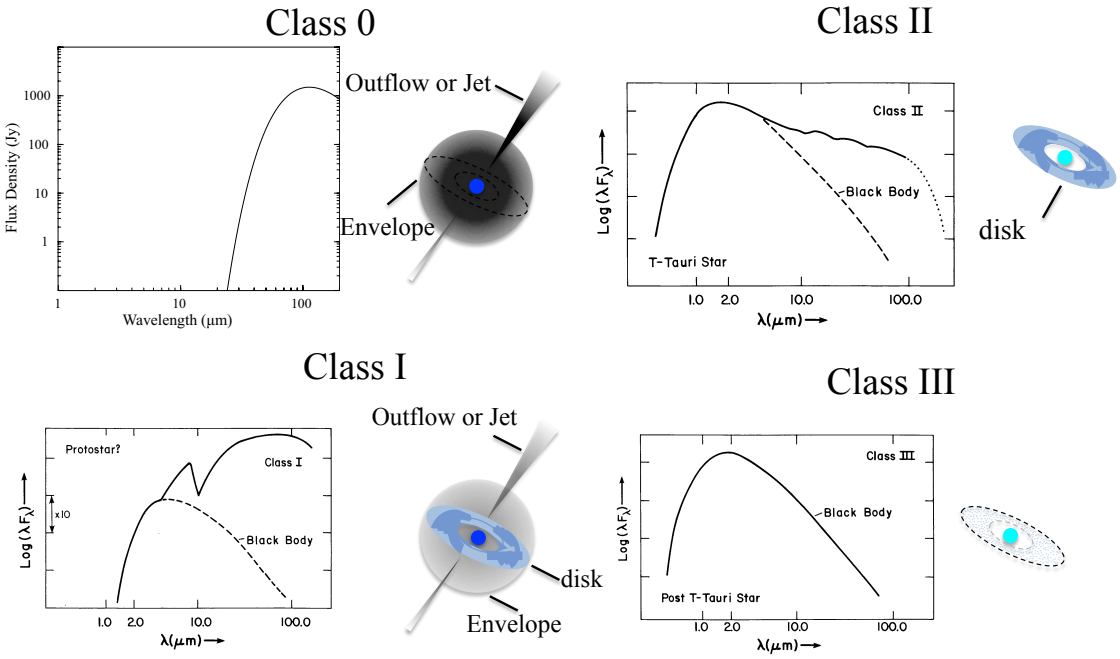

Figure 6.1: schematic SEDs and images of Class 0 – III

The SEDs of Class 0 and Class I – III are cited from Andre et al. (2000) and Lada (1987), respectively.

et al., 2003; Reipurth et al., 2004a,b; Flaccomio et al., 2006; Peretto et al., 2006; de Wit et al., 2009; Maury et al., 2009). NGC2264 was discovered by Friedrich Wilhelm Herschel in 1784 and listed in his catalog (Dahm, 2008). NGC2264 is composed of many OB stars, young stars and nebulosities surrounding them, and there are some distinct sources. In Figure 6.3a, a bright star located in the north of the image is S Monocerotis (S Mon), which is an O7 V massive star multiple binary (Gies et al., 1993, 1997) and is believed to be ionizing Cone Nebula seen in south of the image. In Figure 6.3b, the brightest star illuminating near the center of the image is IRS 1 (Allen's infrared source) discovered by Allen (1972). IRS 1 is implied as an B-type star (Schwartz et al., 1985) and there are no disks around IRS1 (Schreyer et al., 2003). Maury et al. (2009) plotted it on the M_{env} – L_{bol} diagram, which indicates the evolutionary stage of a star or a core, and

IRS1 is suggeste
as shown in Figu
will mention it i

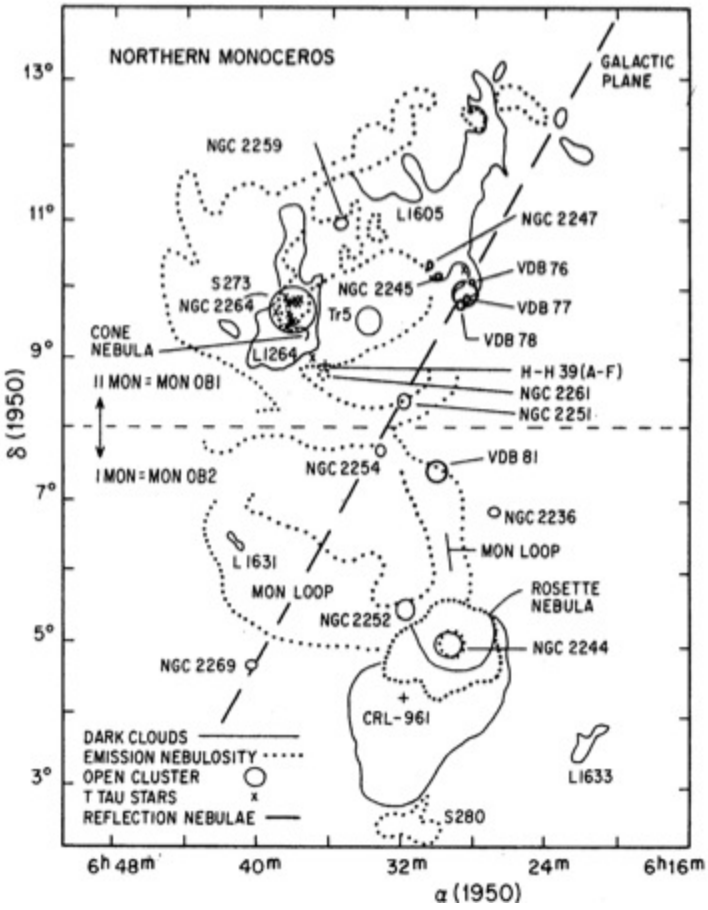

Figure 6.2: The map of northern Monoceros region

This shows some of most important objects (Pérez, 1991). NGC2264 lies on the north-west of this map.

6.1.4 NGC2264C

In NGC2264, there are two labeling with alphabets; one is based on ^{12}CO (1–0) and ^{13}CO(1–0) mapping (Crutcher et al., 1978) and the other is based on ^{12}CO (1–0) outflow mapping (Margulis et al., 1988). We use the latter labeling since these labeling is often used. The outflow region NGC2264C is located around IRS1 and is a active star forming site. There are many observations to investigate star formations with all wavelength (Allen, 1972; Kruegel et al., 1987; Margulis et al., 1988; Scarrott & Warren-Smith, 1989; Schreyer et al., 1997; Ward-Thompson et al., 2000; Nakano et al., 2003; Schreyer et al., 2003; Reipurth et al., 2004a,b; Flaccomio et al., 2006; Peretto et al., 2006; de Wit et al., 2009; Maury et al., 2009). Nakano et al. (2003) and Schreyer et al. (2003) shows that there is a low-density cavity of the remnant cloud core observed in molecular lines ($H^{13}CO^+$ or CS (2–1)). Schreyer et al. (2003) shows that there

are several embedded stars around IRS1 and they suggested that these stars are in the low-density cavity. As labeling by Margulis et al. (1988), some outflows in the region were observed with higher resolution using IRAM Plateau de Bure interferometer (PdBI) (Maury et al., 2009). They used ^{12}CO (2–1) line to investigate outflows in detail and they detected 11 red-shifted and blue-shifted lobes. From the collimation of outflow, they determined the driving sources for some lobes and the driving sources were millimeter cores detected by Peretto et al. (2006, 2007). However, they cannot determined the other lobes since the lobes are poorly collimated, too far away from the protostellar clump or too blended with other lobes. These show that the outflows in NGC2264C are very complex (see Figure 6.5). Water maser is detected in NGC2264C Genzel & Downes (1977) but the driving source was not identified.

6.2 VLBI Results

We show a typical water maser spectrum of our observations in Figure 6.6. We detected four water maser spots in the LSR velocity ($V_{\rm LSR}$) range from $6.77\,{\rm km\,s^{-1}}$ to $7.61\,{\rm km\,s^{-1}}$. These spots are grouped into two features. Each feature is defined as a group of spots emitting at velocities and with positions deferent by less than the beam size. The beam size of each epoch is shown in Table 3.4. The spots ID 1, 2 and 3 make feature 1. These 3 maser spots were detected from epoch 1 to epoch 8. The spot ID 4 makes feature 2. This spot was detected only from epoch 7 to epoch 9. Feature 1 is located 22 arcsec away from feature 2, which is discussed in section 5.5.2.

In order to obtain the annual parallax, we adopted the assumptions that the observed maser spots have no acceleration and the reference source J0643+0857 is fixed on the sky. Therefore, the motion of the maser spots relative to the reference source, J0643+0857, projected along each celestial coordinate is thought as the combination of a sinusoidal (parallax) and a linear motion (proper motion). To estimate the parallax, we used only the maser spots of feature 1 since we could detect feature 2 only in 3 epochs. We performed the least square fitting of the position offset $(\Delta\alpha^{(i)}, \Delta\delta^{(i)})$ of the maser spot ID i in the feature located at (α, δ) at time t using the following equations;

$$\Delta\alpha^{(i)}\cos\delta = \varpi(-\sin\alpha\cos\lambda_\odot + \cos\epsilon\cos\alpha\sin\lambda_\odot) + (\mu_\alpha^{(i)}\cos\delta)t + \alpha_0^{(i)}\cos\delta \tag{6.2}$$

$$\Delta\delta^{(i)} = \varpi(\sin\epsilon\cos\delta\sin\lambda_\odot - \cos\alpha\sin\delta\cos\lambda_\odot - \cos\epsilon\sin\alpha\sin\delta\sin\lambda_\odot) + \mu_\delta^{(i)}t + \delta_0^{(i)}, \tag{6.3}$$

where $(\mu_\alpha^{(i)}, \mu_\delta^{(i)})$ is the proper motion vector of the maser spot ID i, t is time, ϖ is the annual parallax, $\lambda_\odot$ is ecliptic longitude of the Sun at t, ϵ is the inclination of the ecliptic coordinates and (α_0, δ_0) is the spot position at $t = 0$. We fitted the positions of the three maser spots of feature 1 simultaneously with one common parallax, and different proper motions and position offsets for individual spots.

The total error of the maser position is estimated by the quadratic sum of the systematic error and the random error. The systematic error is called as "error floor" (e.g. Sanna et al. (2009)). We can estimate the random error since

it is formulated as $\theta_{\rm beam}/SNR$ (Reid et al., 1988). It is very difficult to estimate the accurate "error floor" because there are many factors such as residual phase of phase referencing, the error in zenith delay of the troposphere and the ionosphere, the error in calibration of the instrumental offset and blending of maser spots, and so on and we cannot know the all factors (e.g. Hachisuka et al. (2006); Honma et al. (2007); Nakagawa et al. (2008), etc). Therefore, we estimated the total error as the reduced χ^2 is unity. Hereafter, we refer the total error as the "positional uncertainty". The positional uncertainty is assumed to be the same at all epochs and is (reduced χ^2) $= \chi^2/\nu = 1$, where χ^2 is the squared sum of the residuals of fitting over the square of the uncertainty of one epoch, ν is the degree of freedom in the fitting i.e. the total number of data points minus the total number of parameters. In our fitting, $\nu = 22 - 7 = 15$ when we used only right ascension data of maser positions and $\nu = 44 - 13 = 31$ when we used both right ascension and declination data. When we fitted both right ascension and declination, the resultant uncertainty of each epoch is 0.219 mas and 1.879 mas for right ascension and declination, respectively. When we fitted the data only in right ascension, the resultant uncertainty of each epochs is 0.148 mas. The quality of the fit along the declination is poor. This is due to the low declination of the target source ($< |10^\circ|$) and the beam sidelobes elongated in declination. Similar cases are described in previous papers (e.g. Kurayama et al. (2011)). The detailed method and the causes of the errors are reported in previous papers (e.g. Honma et al. (2007); Kurayama et al. (2011), etc).

Figure 6.7 shows observed positions and results of the fitting in right ascension and declination. All spots clearly show the sinusoidal parallactic motion. We conducted the fitting for right ascension only because of the reason mentioned above. The resultant parallax was 1.356 ± 0.098 mas, corresponding to the distance of 738^{+57}_{-50} pc. In this paper, we used this value as the final parallax estimation. We note that we obtained the annual parallax to be 1.362 ± 0.145 mas, corresponding to the distance of 734^{+87}_{-71} pc using both right ascension and declination. This is consistent with the value estimated with right ascension only. The estimated proper motions of all spots and parallax of feature 1 are shown in Table 6.1 and the fitting results of the proper motions are shown in Figure 6.7.

Previous distance estimations of NGC2264 report two inconsistent values: one estimation is about 750 pc (Sung et al., 1997; Turner, 2012). This distance was measured with photometric observations. The other is about 900 pc (Baxter et al., 2009). It was measured based on the estimated stellar sizes from photometry and rotation velocity with an assumption of randomly oriented spin axes. Our estimation from annual parallax shows that the optical distance is the reliable one.

We conducted the proper motion fitting of feature 2, with the assumption that feature 2 has the same parallax as feature 1. The fitting results are shown in Table 6.1 and Figure 6.8. The estimated proper motion was $(\mu_\alpha \cos\delta, \mu_\delta) =$ (23.91 $\pm$ 4.29, $-$29.81 $\pm$4.27) mas yr^{-1}.

We estimated the peculiar motions using a Galactic flat rotation model with

Galactic constants of $R_0 = 8.05$ kpc and $\Theta_0 = 235$ km s^{-1} (Honma et al., 2012), together with the solar motion of $(U_\odot, V_\odot, W_\odot) = (+10.3\,\mathrm{km\,s^{-1}}, +15.3\mathrm{km\,s^{-1}}, +7.7\,\mathrm{km\,s^{-1}})$ (Ando et al., 2011). The peculiar motions and the position of the water masers are shown in Table 6.2 and Figure 6.9.

Table 6.1: Parallax and proper motions

Parallax results					
Fitting ID	Parallax ϖ [mas]		Note[a]		
1	1.362 ± 0.145		R.A. and Dec.		
2	1.356 ± 0.098		R.A. only		
Detected positions and Flux Densities					
Spot ID	R.A.(J2000)	Dec.(J2000)	$\Delta\alpha\cos\delta^d$ [mas]	$\Delta\delta^d$ [mas]	Flux Density[e] [Jy beam^{-1}]
1[b]	$6^h41^m9.8594^s$	$+9°29'14.672''$	−8.81	−27.94	1.04
2[b]	$6^h41^m9.8594^s$	$+9°29'14.672''$	−8.89	−27.81	1.26
3[b]	$6^h41^m9.8594^s$	$+9°29'14.672''$	−8.92	−27.76	1.14
4[c]	$6^h41^m10.1214^s$	$+9°29'36.133''$	3921.20	21432.79	5.64
Proper motions					
Spot ID	V_{LSR} [km s^{-1}]	$\mu_\alpha\cos\delta$ [mas yr^{-1}]	μ_δ[mas yr^{-1}]		
1[b]	6.77	−0.87 ± 0.58	−6.23 ± 3.05		
2[b]	7.19	−1.08 ± 0.58	−5.92 ± 3.06		
3[b]	7.61	−0.92 ± 0.58	−6.01 ± 3.06		
4[c]	7.19	28.32 ± 3.16	−33.53 ± 3.14		

[a] The data used to estimate the annual parallax.
[b] Maser spots used to estimate the annual parallax.
[c] The proper motion of the spot was estimated by assuming the parallax of 1.356 ± 0.098 mas.
[d] The positions of water maser spots with respect to $(\alpha_{\mathrm{J2000.0}}, \delta_{\mathrm{J2000.0}})$= $(6^h41^m9^s86, +9°29'14''.7)$.
[e] Peak flux density of the spot at the first detection.

6.3 NH_3 Mapping

Figure 6.10 shows the profile map at 186 positions in NH_3 (1,1), (2,2), and (3,3) lines. Significant NH_3 (1,1), (2,2), and (3,3) emissions were detected with better than 3 in the signal to noise ratio at 120, 51, and 7 positions, respectively. The NH_3 line spectrum comprises five quadruple hyperfine components consisting of a main line and two symmetric pairs of satellite lines. The typical spectra in (1,1), (2,2) and (3,3) lines at the 8 representative positions are shown in Figure 6.11. In (1,1) line, we also detected satellite lines at 31 positions.

The velocity integrated intensity maps in these three lines are shown in Figure 6.12. The velocity range was from 2 to 11 km s^{-1} which covered the main line. The (1,1) emission is distributed in $16' \times 19'$ or 3.5 pc × 4.2 pc. The overall distribution is elongated along the galactic plane at a position angle of PA

Table 6.2: peculiar motions

In the cartesian galactic coordinate				
	U^a [km s^{-1}]	V^b [km s^{-1}]	W^c [km s^{-1}]	$\sqrt{U^2+V^2+W^2}$ [km s^{-1}]
Feature 1	+3.7	−9.6	−4.1	11.2
Feature 2	+53.6	−132.2	+43.1	149.0
In the equatorial coordinate				
	ΔV_α [km s^{-1}]	ΔV_δ [km s^{-1}]	ΔV_r [km s^{-1}]	$\sqrt{\Delta V_\alpha^2+\Delta V_\delta^2}$ [km s^{-1}]
Feature 1	+0.8	−11.2	−0.1	11.2
Feature 2	+103.2	−107.3	−0.1	149.0

[a] The positive peculiar motion means locally toward the galactic center.
[b] The positive peculiar motion means locally in the direction of the galactic rotation.
[c] The positive peculiar motion means toward the north galactic pole.
We used the flat rotation with $R_0 = 8.05$ kpc, $\Theta_0 = 235$ km s^{-1}, as the kinetic model of the Galaxy.

$\sim 150°$ on the equatorial coordinates. Two clouds are clearly seen in the mapping area. The most intense peak is located at (α, δ)=($6^{\rm m}41^{\rm m}10.2^{\rm s}, +9°29'34''$), which corresponds to NGC 2264 C. The second intense peak is located at (α, δ) = ($6^{\rm h}41^{\rm m}6.1^{\rm s}, +9°34'34''$), which corresponds to NGC 2264 D. The distribution is well traced in the ^{13}CO and C^{18}O lines (Ridge et al., 2003). Kruegel et al. (1987) observed NGC 2264 C and NGC 2264 D in the NH_3 (1,1) and (2,2) emission lines using Effelsberg 100 m telescope. Our mapping area is larger than theirs. Our map is the first map in the (3,3) emission line. The (2,2) emissions are detected at NGC 2264 D and NGC 2264 C. The (3,3) emission is detected at NGC 2264 C.

6.4 Identifying the Driving Sources of the Maser Features

We detected two water maser features separated by about 22 arcseconds. The large separation and the large difference in peculiar velocities suggest that these two maser features are associated with two different driving sources. Based on the position and motion of each maser feature, we identify the source candidate for each feature.

6.4.1 The Driving Source of Feature 1

We looked for the driving source of feature 1 based on the peculiar motion and the position. At the position of feature 1, we found a dense molecular cloud core in both N_2H^+ line and 3.2 mm continuum maps of Peretto et al. (2007). In these maps, both the cloud core and feature 1 are located south of the clump CMM4 (see Figure 6.9). Hereafter we call the cloud core as "CMM4S". The central source of CMM4S should be the driving source of feature 1 based on its position and the peculiar motion.

6.4.2 The Driving Source of Feature 2

In many cases the driving source of a maser feature can be detected in the infrared. We, therefore, checked point source catalogs based on 2MASS, AKARI, IRAS, MSX, Spitzer, and WISE observations (Beichman et al., 1988; Egan et al., 2003; Skrutskie et al., 2006; Ishihara et al., 2010; Wright et al., 2010). We also checked the image taken with these satellites except for the AKARI. However, we could not identify any infrared sources due to saturation of the strong source NGC 2264 IRS1.

A centi-meter radio continuum source has been found in association with the driving sources of many outflows in star-forming regions. We found the 3.6 cm continuum source NGC 2264 VLA3 (Reipurth et al., 2004b) 80 mas north-west from feature 2 (see Figure 6.9). It is close to feature 2 but the separation is beyond the positional ambiguity in both observations, 50 mas for the VLA3 and 3 mas for feature 2. The direction of feature 2 from VLA3 on the sky is aligned to the direction of the peculiar motion of feature 2. We, therefore, think that feature 2 has its own driving source and it is associated with VLA3, although in this region many outflows were detected in the CS and CO lines (Schreyer et al., 2003; Maury et al., 2009).

Feature 2 has the peculiar motion as large as about 150 $\mathrm{km\,s^{-1}}$. A water maser outflow with such high velocity has been observed in some other massive star-forming regions like W49N (Gwinn et al., 1992). With this large motion it requires about 2 years to the distance from VLA3 to current position of feature 2.

The location of IRS1 on the sky is as close as 2.2 arcsec to feature 2. The positional ambiguity of IRS1 is about 1.6 arcsec by Schreyer et al. (2003) and the direction of feature 2 from IRS1 on the sky is not aligned to the direction of the peculiar motion of feature 2. Therefore, we do not think that IRS1 is the driving source of feature 2. Also, feature 2 does not seem to be associated with the jet-like structure near IRS1 (Schreyer et al., 1997, 2003) due to the same reason.

6.5 An X-ray Source Associated with Feature 1

At approximately 940 mas north-west from the position of feature 1, we found an X-ray source (see Figure 6.9). The positional ambiguities of X-ray source and feature 1 are 620 mas and 3 mas, respectively. The source is listed in Flaccomio et al. (2006) as the source number 299 in their Table 1 and that 1269 in their Table 3, although they are identical. We call the X-ray source as FMS2-1269. The X-ray detection is reliable and about 20 photons were detected without any NIR or MIR source around it.

Flaccomio et al. (2006) classified FMS2-1269 not to be an extragalactic source. We, therefore, believe that this X-ray emission is associated with a source embedded in the dense cloud core, CMM4S. In order to assess the X-ray properties, we re-analyzed the X-ray spectrum of the source, using the same data of Flaccomio et al. (2006). The X-ray spectrum is shown in Figure 6.13.

We fitted the data with an absorbed thin thermal plasma model. In the fitting, we used an X-ray spectral fitting package, XSPEC ver 12.7.0, which is provided by the High Energy Astrophysics Science Archive Research Center (HEASARC). For the thin thermal plasma model, we used *apec* model (Smith et al., 2001), and for the photo-electric absorption model, we used *wabs* model which uses Wisconsin cross-sections (Morrison & McCammon, 1983). Since the photon statistics is low, we fixed the plasma temperature to 3 keV, and the abundance to 0.3 $Z_{\odot}$, both of which are typical values for a Class I source in the quiescent phase (e.g. Imanishi et al. (2001)). Using these values we obtained emission measure (EM)[1] and the column density of H atom ($N_{\rm H}$). The best-fit values for the EM and the $N_{\rm H}$ are 9.4 (2.6 – 24.) $\times 10^{53}$ cm^{-3} and 5.4 (2.5 – 9.2) $\times 10^{23}$ cm^{-2}, respectively. The errors indicate 90% confidence level. The obtained $N_{\rm H}$ corresponds to the column density of H_2 molecules, $N_{\rm H_2}$ = 2.7 (1.3 – 4.6) $\times 10^{23}$ cm^{-2}. We note that the estimated $N_{\rm H_2}$ corresponds to the region in the foreground of the central star. For the column density of the dust core, i.e. that from one side to the other of the core, we should double it. We, therefore, give the column density of the core in H_2 molecules to be $N^{\rm X}_{\rm H_2}$, 5.4 (2.5 – 9.2) $\times 10^{23}$ cm^{-2}.

To make comparison, we estimated the column density from the 3.2 mm continuum map in Peretto et al. (2007). Because the continuum source is unresolved with their synthesized beam size ($5.3'' \times 3.8''$), we can only derive the beam averaged value. To estimate the gas column density, we adopted the following equation after (Motte et al., 1998):

$$N^{\rm dust}_{\rm H_2} = \frac{S^{\rm beam}_{\rm 3.2mm}}{\mu\, m_{\rm H}\, \Omega_{\rm beam}\, \kappa_{\rm 3.2mm}\, B(T_{\rm d})} \tag{6.4}$$

where, $S^{\rm beam}_{\rm 3.2mm}$ is the flux density at 3.2 mm integrated over the beam, μ = 2.33 is the mean molecular weight of the gas, $m_{\rm H}$ is the mass of a hydrogen atom, $\Omega_{\rm beam}$ is the beam solid angle, $\kappa_{\rm 3.2mm}$ = 1.3 $\times$ 10^{-3} cm^2 g^{-1} Peretto et al. (2007) is the dust opacity at 3.2 mm per unit gas mass column density and $B(T_{\rm d})$ is the Planck function with a dust temperature $T_{\rm d}$. From the 3.2 mm continuum map (Peretto et al., 2007), we estimated the beam averaged peak flux density is 2.4 mJy beam^{-1}. Using $T_{\rm d}$ =15 K as Peretto et al. (2007), we got $N^{\rm dust}_{\rm H_2}$ =2.6 $\times 10^{23}$ cm^{-2}. It is consistent with the estimation from X-ray absorption. We should note that $N^{\rm dust}_{\rm H_2}$ is the beam averaged value, which means the peak value can be lager than that. We, therefore, use $N^{\rm X}_{\rm H_2}$ as the actual value of the H_2 column density. It supports that FMS2-1269 is the embedded central source of CMM4S and then the driving source of feature 1.

[1]In radio astronomy, EM is defined as $\int n_{\rm e}\, n_{\rm p}\, dx$ integrated along the line of sight, where $n_{\rm e}$ and $n_{\rm p}$ are number densitis of electrons and photons, respectively. In X-ray astronomy, EM is defined as $\int n_{\rm e}\, n_{\rm p}\, dV$ integrated over the volume of X-ray plasma. We use the latter in this paper.

6.6 The Characteristics of FMS2-1269

We checked the high resolution infrared images in K band and 11.9 μm band obtained by Schreyer et al. (2003). In these images (Figure 6.14) and even in the large K band image around IRS1 as Figure 1 of Schreyer et al. (2003), we found no sources at the position of feature 1. Schreyer et al. (2003) observed NGC2264 with SOFI at the New Technology telescope (NTT) in near-infrared K band. The limiting magnitude of SOFI in their observations is 15.5 mag with 3 sigma noise level (K. Schreyer & S. Bringfried, private communication). A Class I source has 1.7 – 5.7 mag in K band absolute magnitude calculated from the apparent magnitude in the figure 24 of Aspin et al. (1994). At the distance of 738 pc, a Class I source can be seen with 11.1 – 15.1 mag. Therefore, we should see the source in the image of Schreyer et al. (2003) if FMS2-1269 were a Class I. In addition, FMS2-1269 was not detected in mid-infrared image of Schreyer et al. (2003) and the limiting flux is 0.5 Jy (K. Schreyer & S. Bringfried, private communication). Neither detection in mid nor near infrared band suggests that FMS2-1269 is a deeply embedded source and may be much younger than the Class I phase i.e. in the Class 0 phase.

The difference between the Class 0 and Class I phases is earlier or later than the envelope dissipation phase. Therefore, we should assess the dissipation of the CMM4S envelope to distinguish Class 0 from Class I. We made rough estimation of the density of CMM4S using the column density divided by the expected geometrical depth. We assumed the depth is the same as the apparent size of CMM4S i.e. 4.5″ in the 3.2 mm map (Peretto et al., 2007) since CMM4S is not resolved with the 5.3″ × 3.8″ beam. We derive the density for CMM4S of 10^6 cm^{-3}. It is enough high compared with that of typical molecular cloud core. Therefore, CMM4S should be before the envelope dissipation, that is in the Class 0 phase.

To assess its evolutionary stage, it is important to establish the mass of CMM4S. We estimated the mass following two methods; the mass from column density with X-ray absorption and that from dust emission. As shown in section 5.2, we estimated the H_2 column density of the gas associated with CMM4S to be 5.4 (2.5 – 9.2) $\times 10^{23}$ cm^{-2} from the X-ray absorption. It gives the core mass to be $M_{\rm X} \simeq 2.5$ (1.2 – 4.3) $M_\odot$, if the core size is 5.3″ × 3.8″. The actual mass may be slightly smaller than it because the actual size may be smaller than that. Using the 3.2 mm continuum map, we estimated the mass from the following equation after Andre et al. (1996):

$$M_{\rm dust} = \frac{S_{3.2{\rm mm}}\, D^2}{\kappa_{3.2{\rm mm}}\, B(T_{\rm d})} \tag{6.5}$$

where D is the distance toward the source. From the equation, we estimated the core mass to be $M_{\rm dust} = 1.4 - 2.3\, M_\odot$. The mass is consistent to that obtained from X-ray absorption. We adopt the envelope mass of CMM4S is about $2\, M_\odot$.

The bolometric luminosity of CMM4S is another important parameter. To estimate it, we should know the spectral energy distribution (SED) or the bolometric temperature. Although it is difficult to draw the SED due to poor ob-

servations of continuum flux densities, we can give a reasonable limit to the luminosity.

If we assume the SED is single temperature blackbody of 15 K, the bolometric temperature of CMM4S is 1.6 $L_{\odot}$. The upper limit at 11.9 μm and in K band give the upper limit of the single blackbody temperature to be 110 K. In this case, we can estimate the bolometric luminosity of CMM4S to be $3.5 \times 10^3\, L_{\odot}$. Non detection in K band suggests that the source should not show a significant excess in shorter wavelength. Therefore, we conclude the luminosity of CMM4S should be between 1.6 and $(3.5 \times 10^3)\, L_{\odot}$, although the actual luminosity should be fairly lower than the upper limit because of the reason shown below.

In Figure 6.15, we plot CMM4S (FMS2-1269) on the $M_{\rm env}$ – $L_{\rm bol}$ diagram shown in Maury et al. (2009). The horizontal bar along the bolometric luminosity axis corresponds to the range derived with single temperature blackbody between 15 K and 110 K. The vertical bar along the envelope mass axis corresponds to the mass range as we estimated above. In Figure 6.15, the blue trajectories indicate the model evolutionary tracks shown in Andre et al. (2000) and Maury et al. (2009). CMM4S should be in the darker half of the horizontal bar range, since CMM4S is in the earlier phase than the dissipation phase. In this case, CMM4S is on the track of about 2 $M_{\odot}$ envelope mass and will grow up to a low mass star.

The association of water maser with CMM4S also supports that it is a Class 0 source. Furuya et al. (2001, 2003) shows that a Class 0 source has much higher detection rate of water maser emission than that of a Class I source.

6.7 Comparison with Other X-ray-emitting Class 0 Candidate

To know the X-ray emission mechanism of a YSO, it is important to establish the relation between X-ray emission and its class. A Class I source is widely recognised as an X-ray emitter; e.g. in Rho Oph region, the X-ray detection rates are as high as 70% in both bona-fide Class I sources and Class I candidates (Imanishi et al., 2001). However, only several Class 0 candidates have been detected in the X-ray band; an X-ray source in OMC 3 region (Tsuboi et al., 2001), IRS 3A in Lynds 1448 (Tsujimoto et al., 2005), SMM 1B (=IRS 7B) in R CrA (Hamaguchi et al., 2005), TC 4 in the Trifid Nebula (Rho et al., 2004), BIMA 2 (=IRAS21391+5802) in the IC 1396N globule (Getman et al., 2007). Getman et al. (2007) present a $M_{\rm env}$–$L_{\rm bol}$ diagram to indicate the evolutionary track and the current conditions of the dust cores of Class 0 candidates with X-ray detection. The atomic hydrogen column densities of these sources range (2.8 – 10) $\times 10^{23}$ cm^{-2}. Our estimation of CMM4S (FMS2-1269), $\sim 5 \times 10^{23}$ cm^{-2}, is well in this range.

The intrinsic X-ray luminosity of the X-ray source associated with CMM4S is derived as 1 $\times 10^{31}$ erg s^{-1} in the 0.5 – 10 keV band at 738 pc. It is well in the range for the intrinsic X-ray luminosity from a Class 0 candidate; $\sim 10^{30}$ erg s^{-1} for OMC-3 region and $30 < \log L_{\rm X} < 31$ erg s^{-1} for R CrA. Therefore,

FMS2-1269 shows similar properties in X-ray as the other Class 0 candidates with X-ray emission. The main difference between FMS2-1269 and the other X-ray emitting Class 0 candidates is the non-detection at mid-infrared band and this suggests that CMM4S has lower temperature and can be even younger than the other X-ray emitting Class 0 candidates.

The column densities of CMM4S (FMS2-1269) and previously detected Class 0 candidates have larger column densities than that of a typical Class I source since the typical value of a Class I source is $\sim 0.3 \times 10^{23}$ cm^{-2} (Tsujimoto et al., 2002). However, the X-ray luminosities of FMS2-1269 and the previously detected Class 0 candidates are similar to the typical value of a Class I source, $\sim 10^{30}$ erg s^{-1} (Tsujimoto et al., 2002).

6.8 Gas Temperature

The temperature of the dense molecular gas is one of important parameters to know the star formation activity. In order to obtain it, NH_3 is a good prove. We can estimate the optical depth of the main lines from the intensity ratio of the satellite lines to the main line and of each rotational level, and the rotational temperature of NH_3 is derived from the ratio of the main lnes at different rotational levels.

Figure 6.16 shows the correlation between integrated intensities of main and satellite lines. We plotted only the data detected better than 3 σ level in both main and satellite lines. The correlation plots show the ratio of the main to satellite line intensities, $R_{\rm m/s}$, is fairly uniform over the whole observed area. The estimated value of $R_{\rm m/s}$ from the inner and outer pairs of the satellite lines are estimated to be 2.89 ± 0.11, and 3.47 ± 0.15, respectively. These values give the consistent values of the optical depth of the (1,1) main line as τ(1,1,m) = 0.65 ± 0.13 – 0.72 ± 0.14, respectively, using the method shown in Ho & Townes (1983). Therefore we concluded the optical depth of the NH_3 (1,1) main line τ(1,1,m) $\simeq 0.7 \pm 0.1$.

Using this value, we estimated the rotational temperature of NH_3, $T_{\rm rot}$. So, the $R_{(2,2)/(1,1)}$ is a good indicator of the rotational temperature of NH_3 from the intensity ratio of the NH_3 (1,1) and (2,2) main lines at each position. Figure 6.17 shows the correlation plot of the (1,1) and the (2,2) integrated intensity of the NH_3 main line in the whole area, NGC2264 C and NGC 2264 D regions. We could not find any significant difference in $T_{\rm rot}$ and the average $R_{(2,2)/(1,1)}$ was 0.34 ± 0.02 for the whole area. In the case that the rotational temperature is less than 20 K, it is very close to the gas kinetic temperature, $T_{\rm k}$ (Ho & Townes, 1983). Therefore, the average kinetic temperature of gas in NGC 2264 is $T_{\rm k} = 16 \pm 1$ K. In NGC 2264 C region, Ward-Thompson et al. (2000) found that the spectral energy distribution (SED) in the mm/submm and far infrared regimes shows two temperatures of 17 K and 38 K. Our kinetic temperature was consistent with that of the colder dust. We, therefore, suggest that the distribution of the colder dust is extended in whole area since the temperature of NH_3 is uniform in the whole area. Actually the warm molecular gas should be confined in small regions. Around IRS 1, Kruegel et al. (1987) reported the

temperature derived from NH_3 (1,1) and (2,2) lines to be 28 K and 60 K derived from the NH_3 (2,2) and (4,4) lines. Although these estimations are much hotter than our results, they are consistent with that of the hotter dust. The hotter gas and dust may be located locally around IRS1.

6.9 Mass of the Molecular Clouds and the Star Formation Efficiency

To estimate the mass of the clouds, we used two methods; integration of the column density, $M_{\rm LTE}$, and estimation under the virial equilibrium, $M_{\rm vir}$. To estimate the either mass, we estimated the size of each cloud from its apparent size of $\theta_{\rm s} = (\theta_{\rm max}\theta_{\rm min})^{1/2}$ with the beam deconvolution, where we fitted the contours having half of the peak in the integrated intensity map with ellipse and we obtained $\theta_{\rm max}$ and $\theta_{\rm min}$ along the major and minor axes, respectively. The estimated value of $(\theta_{\rm max}, \theta_{\rm min})$ are ($3'.6$, $2'.5$) and ($5'.1$, $3'.0$) for NGC 2264 C and D, respectively. Using our distance of 738 pc, we obtained the sizes of NGC 2264 C and D to be 0.53 and 0.76 pc, respectively. To obtain the total column density of NH_3, we used the method of Mangum et al. (1992).

The total of column densities of NH_3 in all states is estimated to be $N_{\rm tot}(NH_3)$ $\sim 10^{16}$ cm^{-2} from the column density at (1,1) level derived from the τ(1,1,m) and the observed line width under the assumption of the local thermal equilibrium (LTE) with the estimated kinetic temperature for each cloud. Using the abundance ratio of $X(NH_3) = 10^{-8}$ (Irvine et al., 1987), we obtained the masses under this procedure, or the LTE masses, are $1.29 \times 10^3 M_\odot$ and $1.26 \times 10^3 M_\odot$ for NGC 2264C and D, respectively. If we assume a spherically symmetric geometry, these masses give the averaged H_2 number density in the cloud to be $n(H_2) \sim 10^4$ cm^{-3}. This value is consistent to the NH_3 critical density and it suggests that the estimated LTE masses are valid.

Using the observed line width of full width at half maximum of 3.2 km s^{-1} and 2.7 km s^{-1} for C and D, the virial mass is estimated to be $M_{\rm vir} \sim 6.9 \times 10^2$ $M_\odot$ for either cloud. The LTE mass and the virial mass are consistent. This suggest that the two clouds are in virial equilibrium. We summarized the obtained parameters of NGC 2264 C and D clouds in Table 6.3.

We compared our mass with the mass previously estimated since the gas masses were estimated from a variety of observation. Kruegel et al. (1987) estimated the mass of NGC 2264 C and NGC 2264 D to be about 460 $M_\odot$ each other from their NH_3 observations. Wolf-Chase et al. (1995) estimated the LTE mass of NGC 2264 C and NGC 2264 D from their CS (2 – 1) observations and the masses were 1900 – 2500 $M_\odot$ and 500 – 700 $M_\odot$, respectively. Schreyer et al. (1997) estimated the virial mass of NGC 2264 C from the mean line width of all $C^{18}O$ and CS (7 – 6) line in their observations and the mass was 580 $M_\odot$. Ward-Thompson et al. (2000) estimated the mass of NGC C2264 C from their milli-meter continuum observations and the mass of about 620 $M_\odot$. Since most of these masses were estimated using the distance of 800 pc, we recalculate with our distance and the value were shown above. The our mass was consistent with all previous mass within an order of magnitude.

On the other hand, the sum of the masses of T Tauri and OB stars within a $10'$ (2.1 pc) radius from IRS1 is estimated to be 119 $M_\odot$ (Dahm & Simon, 2005). Teixeira et al. (2012) estimated the stellar mass of 718 ± 121 $M_\odot$ within the area of 1264.48 arcmin^2 with Spitzer observations. The stellar mass estimation of Dahm & Simon (2005) did not include any infrared embedded sources and that of Teixeira et al. (2012) did not include the other sources without infrared sources. Also, the area is different from the area that we estimated the gas mass with NH_3 observations. Then, we adopted the stellar mass of 173 $M_\odot$. The stellar mass estimated by multiplying the ratio of our observed area and that of Teixeira et al. (2012) by the stellar mass of Teixeira et al. (2012) based on the assumption that the stars uniformly distribute in the region. Using our distance and mass and this stellar mass, we could estimate the SFE of NGC2264 to be $\gtrsim 7$ – 13%.

We compare our SFE with previous results and other regions. Teixeira et al. (2012) estimated the SFE of NGC 2264 to be $\gtrsim$ 25 % at their adopted distance of 913 pc. This SFE is re-estimated $\gtrsim$ 16 % using our distance of 738 pc. This value is consistent with ours.

The SFE of some other regions were reported in Toujima et al. (2011). In their paper, the SFE of NGC 7000, NGC 1333 and L1228 were estimated from the gas masses of NH_3 and the stellar masses of T Tauri stars and their SFEs were 36 – 62 %, 16 % and 8%. As we compared the SFE of NGC2264 with them, the SFE of NGC2264 is smaller than that of NGC7000 which there are triggered star formations in and is same as those of NGC 1333 and L1228 which there are not triggered star formations in.

Table 6.3: The physical properties of two clouds.

Name	d (pc)	τ(1,1,m)	$T_{\rm rot}$ (K)	$N_{\rm TOT}(NH_3)$ (cm^{-2})	$n(H_2)$ (cm^{-3})	$M_{\rm LTE}$ ($M_\odot$)	$M_{\rm vir}$ ($M_\odot$)
NGC 2264 C	0.53	0.62 ± 0.14	17 ± 1	2.3×10^{15}	5.7×10^4	1.29×10^3	6.9×10^2
NGC 2264 D	0.76	0.76 ± 0.14	15 ± 1	2.3×10^{15}	3.7×10^4	1.26×10^3	6.9×10^2

6.10 Summary

We conducted VLBI observations of water masers toward the NGC 2264 star forming region and we detected two water maser features, separated by about 22 arcseconds in N - S directions: we named the southern feature as feature 1 and northern feature as feature 2. In addtion to VLBI observations, we performed the NH_3 mapping with Kahima 34 m telescope. Our conclusions are summarized as the followings:

1. We precisely determined the parallax of NGC2264 to be 1.356 ± 0.098 mas, corresponding to the distance of 738^{+57}_{-50} pc. This supports the photometric distance previously known.

2. Near feature 1, we found an X-ray source (FMS2-1269) listed in Flaccomio et al. (2006) and a dust continuum core CMM4S shown in Peretto et al. (2007). These sources are physically associated with feature 1. CMM4S shows large H_2 column density about 5.4×10^{23} cm^{-2}. The mass of CMM4S is estimated to be about 2 $M_\odot$.

3. We suggest that FMS2-1269 is an X-ray-emitting Class 0 source based on the followings; (1) no detection in the near- nor mid- infrared emission, (2) high volume density compared with that typical for a molecular cloud core, (3) the association with the water masers, (4) showing X-ray properties similar to those of previously detected X-ray-emitting Class 0 candidates.

4. Feature 2 should be associated with the centimeter continuum source VLA3. It could be associated with a relatively high-velocity outflow, with speed as fast as 150 km s^{-1}.

5. We estimated the gas temperature, the column density, the LTE mass, the virial mass and SFE based on our NH_3 mapping observations. The averaged kinetic temperature of gas is 16 ± 1 K using the optical depth. From the total column density of NH_3, $N_{\rm tot}(NH_3) \sim 10^{16}$ cm^{-2}, our distance of 738 pc and the abundance ratio $X(NH_3) = 10^{-8}$, the LTE mass of NGC 2264 C and D are estimated to be $1.29 \times 10^3 M_\odot$ and $1.26 \times 10^3 M_\odot$, respectively. We also estimated the virial mass and the virial mass are consistent with LTE mass. From our gas mass and the stellar mass derived by Teixeira et al. (2012), the SFE is estimated to be $\gtrsim 7$ – 13%.

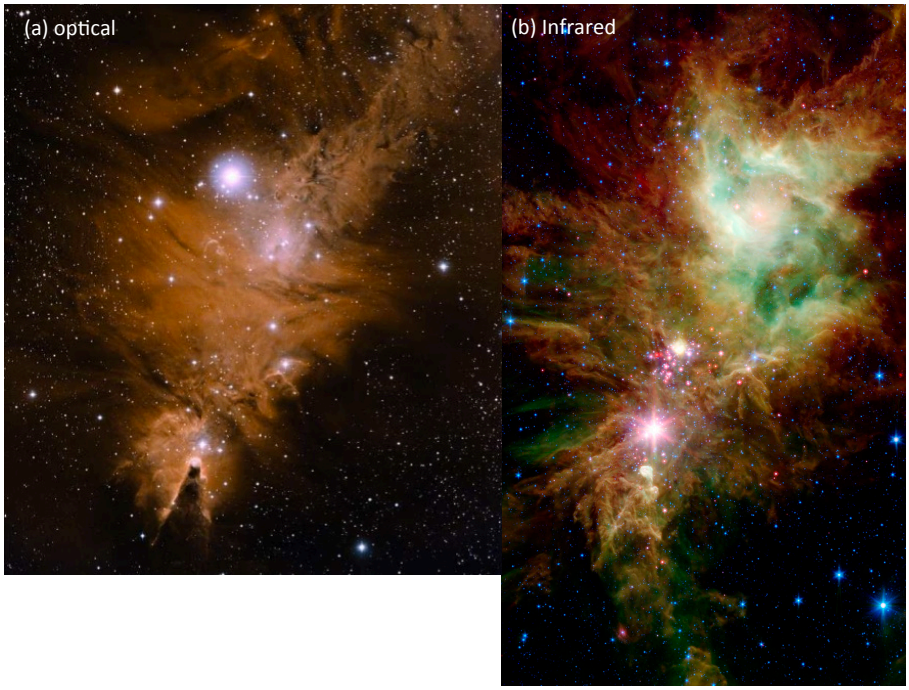

Figure 6.3: The whole picture of the NGC2264 star forming region.

Both image shows north is up and east is left. a)The three color composite image with optical ionized line filters, OIII (light-blue), Hα (red-orange) and SII (blue-violet) (Dahm, 2008). The field of view is approximately $0.75° \times 1.00°$. The massive star binary S Mon is the bright star located in the north side of this image and is believed to be the ionizing source of the bright rimmed Cone Nebula (Dahm, 2008). b)The combined *Spitzer* IRAC-MIPS image of almost whole NGC 2264 region showing 3.6 and 4.5 μm (blue), 5.8 μm (cyan), 8 μm (green), and 24 μm (red) emission (Dahm, 2008). The bright star near the image center is NGC2264 IRS1 (Allen's infrared source) which NGC2264C surrounds and the cluster located in the north of IRS1 is called as snow-flake cluster (NGC2264D). In contrast with optical line image (a), S Mon is not much distinct.

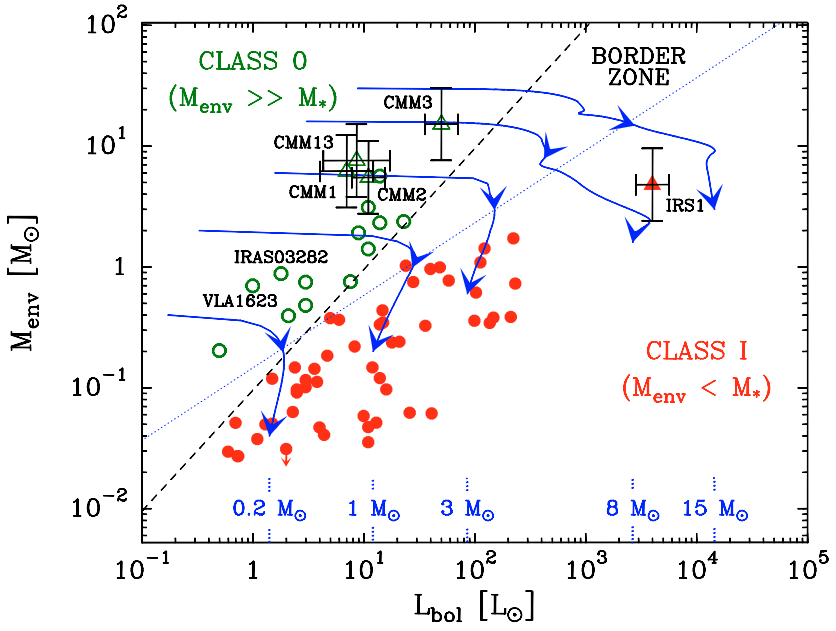

Figure 6.4: Envelope mass versus bolometric luminosity diagram

Envelope mass versus bolometric luminosity diagram shown in Maury et al. (2009). Open green circles, filled red circles, open green triangles with error-bars and filled red triangles with error-bars shows Class 0 objects in other regions, Class I objects in other regions, cores in NGC2264 identified by Peretto et al. (2007) and IRS1. The blue arrows indicate the model evolutionary track and the computed final mass is shown below.

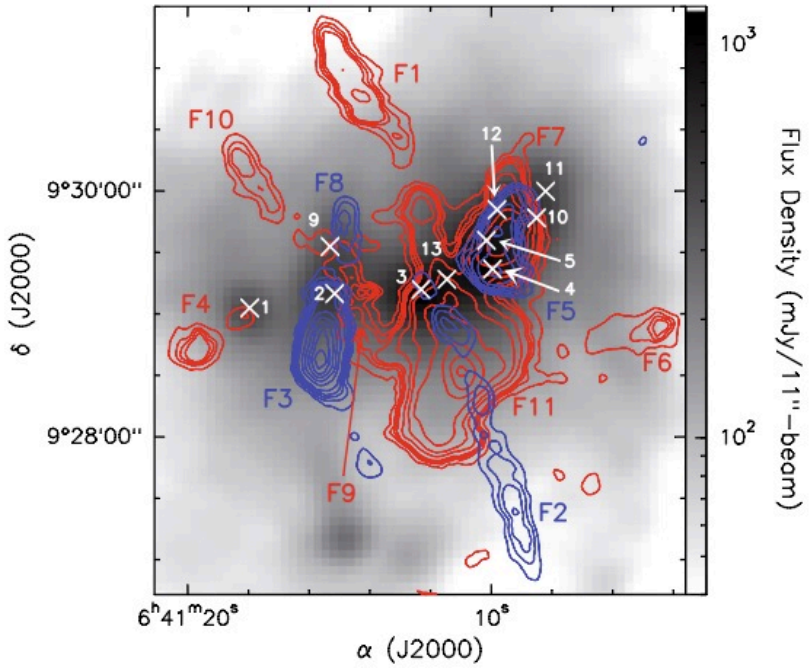

Figure 6.5: The detailed outflow map in NGC2264C

The detailed outflow map in NGC2264C (Maury et al., 2009). Blue contours show the levels of ^{12}CO (2–1) intensity integrated between −27 km s^{-1} and 2 km s^{-1} in the blue-shifted part of the line, and go from 5 to 98 K km s^{-1} . Red contours are levels of intensity integrated between 13 km s^{-1} and 34 km s^{-1} in the red-shifted part of the line, and go from 5 to 110 K km s^{-1}. The background grey scale is 1.2 mm dust continuum emission shown in Peretto et al. (2007) and the white cross and numbers indicate the peak of the continuum core.

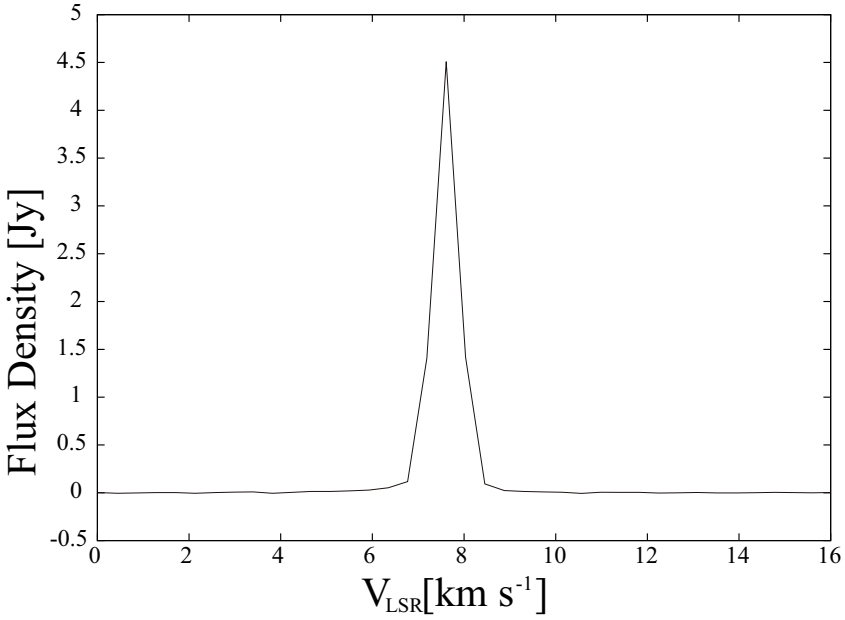

Figure 6.6: The cross-power spectrum of the water maser emission of NGC2264

The cross-power spectrum of the water maser emission of NGC2264 obtained from the baseline of Mizusawa – Iriki on 2010 March 8.

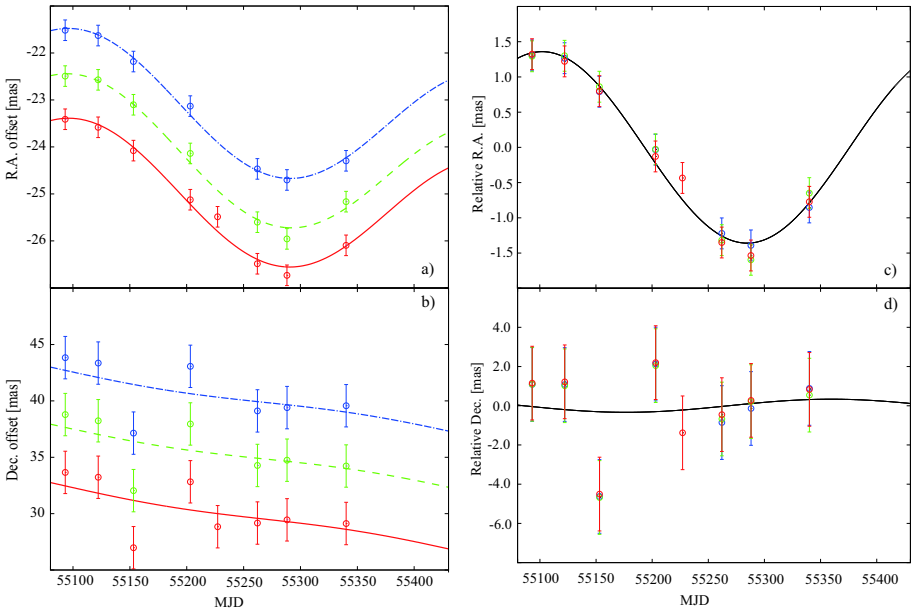

Figure 6.7: The time variations and The parallactic sinusoids of NGC2264

(a) The time variation in right ascension of three maser spots (ID 1 – 3, which compose feature 1, shown in Table 6.1) in NGC 2264 obtained by VLBI observations at 22 GHz with VERA. The filled circles with error bars and lines represent the observed positions and the fitting results for them. The errors are 0.219 mas. The red (solid), green (dotted) and blue (dashed) lines correspond to the maser spots ID 1, 2 and 3, respectively. We shifted +1 mas and +2 mas for ID 2 and 3 to avoid overcrowding. (b) The same as (a) but in declination and we shifted +5 mas and +10 mas for spot ID 2 and 3. The errors are 1.879 mas. (c) The parallactic sinusoid in right ascension after removing the proper motions. (d) The same as (c) but in declination.

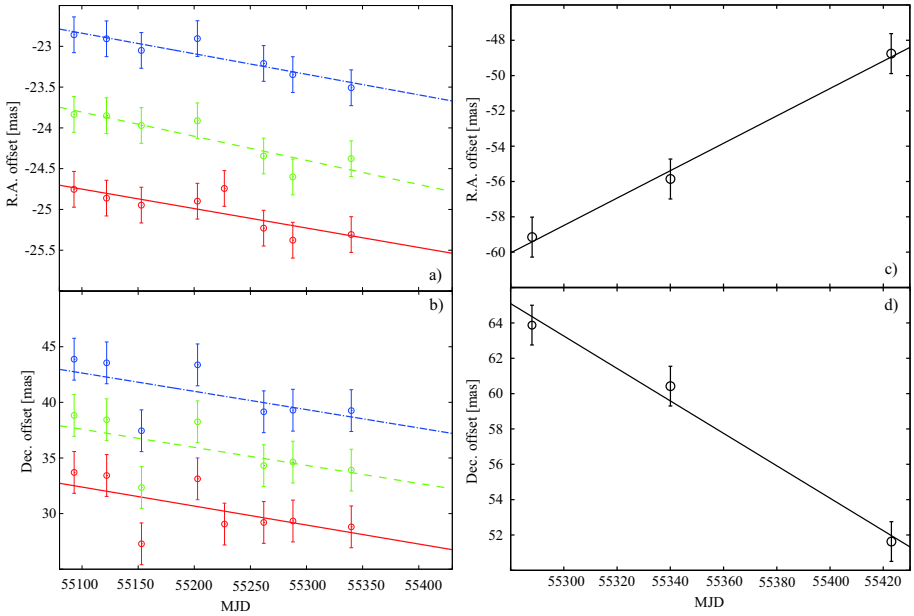

Figure 6.8: The proper motions of water masers inNGC2264

(a) The proper motions after removing the annual motion. The plot report the right ascension change with time of the three maser spots (ID 1 – 3), which compose feature 1, as indicated in Table 6.1. The colors (lines), symbols and shifts are the same as (a) in Figure 2. (b) The same as (a) but in declination. The colors, symbols and shifts are the same as (b) in Figure 2. (c) The same as (a) but for the maser spot ID 4, which composes feature 2, as indicated in Table 6.1. We show the result for spot ID4 based on the assumption that the spot has the same parallax as that of the other spots. (d) The same as (c) but in declination.

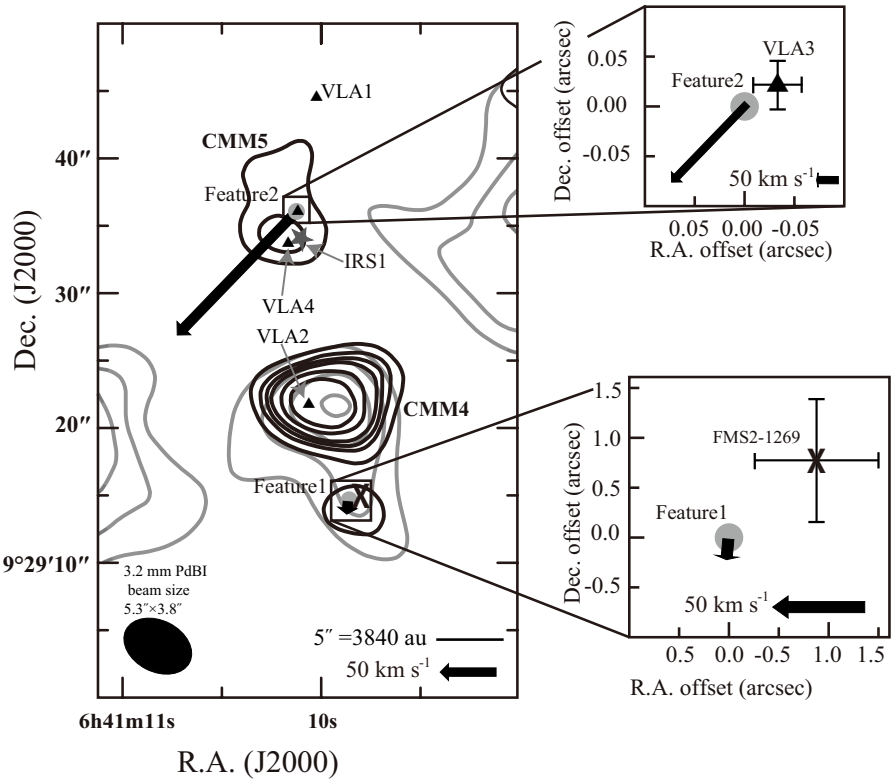

Figure 6.9: The detected masers and their peculiar motions

The grey filled circle and the black arrows show the detected masers and their peculiar motions. The solid grey and the solid black contours show N_2H^+ and 3.2 mm continuum emissions by Peretto et al. (2007), respectively. The black filled triangles show VLA 3.6 cm continuum sources shown in Reipurth et al. (2004b). Also, we showed the position of IRS1 and the X-ray source (FMS2-1269) posted on Flaccomio et al. (2006) with the star symbol and the black cross, respectively. The adopted coordinates of IRS 1 is $(\alpha_{J2000.0}, \delta_{J2000.0})$=($6^h41^m10^s.1$, $+9°29'\,34''.0$) as shown in the Table 1 of Schreyer et al. (2003). The left-bottom ellipse indicates the beam size ($5.3'' \times 3.8''$) of 3.2 mm PdBI observations by Peretto et al. (2007). The top-right panel is a blowup around feature 2 at $(\alpha_{J2000.0}, \delta_{J2000.0})$=($6^h41^m10^s.1214$, $+9°29'\,36''.133$). VLA 3 is shown as a filled triangle with its positional error of 50 mas. The bottom-right panel is a blowup around feature 1 at $(\alpha_{J2000.0}, \delta_{J2000.0})$=($6^h41^m09^s.8594$, $+9°29'\,14''.672$). FMS2-1269 is shown as a black cross with its positional error of 620 mas.

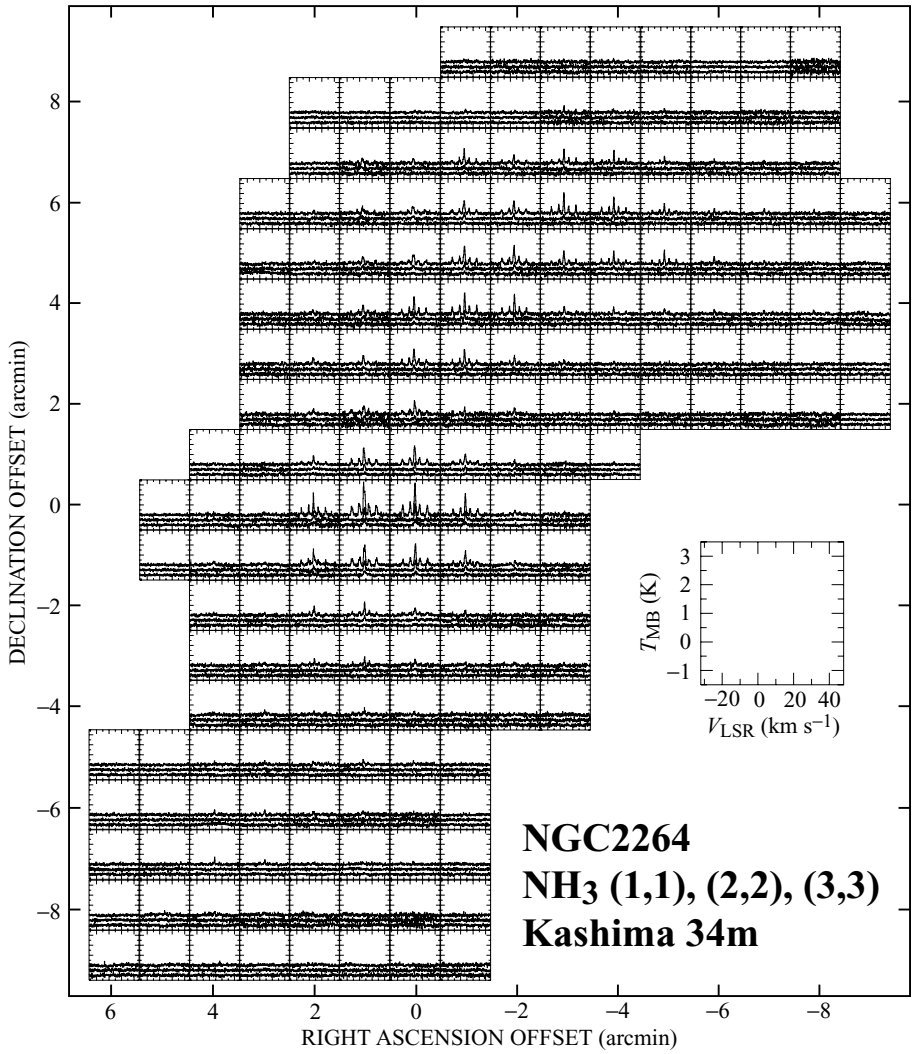

Figure 6.10: NH_3 Profile Map of NGC2264

All measured spectra in NH_3 (1,1), (2,2), (3,3) lines for NGC 2264. The scale of the spectra are indicated by the small box shown in the bottom right corner.

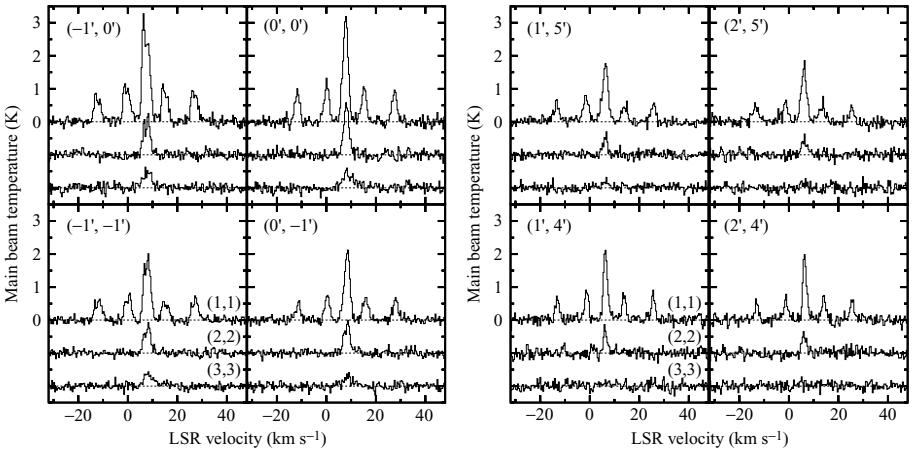

Figure 6.11: NH_3 spectra of NGC2264

The 8 representative spectra of NGC 2264. Grid spacing is $1'$. The position of the each spectrum in Figure 6.10 is shown in each top left corner.

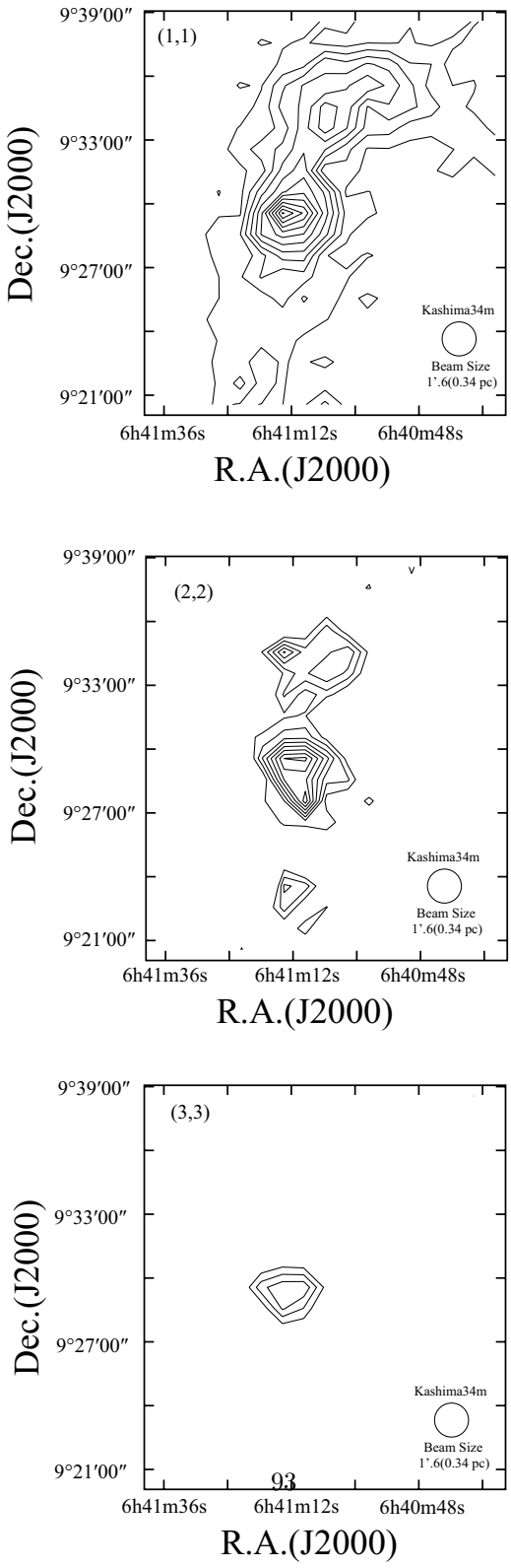

Figure 6.12: NH_3 Map of NGC2264

NH_3 integrated contour map (1,1), (2,2) and (3,3). The (1,1) map has a lowest contour level of 0.35 $\mathrm{K\,km\,s^{-1}}$ and an interval of 1 $\mathrm{K\,km\,s^{-1}}$. The contours of the (2,2) and (3,3) maps have a lowest level of 0.35 $\mathrm{K\,km\,s^{-1}}$ and an interval of 0.2 $\mathrm{K\,km\,s^{-1}}$. the circle at the bottom right corner shows the beam size.

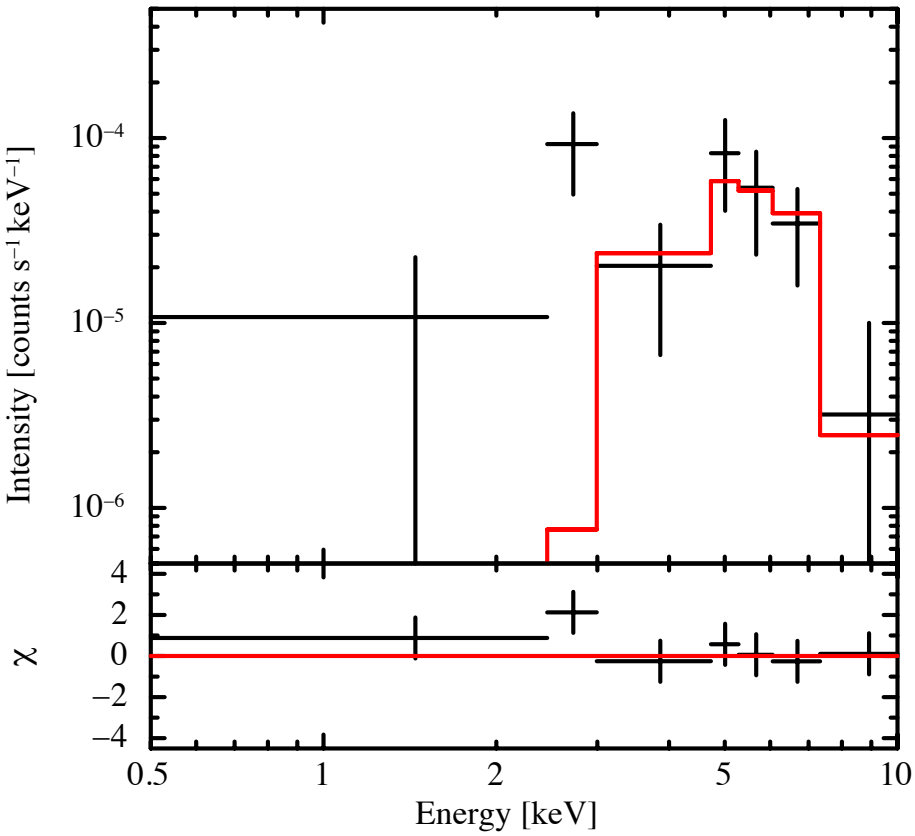

Figure 6.13: X-ray spectrum of FMS2-1269

X-ray spectrum of FMS2-1269 fitted with an absorbed coronal plasma model (*apec* model). The lower panel shows the residuals from the best-fit model. The red line and the black crosses indicate the final model and observed values, respectively.

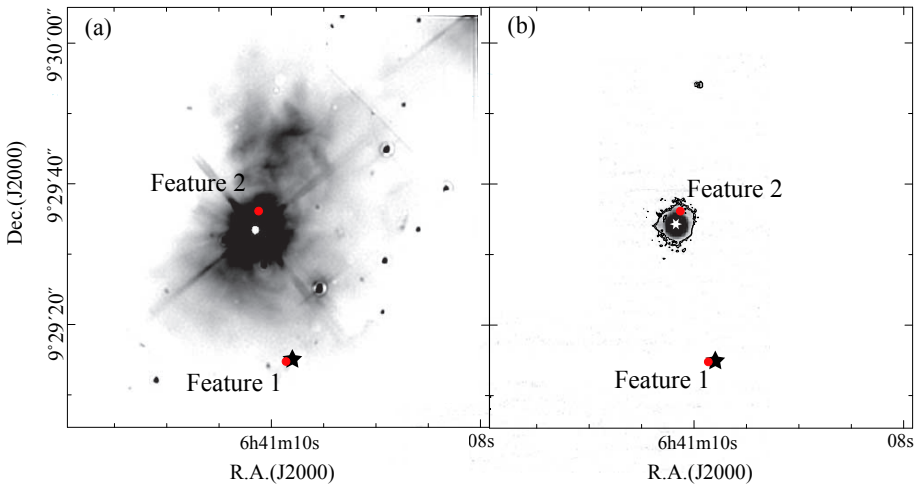

Figure 6.14: The infrared images around the maser features

a) The near infrared K band image reproduced from Schreyer et al. (2003). We showed the positions of the water maser features and the X-ray source with red filled circles and a star symbol. The central bright star is IRS 1. b) The mid infrared 11.9 μm band image reproduced from Schreyer et al. (2003). We showed the positions of the water maser features and the X-ray source with red filled circles and a black star symbol.

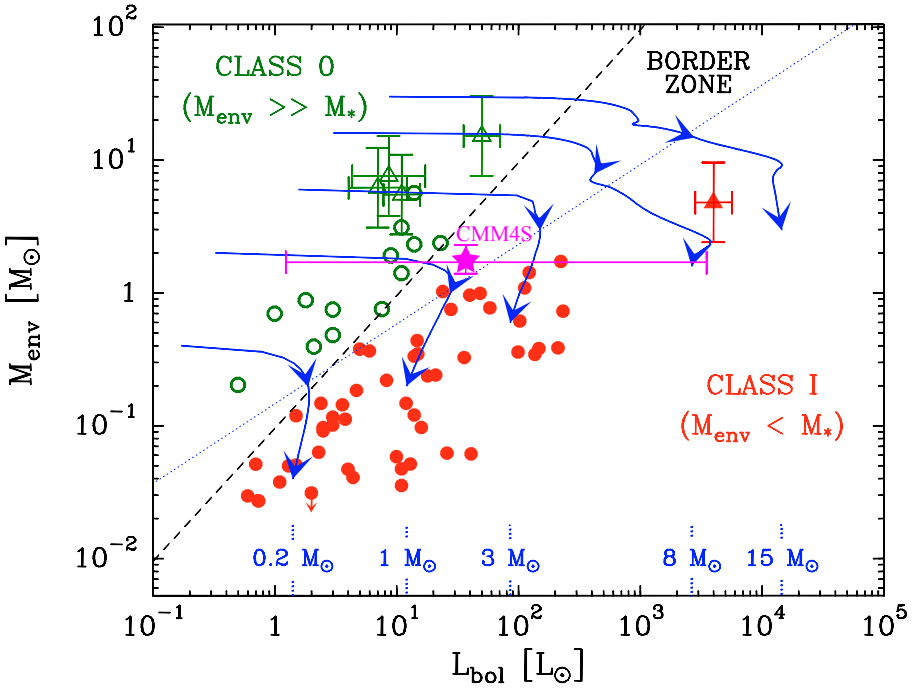

Figure 6.15: The plot of CMM4S on the $M_{\rm env}$ – $L_{\rm bol}$ diagram

The plot of CMM4S on the $M_{\rm env}$ – $L_{\rm bol}$ diagram overlaid on Figure 9 in Maury et al. (2009). Our plot is shown as a magenta star symbol with error, although we believe that CMM4S should be located in the darker half on the horizontal error range. As shown in Maury et al. (2009), the open and filled circles indicate Class 0 and I objects, respectively. The triangles show the other protostellar sources in NGC2264C region (open triangle) and NGC2264 IRS1 (filled triangle). The blue arrows show theoretical evolutionary tracks.

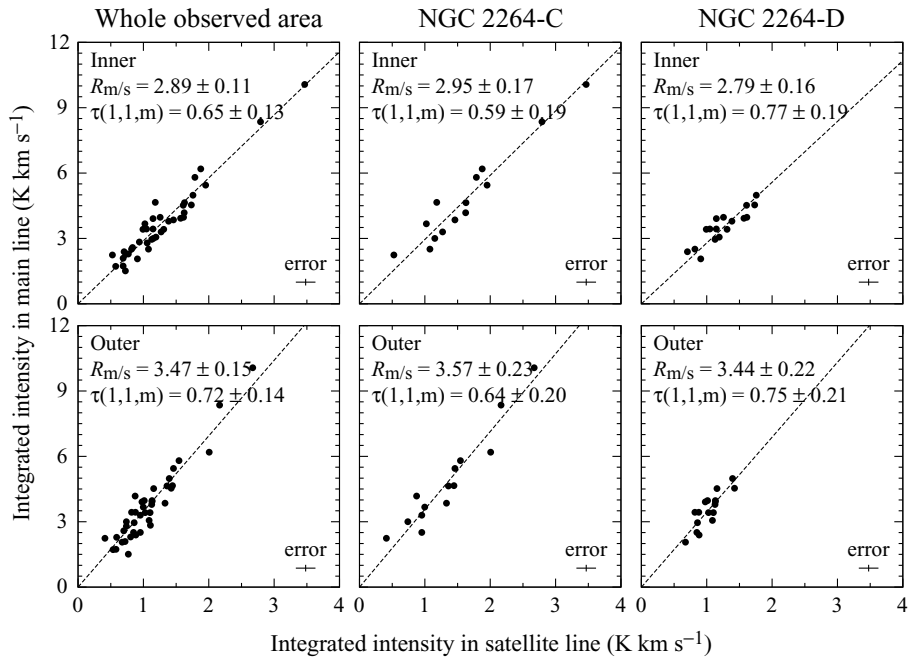

Figure 6.16: Correlations of the integrated intensity of the main line and satellite line

The upper three figures are calculated by using inner satellite line and the lower three figures were the scheme calculated by using outer satellite line. Also, we showed the estimated $R_{m/s}$s and optical depths at the top of each plot.

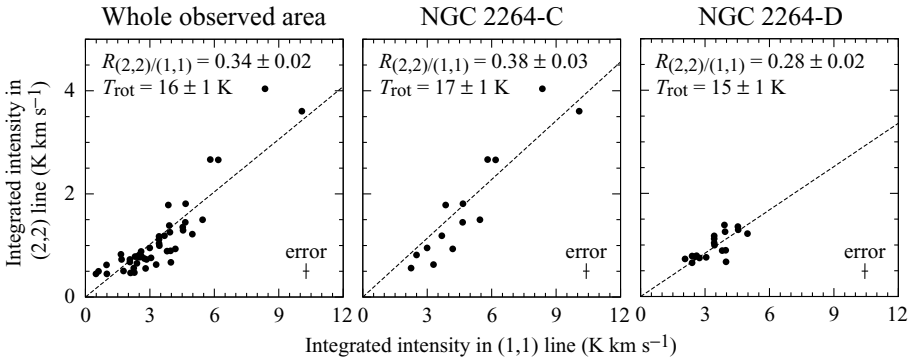

Figure 6.17: Correlations of the integrated intensity of the (2,2) line and (1,1) line

We showed the calculated $R_{(2,2)/(1,1)}$s and rotational temperatures at the top of each plot.

7 Summary and Future Works

7.1 Summary of my Thesis

In sections above, we showed some annual parallax measurements for the three targets (RX Boo, RW Lep and NGC2264). Two our distances of RX Boo and NGC2264 are consistent with that of the previous methods. We, therefore, confirmed that their assumptions are reasonable since the distance measured with parallax is most direct method to measure distance. Annual parallax toward the star or region became successful and the accurate distances are determined. Our distance measurements of the sources, RW Lep, are first distance measurements toward the star on the astronomy. These three annual parallax measurements gave us the precise discussions and new aspects; for RX Boo and RW Lep, we determined their luminosities, radii, mass. Our annual parallax measurements will give us the first accurate PL relations for Mira and SRVs. For NGC2264, we determined the actual size, density, luminosity, mass and a star formation. Our discussions of FMS2-1269 in NGC2264 indicated that it MAY BE Class 0 source, but we believe that it IS Class 0 source. We make some efforts to determine whether it is Class 0 or not. If the FMS2-1269 is Class 0 source, it gives us the limitation, which evolutionary stages the X-ray is emitted from. We did not obtain these achievements without our distance measurements and we must not forget the importance of the distance since it is the base of astronomy. The discussions without the accurate distance may be only the guess.

7.2 Future Works

We need more precise distances to discuss the large structure. The final destination of VERA is to make the map of MWG. However, we have only smaller than 100 distances. To make it, we must determine the more distance. I expect that VERA completes the extraordinary grand map of the MWG and that the galactic dynamics are clarified. The PL relations of Miras and SRVs are completed and they are bases of the further astronomical developments. I studied at the centimeter wavelength and with the resolution of small scale $\sim$ 1 mas, but the millimeter also approaches to the small scale. The Atacama Large Millimeter/submillimeter Array (ALMA) can observe the millimeter wavelength and resolve the structure of $\sim$ 10 mas, which is almost same with VERA. We have struggled with nothing (small) to compared with VERA data and we are eager to compare it with some the other wavelength data, which include more different informations. Thanks to ALMA, we can do it and VERA and ALMA will open the door of next generation of astronomy. In addition to radio wavelength, infrared or optical wavelengths are also important for astronomy. The Thirty Meter Telescope will be constructed in near future and it also clarify some mysterious phenomena.

7.2.1 FMS2-1269 and Class 0

We found the water maser feature accompanied with FMS2-1269. We thought that FMS2-1269 is Class 0 source. However, we were racked by the ambiguity of the Class 0 definitions. There are some definitions and we need to summarize the definitions. To show that FMS2-1269 is Class 0, we must know some things; 1) to resolve the core CMM4S, 2) the accurate density of CMM4S, 3) the SED of the FMS2-1269 / CMM4S 4) that we do not see the source from edge-on and 5) being powerful outflow from the source. 1) is to confirm the existence of the envelope and 2) is to know that the envelope has sufficiently dense. 3) is to investigate that FMS2-1269 is consistent with the empirical definition and with that of Andre et al. (2000). 4) is to show that it is not the edge-on source of the more evolved source (Class I, II and more evolved). 5) is based on the image and the definition of Andre et al. (2000) and to show that FMS2-1269 is consistent with them. If these are shown, FMS2-1269 becomes to a member of Class 0. Now, we can achieve them with ALMA, TMT and so on. We can do it !

7.2.2 The Driving Source of Feature 2 in NGC2264

We detected two water maser features; Feature 2 is drives by FMS 2-1269 and Feature 1 may be drives by VLA3. We have a question for Feature 1, which have large peculiar velocity. We wonder where the peculiar motion comes from since the peculiar velocity is estimated without subtraction of systematic (internal) motion. Two causes are considered; one is the case that the driving source VLA3 has large peculiar velocity and the other is the case that VLA3 has small velocity but water maser has large velocity. The former one indicates that the system of VLA3 has large peculiar velocity ($\sim$ 150 km s^{-1}) and this is especially high velocity. The latter one indicates that water maser flow has large velocity. The high velocity outflow velocity on the spectrum are shown in many papers and it indicates that they have the high velocity for the line-of-sight, but Feature 1 has small radial velocity. This implies that there are many high velocity outflow vertical to the line-of-sight. These two possibilities can be easily determined with the proper motion measurements of VLA3. Therefore, we will submit the proposal to VLA, to measure the proper motion of VLA3.

References

Aspin, C., Sandell, G., & Russell, A. P. G. 1994, A&AS, 106, 165

Allen, D. A. 1972, ApJL, 172, L55

Ando, K., Nagayama, T., Omodaka, T., et al. 2011, PASJ, 63, 45

Andre, P., & Montmerle, T. 1994, ApJ, 420, 837

Andre, P., Ward-Thompson, D., & Motte, F. 1996, A&A, 314, 625

Andre, P., Ward-Thompson, D., & Barsony, M. 2000, Protostars and Planets IV, 59

Andronov, I. L., & Kudashkina, L. S. 1988, Astronomische Nachrichten, 309, 323

Aringer, B., Höfner, S., Wiedemann, G., Hron, J., Jørgensen, U. G., Käufl, H. U., & Windsteig, W. 1999, A&A, 342, 799

Bachiller, R. 1996, ARA&A, 34, 111

Barrett, A. H., Schwartz, P. R., & Waters, J. W. 1971, ApJL, 168, L101

Baxter, E. J., Covey, K. R., Muench, A. A., et al. 2009, AJ, 138, 963

Bedding, T. R., & Zijlstra, A. A. 1998, ApJL, 506, L47

Bedding, T. R., Zijlstra, A. A., Jones, A., & Foster, G. 1998, MNRAS, 301, 1073

Beichman, C. A., Neugebauer, G., Habing, H. J., Clegg, P. E., & Chester, T. J. 1988, Infrared astronomical satellite (IRAS) catalogs and atlases. Volume 1: Explanatory supplement, 1,

Bessel, F. W. 1838, MNRAS, 4, 152

Binney, J. & Merrield, M. 1998, Galactic Astronomy (Princeton, NJ: Princeton Univ. Press), chap. 5.1

Boboltz, D. A., & Claussen, M. J. 2004, Bulletin of the American Astronomical Society, 36, 1357

Casanova, S., Montmerle, T., Feigelson, E. D., & Andre, P. 1995, ApJ, 439, 752

Chen, H., Myers, P. C., Ladd, E. F., & Wood, D. O. S. 1995, ApJ, 445, 377

Cheung, A. C., Rank, D. M., Townes, C. H., Thornton, D. D., & Welch, W. J. 1969, Nature, 221, 626

Cesaroni, R., Palagi, F., Felli, M., et al. 1988, A&AS, 76, 445

Chagnon, G., Mennesson, B., Perrin, G., Coudé du Foresto, V., Salomé, P., Bordé, P., Lacasse, M., & Traub, W. 2002, AJ, 124, 2821

Chikada, Y., Kawaguchi, N., Inoue, M., et al. 1991, Frontiers of VLBI, 79

Cioni, M.-R. L., Marquette, J.-B., Loup, C., et al. 2001, A&A, 377, 945

Cox, N. L. J., Kerschbaum, F., van Marle, A.-J., et al. 2012, A&A, 537, A35

Crutcher, R. M., Hartkopf, W. I., & Giguere, P. T. 1978, ApJ, 226, 839

Crocker, D. A., & Hagen, W. 1983, A&AS, 54, 405

Cutri, R. M., Skrutskie, M. F., van Dyk, S., et al. 2003, VizieR Online Data Catalog, 2246, 0 2001, A&A, 377, 945

Dahm, S. E., & Simon, T. 2005, AJ, 129, 829

Dahm, S. E. 2008, Handbook of Star Forming Regions, Volume I, 966

Dyck, H. M., Benson, J. A., van Belle, G. T., & Ridgway, S. T. 1996, AJ, 111, 1705

Egan, M. P., Price, S. D., Kraemer, K. E., et al. 2003, VizieR Online Data Catalog, 5114, 0

Enoch, M. L., Evans, N. J., II, Sargent, A. I., & Glenn, J. 2009, ApJ, 692, 973

ESA 1997, VizieR Online Data Catalog, 1239, 0

Feast, M. W., Glass, I. S., Whitelock, P. A., & Catchpole, R. M. 1989, MNRAS, 241, 375

Flaccomio, E., Micela, G., & Sciortino, S. 2006, A&A, 455, 903

Furuya, R. S., Kitamura, Y., Wootten, H. A., Claussen, M. J., & Kawabe, R. 2001, ApJL, 559, L143

Furuya, R. S., Kitamura, Y., Wootten, A., Claussen, M. J., & Kawabe, R. 2003, ApJS, 144, 71

Genzel, R., & Downes, D. 1977, A&AS, 30, 145

Getman, K. V., Feigelson, E. D., Garmire, G., Broos, P., & Wang, J. 2007, ApJ, 654, 316

Gies, D. R., Mason, B. D., Hartkopf, W. I., et al. 1993, AJ, 106, 2072

Gies, D. R., Mason, B. D., Bagnuolo, W. G., Jr., et al. 1997, ApJL, 475, L49

Glass, I. S., & Evans, T. L. 1981, Nature, 291, 303

Glass, I. S., & van Leeuwen, F. 2007, MNRAS, 378, 1543

W.Goetz, MVS N142, 1952

González Delgado, D., Olofsson, H., Kerschbaum, F., et al. 2003, A&A, 411, 123

Gordon, J. P., Zeiger, H. J., & Townes, C. H. 1955, Physical Review, 99, 1264

Greene, T. P., Wilking, B. A., Andre, P., Young, E. T., & Lada, C. J. 1994, ApJ, 434, 614

Groenewegen, M. A. T., & Whitelock, P. A. 1996, MNRAS, 281, 1347

Grosso, N., Montmerle, T., Feigelson, E. D., et al. 1997, Nature, 387, 56

Gwinn, C. R., Moran, J. M., & Reid, M. J. 1992, ApJ, 393, 149

Haikala, L. K., Nyman, L.-A., & Forsstroem, V. 1994, A&AS, 103, 107

Hachisuka, K., Brunthaler, A., Menten, K. M., et al. 2006, ApJ, 645, 337

Hamaguchi, K., Corcoran, M. F., Petre, R., et al. 2005, ApJ, 623, 291

Hedden, J., Benson, P. J., Little-Marenin, I. R., & Cadmus, R. R. 1991, Journal of the American Association of Variable Star Observers (JAAVSO), 20, 198

Herwig, F. 2005, ARA&A, 43, 435

Hirota, T., Ando, K., Bushimata, T., et al. 2008, PASJ, 60, 961

Ho, P. T. P., & Townes, C. H. 1983, ARA&A, 21, 239

Honma, M., Bushimata, T., Choi, Y. K., et al. 2007, PASJ, 59, 889

Honma, M., et al. 2008a, PASJ, 60, 935

Honma, M., Tamura, Y., & Reid, M. J. 2008b, PASJ, 60, 951

Honma, M., Nagayama, T., Ando, K., et al. 2012, PASJ, 64, 136

Høg, E., Fabricius, C., Makarov, V. V., et al. 2000, A&A, 355, L27

Ishihara, D., Onaka, T., Kataza, H., et al. 2010, A&A, 514, A1

Ita, Y., et al. 2004, MNRAS, 353, 705

Irvine, W. M., Goldsmith, P. F., & Hjalmarson, A. 1987, Interstellar Processes, 134, 561

Imanishi, K., Koyama, K., & Tsuboi, Y. 2001, ApJ, 557, 747

Jike, T., Fukuzaki, Y., Shibuya, K., Doi, K., Manabe, S., Jauncey, D. L. Nicolson, G. D., & McCulloch, P. M. 2005, Polar Geoscience, 18, 26

Jike, T., Fukuzaki, Y., Shibuya, K., Doi, K., Manabe, S., Jauncey, D. L. Nicolson, G. D., & McCulloch, P. M. 2005, Annual Report of the National Astronomical Observatory of Japan, 7, 48

Kamata, Y., Koyama, K., Tsuboi, Y., & Yamauchi, S. 1997, PASJ, 49, 461

Koo, B.-C. 1989, ApJ, 337, 318

Kamezaki, T., Nakagawa, A., Omodaka, T., et al. 2012, PASJ, 64, 7

Kawaguchi, N., Sasao, T., & Manabe, S. 2000, Proc. SPIE, 4015, 544

Kim, J., Cho, S.-H., & Kim, S. J. 2013, AJ, 145, 22

Knapp, G. R., Pourbaix, D., Platais, I., & Jorissen, A. 2003, A&A, 403, 993

Kobayashi, H., et al. 2003, Astronomical Society of the Pacific Conference Series, 306, 367

Koyama, K., Maeda, Y., Ozaki, M., et al. 1994, PASJ, 46, L125

Koyama, K., Hamaguchi, K., Ueno, S., Kobayashi, N., & Feigelson, E. D. 1996, PASJ, 48, L87

Kruegel, E., Guesten, R., Schulz, A., & Thum, C. 1987, A&A, 185, 283

Kučinskas, A., Hauschildt, P. H., Ludwig, H.-G., Brott, I., Vansevičius, V., Lindegren, L., Tanabé, T., & Allard, F. 2005, A&A, 442, 281

Kurayama, T., Master Thesis

Kurayama, T., Sasao, T., & Kobayashi, H. 2005, ApJL, 627, L49

Kurayama, T., Nakagawa, A., Sawada-Satoh, S., et al. 2011, PASJ, 63, 513

Kutner, M. L., & Ulich, B. L. 1981, ApJ, 250, 341

Lada, C. J. 1987, Star Forming Regions, 115, 1

Lada, C. J., & Wilking, B. A. 1984, ApJ, 287, 610

Leavitt, H. S. 1908, Annals of Harvard College Observatory, 60, 87

Lebzelter, T., & Obbrugger, M. 2009, Astronomische Nachrichten, 330, 390

Lewis, B. M., David, P., & Le Squeren, A. M. 1995, A&AS, 111, 237

Litvak, M. M., McWhorter, A. L, Meeks, M. L & Zeiger, H. J. 1966, *Phys.Rev.Lett*, 17, 821

Luo, B., Bauer, F. E., Brandt, W. N., et al. 2008, ApJS, 179, 19

Manabe, S., Yokoyama, K., & Sakai, S. 1991, IERS Techn. Note, 8, 61

Mangum, J. G., Wootten, A., & Mundy, L. G. 1992, ApJ, 388, 467

Mattei, J. A., Foster, G., Hurwitz, L. A.,Malatesta, K. H., Willson, L. A.,& Mennessier, M. O. 1997, Hipparcos - Venice '97, 402, 269

Margulis, M., Lada, C. J., & Snell, R. L. 1988, ApJ, 333, 316

Maury, A. J., André, P., & Li, Z.-Y. 2009, A&A, 499, 175

Mayer, A., Jorissen, A., Kerschbaum, F., et al. 2011, A&A, 531, L4

Min, C., Matsumoto, N., Kim, M. K., et al. 2014, PASJ, 29

Morrison, R., & McCammon, D. 1983, ApJ, 270, 119

Motte, F., Andre, P., & Neri, R. 1998, A&A, 336, 150

Myers, P. C., & Ladd, E. F. 1993, ApJL, 413, L47

Nakagawa, A., Tsushima, M., Ando, K., et al. 2008, PASJ, 60, 1013

Nakagawa, A., Omodaka, T., Handa, T., et al. 2014, accpted to PASJ (arXiv:1404.4463)

Nakajima, T. et al., 2007, PASJ, 59, 1005

Nakano, M., Sugitani, K., & Morita, K. 2003, PASJ, 55, 1

Noda, S., et al. 2004, MNRAS, 348, 1120

Nyu, D., Nakagawa, A., Matsui, M., et al. 2011, PASJ, 63, 63

O'Linger, J. C., Cole, D. M., Ressler, M. E., & Wolf-Chase, G. 2006, AJ, 131, 2601

Olofsson, H., González Delgado, D., Kerschbaum, F., & Schöier, F. L. 2002, A&A, 391, 1053

Pérez, M. R. 1991, RMXAA, 22, 99

Peretto, N., André, P., & Belloche, A. 2006, A&A, 445, 979

Peretto, N., Hennebelle, P., & André, P. 2007, A&A, 464, 983

Perkins, F., Gold, T., & Salpeter, E. E. 1966, ApJ, 145, 361

Perrin, G., Coudé du Foresto, V., Ridgway, S. T., Mariotti, J.-M., Traub, W. A., Carleton, N. P., & Lacasse, M. G. 1998, A&A, 331, 619

Perryman, M. A. C., et al. 1997, A&A, 323, L49

Price, S. D., Smith, B. J., Kuchar, T. A., Mizuno, D. R., & Kraemer, K. E. 2010, ApJS, 190, 203

Reid, M. J., & Moran, J. M. 1981, ARA&A, 19, 231

Reid, M. J., Schneps, M. H., Moran, J. M., et al. 1988, ApJ, 330, 809

Reipurth, B., Pettersson, B., Armond, T., Bally, J., & Vaz, L. P. R. 2004, AJ, 127, 1117

Reipurth, B., Rodríguez, L. F., Anglada, G., & Bally, J. 2004, AJ, 127, 1736

Rho, J., Ramírez, S. V., Corcoran, M. F., Hamaguchi, K., & Lefloch, B. 2004, ApJ, 607, 904

Ridge, N. A., Wilson, T. L., Megeath, S. T., Allen, L. E., & Myers, P. C. 2003, AJ, 126, 286

Roeser, S., Demleitner, M., & Schilbach, E. 2010, AJ, 139, 2440

Samus, N. N., Durlevich, O. V., & et al. 2009, VizieR Online Data Catalog, 1, 2025

Samus N.N., Durlevich O.V., Kazarovets E V., Kireeva N.N., Pastukhova E.N., Zharova A.V., et al., General Catalogue of Variable Stars (Samus+ 2007-2012), VizieR On-line Data Catalog: B/gcvs

Sanna, A., Reid, M. J., Moscadelli, L., et al. 2009, ApJ, 706, 464

Scarrott, S. M., & Warren-Smith, R. F. 1989, MNRAS, 237, 995

Schreyer, K., Helmich, F. P., van Dishoeck, E. F., & Henning, T. 1997, A&A, 326, 347

Schreyer, K., Stecklum, B., Linz, H., & Henning, T. 2003, ApJ, 599, 335

Schwartz, P. R., Thronson, H. A., Jr., Odenwald, S. F., et al. 1985, ApJ, 292, 231

Shibata, K. M., Kameno, S., Inoue, M., & Kobayashi, H. 1998, IAU Colloq. 164: Radio Emission from Galactic and Extragalactic Compact Sources, 144, 413

Shintani, M., Imai, H., Ando, K., et al. 2008, PASJ, 60, 1077

Skrutskie, M. F., Cutri, R. M., Stiening, R., et al. 2006, AJ, 131, 1163

Smith, R. K., Brickhouse, N. S., Liedahl, D. A., & Raymond, J. C. 2001, ApJL, 556, L91

Smith, B. J., Price, S. D., & Baker, R. I. 2004, ApJS, 154, 673

Soszyński, I., & Wood, P. R. 2013, ApJ, 763, 103

Speil, J. 2006, Journal of the American Association of Variable Star Observers (JAAVSO), 35, 88

Sung, H., Bessell, M. S., & Lee, S.-W. 1997, AJ, 114, 2644

Snyder, L. E., & Buhl, D. 1974, ApJL, 189, L31

Szymczak, M., Le Squeren, A. M., Sivagnanam, P., Tran Minh, F., & Fournier, A. 1995, A&A, 297, 494

Takaba, H., Ukita, N., Miyaji, T., & Miyoshi, M. 1994, PASJ, 46, 629

Takeuti, M., Nakagawa, A., Kurayama, T., & Honma, M. 2013, PASJ, 65, 60

Tamura, M., Ohashi, N., Hirano, N., Itoh, Y., & Moriarty-Schieven, G. H. 1996, AJ, 112, 2076

Taylor, M. D. 1987, Journal of the British Astronomical Association, 97, 277

Teixeira, P. S., Lada, C. J., Marengo, M., & Lada, E. A. 2012, A&A, 540, A83

Teyssier, D., Hernandez, R., Bujarrabal, V., Yoshida, H., & Phillips, T. G. 2006, A&A, 450, 167

Thaddeus, P., Mather, J., Davis, J. H., & Blair, G. N. 1974, ApJL, 192, L33

Thompson, R. R., Creech-Eakman, M. J., & van Belle, G. T. 2002, ApJ, 577, 447

Toujima, H., Nagayama, T., Omodaka, T., et al. 2011, PASJ, 63, 1259

Tsuboi, Y., Imanishi, K., Koyama, K., Grosso, N., & Montmerle, T. 2000, ApJ, 532, 1089

Tsuboi, Y., Koyama, K., Hamaguchi, K., et al. 2001, ApJ, 554, 734

Tsujimoto, M., Koyama, K., Tsuboi, Y., Goto, M., & Kobayashi, N. 2002, ApJ, 566, 974

Tsujimoto, M., Kobayashi, N., & Tsuboi, Y. 2005, AJ, 130, 2212

Turner, D. G. 2012, Astronomische Nachrichten, 333, 174

van Belle, G. T., Thompson, R. R., & Creech-Eakman, M. J. 2002, AJ, 124, 1706

van Leeuwen, F. 2007, A&A, 474, 653

van Leeuwen, F., & Fantino, E. 2005, A&A, 439, 791

Vlemmings, W. H. T., van Langevelde, H. J., Diamond, P. J., Habing, H. J., & Schilizzi, R. T. 2003, A&A, 407, 213

Vlemmings, W. H. T., & van Langevelde, H. J. 2007, A&A, 472, 547

Ward-Thompson, D., Zylka, R., Mezger, P. G., & Sievers, A. W. 2000, A&A, 355, 1122

Weaver, H., Williams, D. R. W., Dieter, N. H., & Lum, W. T. 1965, Nature, 208, 29

Weinreb, S., Barrett, A. H., Meeks, M. L., & Henry, J. C. 1963, Nature, 200, 829

Whitelock, P., Menzies, J., Feast, M., et al. 1994, MNRAS, 267, 711

Whitelock, P., Marang, F., & Feast, M. 2000, MNRAS, 319, 728

Whitelock, P., & Feast, M. 2000, MNRAS, 319, 759

Whitelock, P. A., Feast, M. W., & van Leeuwen, F. 2008, MNRAS, 386, 313

Wilson, W. J., & Barrett, A. H. 1972, A&A, 17, 385

Wilson, T. L., Batria, W., & Pauls, T. A. 1982, A&A, 110, L20

Winnberg, A., Engels, D., Brand, J., Baldacci, L., & Walmsley, C. M. 2008, A&A, 482, 831

Wolf-Chase, G. A., Walker, C. K., & Lada, C. J. 1995, ApJ, 442, 197

Wood, P. R., & Sebo, K. M. 1996, MNRAS, 282, 958

Wood, P. R. 2000, Publications of the Astronomical Society of Australia, 17, 18

Woodruff, H. C., Tuthill, P. G., Monnier, J. D., Ireland, M. J., Bedding, T. R., Lacour, S., Danchi, W. C., & Scholz, M. 2008, ApJ, 673, 418

Worthey, G., & Lee, H.-c. 2011, ApJS, 193, 1

de Wit, W. J., Hoare, M. G., Fujiyoshi, T., et al. 2009, A&A, 494, 157

Wright, E. L., Eisenhardt, P. R. M., Mainzer, A. K., et al. 2010, AJ, 140, 1868

Xiong, D. R., & Deng, L. 2007, MNRAS, 378, 1270

Yeşilyaprak, C., & Aslan, Z. 2004, MNRAS, 355, 601

Zacharias, N., Monet, D. G., Levine, S. E., et al. 2005, VizieR Online Data Catalog, 1297, 0

Zijlstra, A. A., Bedding, T. R., & Mattei, J. A. 2002, MNRAS, 334, 498

A Lutz-Kelker Bias

We explained the general problems in introductory chapter. However, we must take care of a point which the relation between distance D and parallax ϖ is non-linear. In this appendix chapter, we introduce Lutz-Klker bias.

Lutz-Klker bias indicate how accurate we can determine the parallax. The relation between distance D and parallax ϖ is

$$D = \frac{1}{\varpi} \tag{A.1}$$

as shown in section 1.2.4 and non-linear. Therefore, the probability of observed parallax are departed from that of true parallax when we observe the group of sources of one magnitude and one parallax, which is called as "Lutz-Kelker Bias". To calculate the Lutz-Kelker Bias quantatively, we calculate the conditional probability $P_{\varpi_{\rm obs},m}\ (\varpi)$ that the source with the observed parallax $\varpi_{\rm obs}$ and the apparent magnitude m has true parallax of ϖ, based on three assumption as following;
(1) we assumed that the uncertainty of the observed parallax is a gaussian with the full width half maximum, σ_ϖ. That is, when the observed parallax is $\varpi_{\rm obs}$, the true parallax is $\varpi_{\rm obs}$ and the apparent magnitude is m, the conditional probability $P_{\varpi,m}\ (\varpi_{\rm obs})$ is expressed as

$$P_{\varpi,m}(\varpi_{\rm obs}) = \frac{1}{\sqrt{2\pi\sigma_\varpi}} \exp\Big\{\frac{-(\varpi_{\rm obs}-\varpi)^2}{2\sigma_\varpi^2}\Big\}. \tag{A.2}$$

(2) the luminosity function of the focused group of sources is $\Phi(M) \propto 10^{\beta M}$, where M is absolute magnitude, and the relation is held regardless of the source position.
(3) the spatial density distribution is uniform and the number density from D to $D + dD$ is $\nu\ (D)$.

The conditional probability under the condition that the observed parallax is $\varpi_{\rm obs}$, the true parallax is ϖ and apparent magnitude is m is

$$\begin{aligned} P_m(\varpi_{\rm obs} \cap \varpi) &= P_m(\varpi_{\rm obs}) P_{\varpi_{\rm obs},m}(\varpi) = P_m(\varpi) P_{\varpi,m}(\varpi_{\rm obs}) \\ P_{\varpi_{\rm obs},m}(\varpi) &= \frac{P_m(\varpi) P_{\varpi,m}(\varpi_{\rm obs})}{P_m(\varpi_{\rm obs})}. \end{aligned} \tag{A.3}$$

We calculate $P_m(\varpi)$ since we assumed the $P_{\varpi,m}(\varpi_{\rm obs})$. The relation between D and m is similarly

$$P_m(D) = \frac{P(D) P_D(m)}{P(m)}. \tag{A.4}$$

Since the luminosity function is defined as $\mathrm{dN} = \Phi(\mathrm{M})\nu(\mathrm{D})\mathrm{dM} \cdot 4\pi \mathrm{D}^2 \mathrm{dD}$,

$$P_s(M) \propto \Phi(M) P(s) = \nu(D) D^2 \tag{A.5}$$

Since $P_m(\varpi)\,\mathrm{d}\varpi = P_m(D)\,\mathrm{d}D$, we use equation A.4 and equation A.5

$$P_m(D) =\propto \frac{\Phi(M)\nu(D)}{P(m)}\frac{1}{\varpi^4}. \tag{A.6}$$

When we assign the $P_m(D)$ for equation A.3 and use equation A.2,

$$P_{\varpi_{\rm obs},m}(\varpi) \propto \frac{1}{P_m(\varpi_{\rm obs})P(m)}\frac{\Phi(M)}{\varpi^4}\exp\Big\{\frac{-(\varpi_{\rm obs}-\varpi)^2}{2\sigma_\varpi^2}\Big\}. \tag{A.7}$$

The luminosity function is

$$\Phi(M) \propto 10^{\beta M} = \varpi^{5\beta}10^{\beta m} \tag{A.8}$$

From the equation A.7 and A.8,

$$P_{\varpi_{\rm obs},m}(\varpi) \propto \frac{10^{\beta m}}{P_m(\varpi_{\rm obs})P(m)}\varpi^{5\beta-4}\exp\Big\{\frac{-(\varpi_{\rm obs}-\varpi)^2}{2\sigma_\varpi^2}\Big\} \tag{A.9}$$

In the left term, when we regard $10^{\beta m}$, $P_m(\varpi_{\rm obs})$ and P_m as constant,

$$P_{\varpi_{\rm obs},m}(\varpi) \propto \varpi^{5\beta-4}\exp\Big\{\frac{-(\varpi_{\rm obs}-\varpi)^2}{2\sigma_\varpi^2}\Big\}. \tag{A.10}$$

It must be $\frac{\varpi_{\rm obs}}{\sigma_\varpi} \gtrsim 4$ to be possible that the equation approaches to zero when $\varpi \sim 0$. This indicate that we measure the parallax with the error of 17.5 %. And, to lessen the asymmetry property and to be easy to use statistically, it must be $\frac{\varpi_{\rm obs}}{\sigma_\varpi} \gtrsim 10$, which correponding to the error of parallax of 10 %. Therefore, the 10% is used as a guide to be acheived when we measure the parallax.

Acknowledgements

My thesis must never finish if I have no help from the all my instructors, collaborators, supervisors, senior students and junior students. I cannot be too thankful for all of them. I am very glad to meet and to study astronomy, especially astrometry. First, I aspired for Kagoshima University to study astronomy, and fortunately, I could have worked on them for nine years. I was invited to join the laboratory I belong to now by assistant professor Akiharu Nakagawa seven years ago. This invitation was the opportunity to open the door to study astrometry with VERA. Many VERA members gave me many knowledges and wonderful time. From the time to Now, I studied many things from the astronomy and astrometry to the human relationships in many interesting and difficult experiences. All these are my treasure to live and I must live to apply many experiences.

I cannot be too thankful for my supervisor Toshihiro Handa. He gave me the chance to continue to study astronomy and many advices and knowledges, about not only astronomy but also the others. I would like to be thankful for Akiharu Nakagawa. He taught me how to use AIPS for reducing VERA data, the principle of the interferometer, especially VLBI, and what's more, invited me to the astronomy. I would like to acknowledge the supports and encouragement my advisors in Kagoshima university, Toshihiro Omodaka, Hirohi Imai and Hiroyuki Nakanishi. I am also grateful to all VERA members, especially Tomoharu Kurayama, Takumi Nagayama, Mareki Honma, Tomoya Hirota and Nobuyuki Sakai. And I am grateful to all of the already graduated senior students and junior students sharing same time with me.